Understanding the Impact of a Serrated Trailing Edge on the Unsteady Hydrodynamic Field

Stefan Josip Letica

Thesis submitted to the faculty of the Virginia Polytechnic Institute and State University in partial fulfillment of the requirements for the degree of

Master of Science

In

Aerospace Engineering

William N. Alexander, Committee Chair

William J. Devenport

Kevin T. Lowe

September 4, 2020

Blacksburg, VA

Keywords: trailing edge noise, aeroacoustics, serrations, turbulent boundary layers, wall jet

Understanding the Impact of a Serrated Trailing Edge on the Unsteady Hydrodynamic Field

Stefan Josip Letica

ABSTRACT

Trailing edge noise is a common noise source in aerodynamic applications, such as wind turbines, duct fan blades, and propellers. As sound is a nuisance for people near this machinery, methods of reducing trailing edge noise are being investigated. A proven method of trailing edge noise reduction is using a serrated trailing edge. Many prior experiments have shown that a trailing edge with sawtooth serrations can reduce trailing edge noise compared to a straight trailing edge, but the mechanism by which sawtooth serrations reduce noise is not fully understood. Previous theoretical models have assumed that the turbulence field convecting past a serrated trailing edge is unchanged by the presence of the serrations, but experiments have shown that this is not the case in reality. This work attempts to further explore the mechanisms behind why trailing edge serrations reduce trailing edge noise. Additionally, it evaluates the usefulness of a wall jet wind tunnel for use in the study of serrated trailing edges. Experiments were conducted in an anechoic wall jet wind tunnel using a straight trailing edge configuration and a serrated trailing edge configuration. It was found that there may be differences in the unsteady surface pressure over serrated edges in one-sided flows as compared to two-sided flows, like on that of an airfoil, most notably in relation to the magnitude of the unsteady pressure on the serrations. In the wall jet and in agreement with other studies, it was found that the unsteady pressure fluctuations increase towards the tip of the serration in one-sided flows. This is counter to what is found in some studies of two-sided flows. Good agreement was found between some models of the wavenumber-frequency wall pressure spectrum of a turbulent boundary layer and the measured wall pressure spectrum on the straight trailing edge, and these models also produced good predictions of the noise produced by this trailing edge using Amiet's equation. A surface pressure microphone array was used to estimate the zero spanwise wavenumber surface pressure spectrum. This spectrum was used in Amiet's method to predict the measured trailing edge noise. Predictions using the wavenumber-filtered measurement tended to overpredict the measured far field noise most likely due to the inclusion of broader wavenumber content through the array's side lobe response and the breadth of the main lobe. The serrated trailing edge was found to increase coherence between two points on the same serration while reducing coherence between two points on different serrations. It was concluded that the presence of the serrations decorrelates small-scale turbulent eddies. Additionally, it was found that while the serrated trailing edge did reduce the noise produced, its destructive effect on the geometry-based resonance of the straight trailing edge configuration may have amplified the magnitude of the reduction. Finally, it was concluded that the serrations do indeed affect the hydrodynamic field near the trailing edge, and the theoretical models which make the assumption otherwise must be refined.

Understanding the Impact of a Serrated Trailing Edge on the Unsteady Hydrodynamic Field

Stefan Josip Letica

GENERAL AUDIENCE ABSTRACT

Trailing edge noise is a common noise source in aerodynamic applications, such as wind turbines, duct fan blades, and propellers. As sound is a nuisance for people near this machinery, methods of reducing trailing edge noise are being investigated. A proven method of trailing edge noise reduction is using a serrated trailing edge. Many prior experiments have shown that a trailing edge with sawtooth serrations can reduce trailing edge noise compared to a straight trailing edge, but the mechanism by which sawtooth serrations reduce noise is not fully understood. This work attempts to further explore the mechanisms behind why trailing edge serrations reduce noise. Experiments were conducted in an anechoic wind tunnel facility. It was found that a one-sided flow over a serrated trailing edge may be significantly different from that over a two-sided flow. Good agreement was found between prediction models and measurements of trailing edge noise. The serrated trailing edge was effective at reducing the coherence of turbulent eddies across the roots of the sawtooth serrations. It was concluded that the serrated trailing edge is effective at reducing noise, and that one means of doing so is decreasing the correlation of small-scale turbulent eddies, and that current models of the flow over serrations may need to be refined.

Table of Contents

Chapter 1. Introduction 1
1.1 Aeroacoustics 2
1.2 Amiet's Trailing Edge Noise Prediction Theory 6
1.3 The Empirical Prediction Method of Brooks, Pope, and Marcolini 11
1.4 Experimental Validation of Trailing Edge Noise Prediction Theory 13
1.5 Models of Surface Pressure Wavenumber-Frequency Spectra 15
1.6 Methods of Trailing Edge Noise Reduction 20
1.6.1 Porous Airfoils 20
1.6.2 Finlets 22
1.6.3 Serrations 24
1.6.4 Summary of Trailing Edge Noise Reduction Methods 31
1.7 Objective 32
Chapter 2. Apparatus and Instrumentation 33
2.1 Wall Jet Tunnel 33
2.1.1 Wall Jet Tunnel Geometry 33
2.1.2 Characteristics of Wall Jet Flow 35
2.1.3 Experimental Conditions 37
2.2 Microphones and Data Acquisition 37
2.2.1 Far Field – B&K 1/2" Microphones 38
2.2.2 Surface Pressure – Knowles FG-23329-P07 Microphones 39
2.2.3 Surface Pressure – B&K 1/8" Microphones 40
2.2.4 Data Acquisition System and Processing 41
2.3 Microphone Calibration 42
2.3.1 Microphone Spatial Averaging 42
2.3.2 Frequency Response Calibration 48
2.3.3 Microphone Dynamic Range 55

2.4 Straight Trailing Edge 63
2.5 Serrated Trailing Edge 69
2.6 Beamforming Array 75
2.6.1 Array Design 75
2.6.2 Delay and Sum Beamforming 76
2.6.3 Beamforming Performance of the Linear Array 80
2.7 Wavenumber Filtering 81
2.8 Measurement Uncertainty 86
Chapter 3. Results and Discussion 90
3.1 Characterization of Wall Jet Turbulent Boundary Layer 90
3.1.1 Evaluating the statistically frozen flow hypothesis 90
3.1.2 Streamwise coherence length scale 93
3.1.3 Convection velocity 95
3.2 Trailing Edge Noise from Straight Trailing Edge 99
3.2.1 Beamforming to Identify Noise Sources 103
3.2.2 Cavity Resonance 106
3.2.3 The Image in the Wall 107
3.3 Surface Pressure and Predictions of Trailing Edge Noise for Straight Trailing Edge 110
3.3.1 Wavenumber Filtered Spectrum 110
3.3.2 Potential Unsteady Loading 112
3.3.3 Single-Point Models of Surface Pressure Spectra 114
3.3.4 Predictions of Trailing Edge Noise Using Amiet's Method 116
3.3.5 Brooks-Pope-Marcolini Predictions 121
3.4 Straight Trailing Edge Spanwise Coherence 125
3.5 Far Field Noise from Serrated Trailing Edge 127
3.6 Measurements of Surface Pressure Autospectra on Serrations 129
3.6.1 Positional Comparisons 130

3.6.2 Contour Plots of Surface Pressure on Serrations 133
3.7 Measurements of Coherence on Serrations 136
3.7.1 Coherence Between Center and Side of Serration 136
3.7.2 Coherence Across Serration Centerline 138
3.7.3 Coherence Across the Root 139
3.7.4 Streamwise Coherence Along Serration 141
3.7.5 Coherence Along the Serration Edge 143
Chapter 4. Conclusions 147
References 149

List of Tables

Table 2.1, Self-similarity coefficients for Virginia Tech wall jet tunnel 36
Table 2.2, Estimated boundary layer parameters for wall jet flow in experimental conditions, straight trailing edge conditions 37
Table 2.3, Convection velocity measured using two-point correlation data..... 46
Table 2.4, Valid frequency range for surface pressure microphone autospectra and spanwise coherence measurements 62
Table 2.5, Far field microphone positions for straight trailing edge experiments 65
Table 2.6, Surface pressure microphone spanwise distribution for straight trailing edge 67
Table 2.7, Actual surface pressure microphone positions for serrated trailing edge 72
Table 2.8, Prescribed surface pressure microphone positions and placement error 73
Table 2.9, Far field microphone positions for serrated trailing edge experiments 75
Table 3.1, Far field microphone positions for serrated trailing edge experiments 98
Table 3.2, Frequency bins corresponding to contour plot length scales 134

List of Figures

Figure 1.1, Coordinate system 1
Figure 1.2, Semi-infinite half-plane used in Ffowcs Williams *et al.* and Amiet prediction theories and trailing edge noise directivity diagram 7
Figure 1.3, Form of wavenumber-frequency wall pressure spectrum at constant frequency 16
Figure 2.1, Wall jet settling chamber internal structures, top-down view 33
Figure 2.2, Wall jet anechoic chamber 34
Figure 2.3, B&K Type 4190 1/2" microphone-preamplifier unit 38
Figure 2.4, B&K Type 4190 microphones mounted on gantry 39
Figure 2.5, Knowles microphone box 40
Figure 2.6, B&K Type 4138 microphone-preamplifier unit with pinhole cap 41
Figure 2.7, Example of flush-mounted microphone spatial alignment 43
Figure 2.8, Sine wave pressure signal spatial averaging 44
Figure 2.9, Microphone spatial response function $|H(kR)|^2$ 47
Figure 2.10, Microphone spatial response function $|\mathrm{H(kR)}|^2$ as a function of frequency (dashed – B&K response, solid – Knowles response) 48
Figure 2.11, Frequency response calibration setups 50
Figure 2.12, Amplitude calibration of B&K Type 4138 microphones 51
Figure 2.13, Phase response calibration of B&K Type 4138 microphones 52
Figure 2.14, Frequency and phase response calibration curves for Knowles box 1 microphone 1 53
Figure 2.15, Sensitivity range of Knowles microphone frequency response 54
Figure 2.16, Layout of Knowles performance validation experiment 56
Figure 2.17, Comparison of flat-plate Knowles and B&K Type 4138 autospectra (left) and spanwise coherence between equally-spaced pairs of microphones (right) 59
Figure 2.18, Comparison of B&K pinhole response and flat response at low speed. U_j = 15 m/s 60
Figure 2.19, OASPL of Knowles microphone spectrum vs. nozzle velocity 61
Figure 2.20, Straight trailing edge setup in wall jet tunnel 64

Figure 2.21, Geometry of "mock" trailing edge (dimensions in mm) 64
Figure 2.22, Far field microphone arc in straight trailing edge configuration 66
Figure 2.23, Knowles microphones mounted flush with mock trailing edge surface 66
Figure 2.24, Surface pressure microphone spanwise distribution for straight trailing edge 67
Figure 2.25, Comparison between flat plate surface pressure and trailing edge surface pressure autospectra 69
Figure 2.26, Side view of serrated trailing edge (dimensions in mm) 70
Figure 2.27, Top view of serrated trailing edge. $\lambda = 1.5$ cm, $2h = 1.5$ cm 70
Figure 2.28, Close up view of microphone locations on serrated trailing edge (dimensions in mm) 71
Figure 2.29, Serrated trailing edge and far field microphones in wall jet 74
Figure 2.30, Microphones mounted in serrated trailing edge 74
Figure 2.31, Linear microphone array for beamforming experiment 76
Figure 2.32, Acoustic monopole in free space with linear array of microphones 77
Figure 2.33, Two acoustic monopoles in free space with linear array of microphones ... 78
Figure 2.34, Point spread function and beamwidth for $f = 2000$ Hz monopole at origin, normalized on peak value. 80
Figure 2.35, Wavenumber response function $|A(k_3)|^2$ for different microphone spacings 85
Figure 2.36, Full array response $|W(k_3)|^2$ of wavenumber filter array 86
Figure 2.37, Repeatability comparison for three runs of data measured by microphone 13 on the straight trailing edge at U_j = 0 m/s. 87
Figure 2.38, Repeatability comparison for three runs of data measured by microphone 1 in the far field of the straight trailing edge at U_j = 70 m/s. 88
Figure 2.39, Surface pressure spectrum uniformity measured at U_j = 50 m/s 89
Figure 3.1, Autospectra of surface pressure microphones $\phi_{pp}(f)$ in streamwise orientation in wall jet flat plate 91
Figure 3.2, Experimental and predicted streamwise coherence curves for wall jet flat plate 92
Figure 3.3, Streamwise coherence decay length 94

Figure 3.4, Phase angle of cross spectrum between B&K 1/8" microphones mounted in flat plate. 96
Figure 3.5, Ratio of convection velocity to maximum velocity as a function of frequency. 97
Figure 3.6, Straight trailing edge signal-to-noise, distance-corrected. Dotted lines are background measurements, solid lines are with trailing edge installed. 100
Figure 3.7, Background-subtracted trailing edge noise from straight trailing edge 101
Figure 3.8, U_m^5 curve fit to integrated background-subtracted spectra 102
Figure 3.9, Beamforming experiment results, streamwise array (left side) and spanwise array (right side) at U_j = 70 m/s. The black dashed line represents the location of the trailing edge. 105
Figure 3.10, Background-subtracted trailing edge noise with predicted resonant frequencies overlaid. Blue dashes are frequencies with correction of $0.3d$ and red dashes are frequencies with correction of $0.6d$. 107
Figure 3.11, Image of the undercut trailing edge in the wall as seen by Microphone 1. 108
Figure 3.12, Change in far field sound pressure level due to image in wall effects. 109
Figure 3.13, Filtered surface pressure spectrum compared to single-point spectra of microphones. 112
Figure 3.14, Undercut microphone mounted in wall jet 113
Figure 3.15, Pressure spectrum beneath trailing edge as measured by microphone embedded underneath. Dashed lines are surface pressure data from Mic 8 on the top side (flow side) of the trailing edge. 113
Figure 3.16, Single-sided surface pressure frequency spectra model comparison. The full Chase wavenumber-frequency wall pressure spectrum model is numerically integrated in k_1 and k_3, and Real is the averaged measured surface pressure spectrum. 114
Figure 3.17, Comparison of $\phi_m(\omega)$ implied by Goody and Chase models and real signal with wavenumber filter applied. $\phi_m(\omega)$ is double-sided in this figure. 117
Figure 3.18, Amiet's method predictions of trailing edge noise at Mic 1, U_j = 60 m/s. 119
Figure 3.19, Amiet predictions of trailing edge noise at Mic 1 for U_j = 60 m/s including image in wall effects 121

Figure 3.20, 1/3 octave band predicted and measured trailing edge noise at Mic 1, U_j = 60 m/s 124
Figure 3.21, Spanwise coherence between surface pressure microphones on straight trailing edge. Dashed lines are data from flat plate measurements, with black representing the B&K-B&K pair and magenta representing the B&K-Knowles pair 126
Figure 3.22, Spanwise coherence decay length 127
Figure 3.23, Background-subtracted trailing edge noise from serrated trailing edge..... 128
Figure 3.24, Comparison between distance-corrected background-subtracted trailing edge noise from serrated trailing edge and straight trailing edge. Solid lines are serrated edge, dotted lines are straight edge..... 129
Figure 3.25, Local positions of surface pressure microphones visualized on a single serration (not to scale)..... 130
Figure 3.26, Streamwise microphone similarity comparisons with averaged straight trailing edge autospectrum. Left column is measurements with $U_j = 20$ m/s, right column is U_j = 60 m/s..... 132
Figure 3.27, Contour plots of surface pressure autospectra on serrations. Black triangle denotes the full serration size, green triangle denotes the interpolated region, and blue markers denote microphone locations. 135
Figure 3.28, Coherence between center and side of serrations..... 137
Figure 3.29, Coherence across centerline of serrations 138
Figure 3.30, Coherence across roots of serrated edge 140
Figure 3.31, Streamwise coherence along centerline of serration. Blue line represents coherence between two B&K microphones, green line represents coherence between B&K and Knowles microphones. 142
Figure 3.32, Coherence along the serrated edge compared to coherence along the straight trailing edge 144
Figure 3.33, Coherence along the serrated edge compared to streamwise coherence on the flat plate 146

Chapter 1. Introduction

Trailing edge noise is produced when acoustic sources in a turbulent boundary layer are convected past a sharp trailing edge. The sharp trailing edge radiates the sound to the far field much more efficiently than it would be radiated without the trailing edge's presence. As will be explored later, this trailing edge noise is a significant contributor of noise in many practical applications.

In the following sections, repeated indices *i, j* imply a summation over that index. Unless otherwise stated, *i* and *j* are 1, 2, 3. In terms of the geometry of a trailing edge in a 1D upper surface turbulent boundary layer flow, the 1-direction is streamwise, the 3-direction is spanwise, and the 2-direction is the vertical distance from the trailing edge, with positive directions indicated below and the origin at the mid-span of the trailing edge. This coordinate system is illustrated in Figure 1.1.

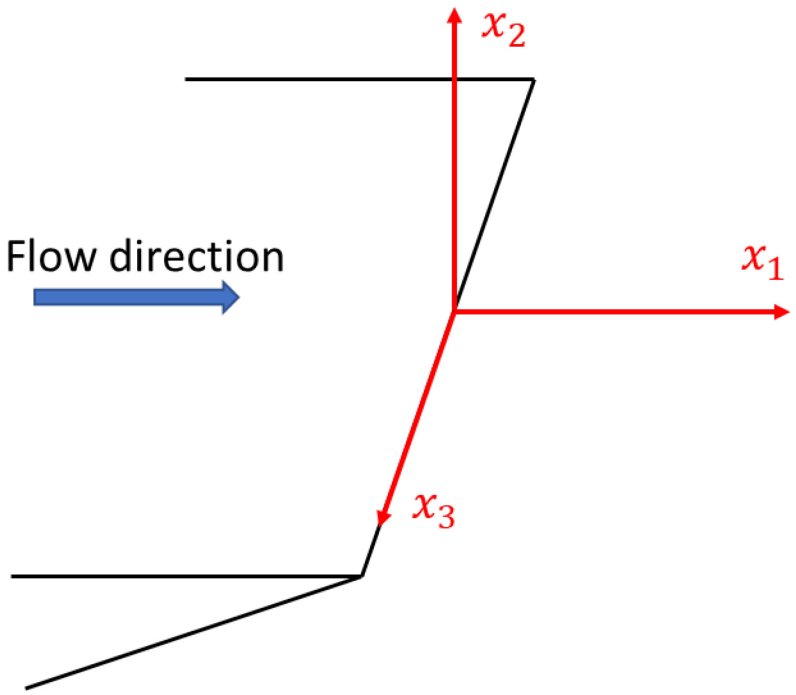

Figure 1.1, Coordinate system.

The human ear is capable of hearing sounds within a range of 20 – 20,000 Hz. Pressure waves vibrate the eardrum, which sends a signal to the brain that we perceive as sound. The sensitivity of the eardrum is logarithmic, and thus it is useful to use a logarithmic unit to describe sound pressure levels. Typically, in air acoustics calculations, the units of sound pressure are expressed as the root mean square of the pressure fluctuation amplitude in decibels referenced to 20 μPa [1]. In the following sections, all reported dB values are referenced to 20 μPa unless otherwise noted.

1.1 Aeroacoustics

The study of aeroacoustics in its present form began with Sir James Lighthill's 1952 publication [2]. Lighthill's paper is concerned with the radiation of the energy of sound by turbulent flow. He considers a fluctuating flow within a small part of a large control volume, the remainder of which is at rest, and can be considered a uniform acoustic medium at rest, with pressure p_∞ and density ρ_∞. The back-reaction of the sound on the fluctuating flow field is significantly less than the fluctuations themselves; thus, the flow in the fluctuating region can be thought of as a forcing function for the production of sound.

Starting with the tensor form of the continuity equation:

$$\frac{\partial \rho}{\partial t} + \frac{\partial (\rho v_i)}{\partial x_i} = 0 \tag{1.1}$$

and the momentum equation:

$$\frac{\partial (\rho v_i)}{\partial t} + \frac{\partial \left(\rho v_i v_j + p_{ij}\right)}{\partial x_j} = 0 \tag{1.2}$$

Lighthill differentiated the continuity equation with respect to time and took the divergence of the momentum equation with respect to x_i. Then, he subtracted them, giving:

$$\frac{\partial^2 \rho}{\partial t^2} - \frac{\partial^2 \left(\rho v_i v_j + p_{ij}\right)}{\partial x_i \partial x_j} = 0 \tag{1.3}$$

Now consider the flow region. Lighthill sought to construct an equation that resembled the acoustic wave equation in the ambient,

$$\frac{\partial^2 \rho}{\partial t^2} - c_\infty^2 \frac{\partial^2 \rho}{\partial x_i^2} = 0 \tag{1.4}$$

To do this, he simply subtracted the Laplacian term $\partial^2(\rho' c_0^2)/\partial x_i^2$ from both sides of equation (1.3), and isolated the wave equation "form" on the left-hand side. Then, he combined the terms on the right-hand side into one tensor. In this case, the fluctuating density $\rho' = \rho - \rho_\infty$ is taken to be the difference of the fluctuating density and the ambient density, rather than the mean density in the flow. This is because the observer is never within the source region, and therefore all sound observed will be in the region where the density fluctuations are relative to the ambient. Thus, the time derivative of the density is equivalent to the time derivative of the fluctuating density, and they can be used interchangeably. It should also be noted that the compressive stress tensor $p_{ij} = p\delta_{ij} - \sigma_{ij}$ and that the speed of sound in the ambient $c_\infty^2 = p'/\rho'$. δ_{ij} is the Kronecker delta, equal to 1 when $i = j$ and 0 otherwise. Using these relations,

$$\begin{aligned} \frac{\partial^2 \rho'}{\partial t^2} - c_\infty^2 \frac{\partial^2 \rho'}{\partial x_i^2} &= -c_\infty^2 \frac{\partial^2 \rho'}{\partial x_i^2} + \frac{\partial^2 \left(\rho v_i v_j + p_{ij}\right)}{\partial x_i \partial x_j} \\ &= -c_\infty^2 \frac{\partial^2 \rho'}{\partial x_i^2} + \frac{\partial^2 \left(\rho v_i v_j + p\delta_{ij} - \sigma_{ij}\right)}{\partial x_i \partial x_j} \end{aligned} \tag{1.5}$$

The right-hand side can be further simplified by realizing that the Laplacian operator on the scalar ρ' yields a scalar, and the same result can be achieved by:

$$\frac{\partial^2 c_\infty^2 \rho'}{\partial x_i^2} = \frac{\partial^2 c_\infty^2 \rho' \delta_{ij}}{\partial x_i \partial x_j} \tag{1.6}$$

Combining the terms on the right-hand side yields:

$$\frac{\partial^2 \rho'}{\partial t^2} - c_\infty^2 \frac{\partial^2 \rho'}{\partial x_i^2} = \frac{\partial^2 T_{ij}}{\partial x_i \partial x_j} \tag{1.7}$$

where T_{ij}, known as the Lighthill stress tensor, is defined by:

$$T_{ij} = \rho v_i v_j + (p' - \rho' c_\infty^2)\delta_{ij} - \sigma_{ij} \tag{1.8}$$

This stress tensor represents all the possible ways a turbulent flow can generate noise. The first term is the fluctuating Reynolds stress, which is the contribution of velocity fluctuations to the mean flow, the second term is stresses caused by non-isentropic pressure and density fluctuations, and third term is the viscous stresses. Outside of the flow, $T_{ij} = 0$; this is evident because there are no velocity fluctuations, the viscous effects can be ignored, and the pressure fluctuation p' is equivalent to the density fluctuation times the scaling factor $\rho' c_\infty^2$. This means that any fluctuations in density are propagated acoustically, and thus the left-hand side represents sound.

The result of Lighthill is rather simple, but determination of T_{ij} is not simple. Choosing an improper source region can lead to a situation where the rounding errors from the integration outweigh the contributions from the source terms within the volume integral [1]. Lighthill proposed fixing this issue by expanding the volume integral term and identifying the leading order source terms; Curle (1955) finished this work [3], and gave the following result:

$$\begin{aligned} p'(x,t) = &\int_{-T}^{T} \int_S \left((p_{ij} + \rho v_i v_j) \frac{\partial G}{\partial y_i} + G \frac{\partial (\rho v_j)}{\partial \tau} \right) n_j dS(y) d\tau \\ &+ \int_{-T}^{T} \int_V \left(\frac{\partial^2 G}{\partial y_i \partial y_j} \right) T_{ij}(y,\tau) dV(y) d\tau \end{aligned} \tag{1.9}$$

In this equation, the source terms are dependent on the rate of change of mass flux on the surface $\left(n_j \partial(\rho v_j)/\partial \tau\right)$, the force per unit area on the fluid by the surface term $\left(p_{ij} n_j\right)$, the

momentum flux across the surface $(\rho v_i v_j)$, and the contribution from Lighthill's stress tensor ($T_{ij}(y,\tau)$). One needs to find a Green's function G to satisfy the boundary condition.

The most important result to take away from Lighthill and Curle's formulations for this thesis is that the sources producing sound from a turbulent flow can be described as a set of quadrupoles (in the volume integral) and dipoles (in the surface integral). All of the sound from a turbulent flow is produced entirely within the flow and radiates to the far field through an acoustic medium; the quadrupole terms scale on the order of M^5U^3, while the dipole terms scale on the order of M^3U^3 [1]. This shows that quadrupole sources are much more sensitive to flow speed, and in the regime of low Mach number flow, are much quieter than dipoles.

Since the derivation of Lighthill's acoustic analogy and Curle's equation, the field of aeroacoustics has expanded drastically. Aerodynamic noise is produced in many applications, and understanding its nature is key to predicting the noise that will be produced by an aerodynamic system, whether it be an airfoil, turbomachinery, etc. The original theory of Lighthill and Curle can help us understand these sources.

Many aerodynamic sources have been observed from airfoils. Brooks, Pope, and Marcolini (1989) [4] summarized five primary sources of self-noise that resulted from the interaction between an airfoil and its own boundary layer or wake:

- Turbulent boundary layer trailing edge noise
- Laminar boundary layer vortex shedding noise
- Separation-stall noise
- Trailing edge bluntness vortex shedding noise
- Tip vortex formation noise

Self-noise is noise produced by the unsteady interaction between an airfoil and its boundary layer. This thesis is focused on the study of turbulent boundary layer trailing edge noise, as described in the beginning of the section. Turbulent boundary layer trailing edge (TBL-TE) noise is produced when a turbulent boundary layer flows over a sharp trailing edge. The

discontinuity in the flow efficiently scatters noise from the turbulence in the boundary layer to the far field. This takes the form of a broadband noise source, as the edge interacts efficiently with a wide range of eddy sizes. In a mathematical sense, trailing edge noise is a result of equalizing the unsteady pressure of the boundary layers due to the sudden removal of the upstream non-penetration condition through the airfoil; the radiated noise is then a function of the magnitude of the pressure jump.

Trailing edge noise is a major noise source in a variety of aerodynamic applications. Wind turbines, duct fan blades, and propeller noise are some of the most important fields of application for trailing edge noise [5–7]. In the case of wind turbines and duct fan blades, trailing edge noise has been identified as a major contributor to the noise they produce; while trailing edge noise can be lost in other noise sources that are produced in rotor and propeller blades, such as tip vortex noise and leading edge noise [7], it is nonetheless still a component of the noise produced. Sound is a nuisance for both civilians and operators of these equipment; being able to predict this sound is an important part of the design process to ensure that the device being installed will not be overly disruptive. Predicting trailing edge noise is typically done with either theoretical formulations or semi-empirical methods, and both will be explored in this work.

1.2 Amiet's Trailing Edge Noise Prediction Theory

A useful prediction method for trailing edge noise is that of Amiet (1976) [8], who devised a method of calculating the trailing edge noise using the input of the surface pressure spectrum upstream of the trailing edge.

A previous method to predict trailing edge noise was devised by Ffowcs Williams and Hall (1970) [9], who found the trailing edge noise in terms of the volume integral from Curle's equation (1.9). This approach utilizes a volume integral that encloses a semi-infinite flat plate defined by $x_2 = 0$ for $x_1 \leq 0$ but does not include it, using a tailored Green's function to describe such a volume, eliminating the surface integral from Curle's equation. The assumption of a semi-infinite flat plate is generally a good one for acoustic wavelengths

smaller than the chord of the airfoil. Performing the integration gives two important results: that the directivity of trailing edge noise is a cardioid based on $\sin^2(\theta/2)$, and that the far field noise scales as U^5.

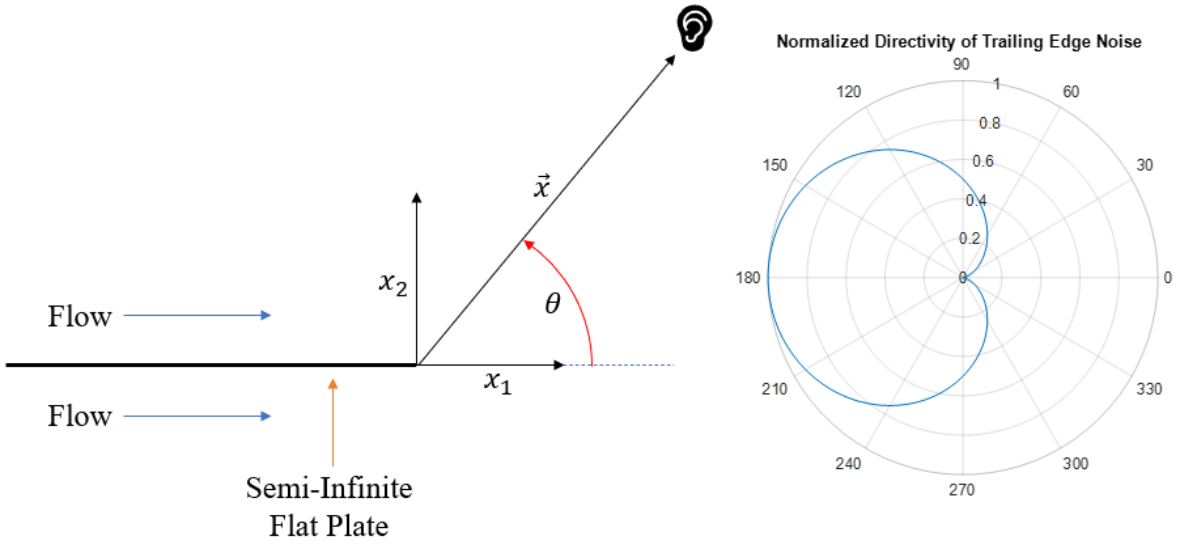

Figure 1.2, Semi-infinite half-plane used in Ffowcs Williams *et al.* and Amiet prediction theories and trailing edge noise directivity diagram.

In practice, however, it is difficult to measure the content of the volume integral when trying to apply Ffowcs Williams and Hall's method to a real flow. Amiet's approach considers the force of the surface of the wall on the fluid as the noise source as the manifestation of the turbulence in the boundary layer. Thus, there are two strategies for predicting trailing edge noise. The turbulent quadrupole sources can be considered directly or the surface dipole response can be considered independently. Amiet solves for the trailing edge noise using the unsteady pressure loading on the surface. It is important to note that in both cases the original source of the noise is the turbulence in the boundary layer; while Ffowcs-Williams and Hall consider the turbulence itself, solving a pure volume integral problem, Amiet's approach considers the turbulence as it manifests itself as pressure fluctuations on the surface, solving an unsteady loading dipole radiation problem.

Amiet assumed that the turbulent velocity field is unaffected by the presence of the trailing edge, or that the turbulence is statistically stationary as it moves past the trailing edge. This compares with Taylor's "frozen field" hypothesis, which states that eddies do not evolve as they convect. Amiet allows for eddy evolution, but the statistical properties of the surface pressure field remain the same. This assumption allows the calculation of the trailing edge noise from the upstream wall pressure spectrum, which is fairly trivial to measure.

Another assumption made to simplify the surface pressure field is that for each streamwise convective wavenumber component $K_1 = \omega/U_c$, there is a single associated convection velocity U_c. In reality, this is not the case; the pressure at a measured frequency is a combination of many $K_1 - U_c$ pairs, which have a constant product ω, the frequency. This manifests itself as the "convective ridge" [10] in the wavenumber frequency wall pressure spectrum, which shows that the dominant components of surface pressure fluctuations at a particular frequency are concentrated around a convective wavenumber K_1 as measured relative to U_c. This region of the surface pressure spectrum dominates the overall range of wavenumbers found at a given frequency and is thus the largest contributor to trailing edge noise. More description of the convective ridge can be found in Section 1.5.

Amiet's analysis uses the Schwarzschild solution procedure [11] to solve the flat-plate pressure equalization problem described in Figure 1.2. The Schwarzschild solution models the trailing edge noise as a result of the pressure difference across the plate equalizing suddenly at the trailing edge as the two boundary layers meet again. The additional pressure field necessary to equalize this pressure beyond $x_1 > 0$ manifests as an acoustic field that satisfies the non-penetration condition through the plate and cancels the pressure jump for the boundary layers downstream of the plate.

Following Amiet's derivation, which used the Schwarzschild solution for a single boundary layer, the following equation for trailing edge noise as observed in the $x_3 = 0$ plane is obtained (as written by Glegg and Devenport [1], which is twice the result that Amiet

produced due to their introduction of a second boundary layer on the opposite side of the plate):

$$S_{pp}(x_1, x_2, x_3 = 0, \omega) = \pi b \left(\frac{\omega c x_2}{\pi 4 c_\infty r_e^2}\right)^2 |\mathcal{L}|^2 \phi_{pp}(0, \omega) \tag{1.10}$$

In this equation, $r_e^2 = x_1^2 + \beta^2(x_2^2 + x_3^2)$ is the distance from the source to the observer, corrected for the flow speed using the Prandtl-Glauert transformation, c is the chord of the airfoil, b is the span of the airfoil, $\mathcal{L}$ is the "generalized lift function" [12], which describes how the pressure field equalizes at the trailing edge, and $\phi_{pp}(k_3, \omega)$ is the spanwise wavenumber frequency spectrum of the wall pressure fluctuations.

There are several important relations to note here. The first is the assumption that the leading-edge response and trailing edge response do not affect each other; in practical applications this is not true, but it is a decent approximation for the purposes of the calculation. Amiet later released an addendum to his paper, which clarified that the $\mathcal{L}$ term should be modified to decay to 0 at the leading edge, since otherwise there would be a leading-edge contribution due to the sudden appearance of a pressure field [12]. This assumption of a semi-infinite plate is important because it is impossible to resolve a system that contains both a leading edge and a trailing edge, and it is a good approximation for airfoils with a chord that is large relative to the acoustic wavelength.

The generalized lift function is essentially an integral of the airfoil response function g, which is the loading response of the surface due to the turbulence passing the trailing edge. The approximation given by Amiet of this integral shows $\mathcal{L}$ to be dependent on K_1, c, U_c, M, r_e and x_1.

The result of zero spanwise wavenumber is tied to the observer being in the $x_3 = 0$ plane. As the intersection point of a particular gust moves down the straight trailing edge, the radiation efficiency becomes stronger and stronger [1]; for a perfectly normal plane wave ($k_3 = 0$), this trace speed is effectively infinite, thus making it the dominant noise source.

This dominant noise source only couples with observers in the $x_3 = 0$ plane; nonzero spanwise wavenumbers will not couple with the observer in the $x_3 = 0$ plane, as they will radiate with an $x_3 \neq 0$ component. For the purposes of using this formula, then, the zero-spanwise-wavenumber frequency wall pressure spectrum must be an input.

Assuming that the turbulent eddies are small relative to the chord ($kc \ll 1$), Glegg and Devenport [1] show that the $|\mathcal{L}|^2$ term can be approximated as:

$$|\mathcal{L}|^2 \sim \frac{4L^2}{c^2}\frac{1}{M}\frac{1}{(1 + x_1/r_e)} \tag{1.11}$$

where L is the length scale of the turbulence at the given frequency ($\omega \sim U/L$). Noting that the x_i/r_e terms are nothing more than direction cosines, they arrive at the following expression for the scaling and directivity of the trailing edge noise:

$$S_{pp}(x_1, x_2, x_3 = 0, \omega) \sim \frac{\sin^2\left(\frac{1}{2}\theta\right)\rho_0^2 U^5 L b}{c_\infty |\vec{x}|^2} S(\omega) \tag{1.12}$$

where θ is the observer angle from the trailing edge relative to the plane containing the trailing edge, positive downstream. This result was similar to that obtained by Ffowcs-Williams and Hall [9], most notably in the agreement regarding the directivity and the velocity scaling.

The source term $\phi_{pp}(0, \omega)$ can be further broken down to be expressed as [1]:

$$\phi_{pp}(0, \omega) = \frac{1}{\pi} l_p(\omega) S_{pp}(\omega) \tag{1.13}$$

where $S_{pp}(\omega)$ is the autospectrum of the fluctuations and $l_p(\omega)$ is the spanwise correlation length scale of the fluctuations, which can be found by integrating the spanwise cross spectrum $S_{pp}(\Delta x_3, \omega)$ of the fluctuations normalized by their autospectrum with respect to Δx_3:

$$l_p(\omega) = \int_0^\infty \frac{S_{pp}(\Delta x_3, \omega)}{S_{pp}(\omega)}\, d\Delta x_3 = \int_0^\infty \gamma(\Delta x_3, \omega)\, d\Delta x_3 \tag{1.14}$$

While further work was done on this topic, such as that of Howe [13], who combined the theories of Ffowcs Williams *et al.* [9] and Amiet [8] to produce a more general approach that requires measurement of both the boundary layer mean velocity field and turbulent wake mean velocity field, Amiet's method is one of the more useful methods for experimentalists and engineers. Amiet's approach is typically used in practical applications because measurements of the force on the fluid by the surface (a direct consequence of the pressure fluctuations on the surface from the turbulent boundary layer) are much easier to acquire experimentally, and critically, does not require solving for a complicated Green's function. The practicality and relative simplicity of Amiet's approach thus makes it a more ideal theoretical method for performing trailing edge noise predictions. Nonetheless, the work of Ffowcs Williams and Hall was still useful, as it provided insight into the directivity and velocity scaling of trailing edge noise.

1.3 The Empirical Prediction Method of Brooks, Pope, and Marcolini

Some experimentalists choose to pursue a semi-empirical approach to the prediction of trailing edge noise. Brooks, Pope, and Marcolini [4] employed one such approach. Previous studies had shown that knowledge of the mean turbulent boundary layer characteristics was not enough to accurately predict the trailing edge noise; in particular, Reynolds number and angle of attack affect trailing edge noise beyond their effect on the boundary layer thickness. The group ran a series of NACA 0012 airfoils through a test matrix of various angles of attack, chord lengths, and speeds, with tripped and naturally-developing boundary layers on each side of the airfoil, in an anechoic open-jet tunnel at NASA Langley. Using a Strouhal number-based approach for curve-fitting 1/3 octave SPLs, they derived a series of curve-fit relations that were dependent on the parameters δ_i^*, M, α^* (the angle of attack corrected to give the same amount of lift in free air as measured in the tunnel), Re_c, f, and U_∞, which were based on previous theoretical studies. This method, colloquially known as BPM, has

been shown to yield accurate predictions in the years since its formulation and continues to be used today [1].

The BPM equations take the following form:

$$SPL = 10\log\left(10^{SPL_p/10} + 10^{SPL_s/10} + 10^{SPL_\alpha/10}\right) \tag{1.15}$$

in which SPL_α, SPL_p, and SPL_s represent the angle of attack, pressure side, and suction side contributions to the overall noise, respectively. These contributions take the following form:

$$SPL_p = 10\log\left(\frac{\delta_p^* M^5 L \bar{D}_h}{r_e^2}\right) + A(a_p) + (K_1 - 3) + \Delta K_1 \tag{1.16}$$

$$SPL_s = 10\log\left(\frac{\delta_s^* M^5 L \bar{D}_h}{r_e^2}\right) + A(a_s) + (K_1 - 3) \tag{1.17}$$

$$SPL_\alpha = 10\log\left(\frac{\delta_s^* M^5 L \bar{D}_h}{r_e^2}\right) + B(b_s) + K_2 \tag{1.18}$$

In the above equations, L is the spanwise length of the edge wetted by the flow, $\bar{D}_h$ is a directivity factor that is based on the observer location, r_e is the distance from the trailing edge to the observer corrected for thin shear layer refraction, $A()$ and $B()$ are spectral shape functions that are symmetric about their peaks, a_i and b_i are the absolute values of the logarithm of the ratio of St_i to its peak value, K_i are amplitude functions that set the level of the spectral shape functions, and ΔK_1 is a correction for the pressure side contribution at nonzero angles of attack. Definitions for St, $A()$, $B()$, K_i, and ΔK_1 based on the geometry of the experiments performed in this work will be given in Section 3.3.5.

While BPM only measured the noise emitted from NACA 0012 airfoils, which are perfectly symmetrical and not used often in practical applications, it is common to use the method for rough estimates using measured or computed boundary layer parameters for the airfoil in question. It is a good method of quickly predicting noise, but as with any extrapolation

method, its accuracy necessarily decreases the further the applied conditions are from the modelled conditions. It would be better to know the actual surface pressure spectrum beneath the boundary layer of the airfoil or other edge noise source and use that directly for noise predictions. For this reason, despite its more complex nature, Amiet's method and its derivatives continue to be used today.

1.4 Experimental Validation of Trailing Edge Noise Prediction Theory

An early experimental validation confirming the theories purported by Amiet, Ffowcs Williams and Hall, and Howe as applied to a two-sided airfoil was done by Brooks and Hodgson in 1981 [14]. Brooks and Hodgson ran experiments at NASA Langley using a NACA 0012 airfoil embedded in a uniform turbulent flow inside an anechoic chamber, with small embedded transducers embedded in the surface and eight condenser microphones to measure the radiated far field noise. They tested the dependence of the radiated noise on the angle of attack, the flow speed, and the bluntness of the trailing edge. Using Howe's theoretical model [13] and empirical relations for the convection velocity and wavenumber-frequency wall pressure spectrum of surface pressure as functions of sensor separation, they found that they were able to predict the noise directly overhead of the edge quite well in the range $f = 600 - 4500$ Hz and with zero angle of attack. It was also confirmed that the velocity scaling and directivity predicted by Amiet and Ffowcs Williams and Hall were accurately reflected in a real flow over a two-sided airfoil, with the group finding an empirical velocity scaling of $U^{5.07}$ for the sharp trailing edge and $U^{5.3}$ for a blunt trailing edge with a thickness of 2.5 mm. This shows that theoretical prediction models begin to perform less well in the case of a blunted trailing edge, which is to be expected. Finally, they showed that changing the angle of attack tended to not reduce overall sound levels, but did shift the peaks in the trailing edge noise spectrum to lower frequencies due to the angle of attack shift altering the pressure spectra on each side of the airfoil and causing a greater pressure jump at lower frequencies.

Roger and Moreau [6] sought to confirm the applicability of the expression derived by Amiet with a correction to the generalized lift function to correct for the leading edge contribution

derived by themselves and Wang [15]. Using pressure taps mounted in a controlled-diffusion airfoil with a rounded leading and trailing edge and a single far field microphone on a rotating mount, they measured the cases of a turbulent attached boundary layer, laminar boundary layer flow with Tollmien-Schlichting (T-S) instability waves, and a vortex shedding regime. They found that while both Amiet's and Howe's equations predicted the same order of magnitude of the total trailing edge noise perpendicular to the flow, the directivity pattern of the corrected Amiet equation was found to match the experimental data much better than that of Howe, which is attributable to Howe's model having less similarity to the real world formulation of the problem, as it assumes a half plane, while Amiet's model accounts for finite length of the airfoil. They also confirmed the adequacy of using the measured wall pressure spectrum to predict the far field noise.

The leading-edge correction derived by Roger and Moreau [15] used the Schwarzschild solution to the half-plane problem, but performed on an opposite semi-infinite plane, starting at the leading edge and continuing downstream. The noise scattered by the leading and trailing edge of the flat plate in Amiet's method (and a real airfoil) affect each other; when trying to perform the Schwarzschild procedure at the trailing edge, the leading edge noise needs to be accounted for, and vice versa, in an oscillating manner that would theoretically need to be performed infinitely many times. However, Roger and Moreau found that simply the first two iterations of this procedure were enough to adequately predict the noise and directivity, and derived an expression for a leading edge correction.

Herrig *et al.* [16] performed measurements of trailing edge noise on a NACA 0012 airfoil inside a non-aeroacoustic wind tunnel. They compared measurements from surface pressure sensors installed very near the trailing edge with measurements from the Coherent Particle Velocity (CPV) method. They confirmed the validity of a RANS-based code (Rnoise) used to predict the point frequency spectra, and found an exponential decay model for the coherence between spanwise microphones, which is most accurate at $\alpha = 0°$ between $f = 200 - 2000$ Hz. This coherence can be used to calculate the spanwise length scale of the wall pressure fluctuations using Equation (1.14).

Herrig *et al.* also explored the effect of placing surface pressure microphones too close to the trailing edge. Doing so can allow the trailing edge noise to affect the readings of the surface pressure microphones, contaminating the signal; this can not only increase the measured S_{pp}, but also the measured l_p [16], which will cause Amiet's method to over-predict the sound. They observed that changing the angle of attack of the airfoil altered the frequency spectra primarily in ranges that were dominated by trailing edge noise, an effect unaccounted for by Amiet's method, which considers an airfoil at zero angle of attack. It was shown that even in a non-aeroacoustic wind tunnel, trailing edge noise can be predicted using surface pressure measurements. This is primarily because the hydrodynamic fluctuations measured by the surface pressure microphones are far louder than any tunnel background noise.

1.5 Models of Surface Pressure Wavenumber-Frequency Spectra

Amiet's prediction method requires, as an input, the wavenumber-frequency spectrum of the surface pressure fluctuations $\phi_{pp}(k_1, k_3, \omega)$. As measurement of the surface pressure spectrum can be cumbersome, it is useful to have a model with which to predict the surface pressure wavenumber-frequency spectrum using macroscopic flow parameters, such as U_c, δ, δ^*, etc. Several such methods have been explored.

The wavenumber-frequency wall pressure spectrum is the Fourier transform in time and space of the surface pressure field. Turbulent eddies in the boundary layer contributing to the surface pressure spectrum will have an associated time scale and length scale, which correspond to frequencies and wavenumbers in the Fourier domain. Thus, the wavenumber-frequency wall pressure spectrum is a full statistical description of the full wall pressure field.

The spectrum of a single microphone signal only reveals frequency content of the signal, and thus it is useful to show the wavenumber content that makes up each frequency component of the pressure signal. The wavenumber frequency wall pressure spectrum tends to have a primary and secondary lobe when plotted for a constant frequency, centered around the convective wavenumber $K = \omega/U_c$ and the acoustic wavenumber $k = \omega/c$. This plot tends to take the form shown in Figure 1.3.

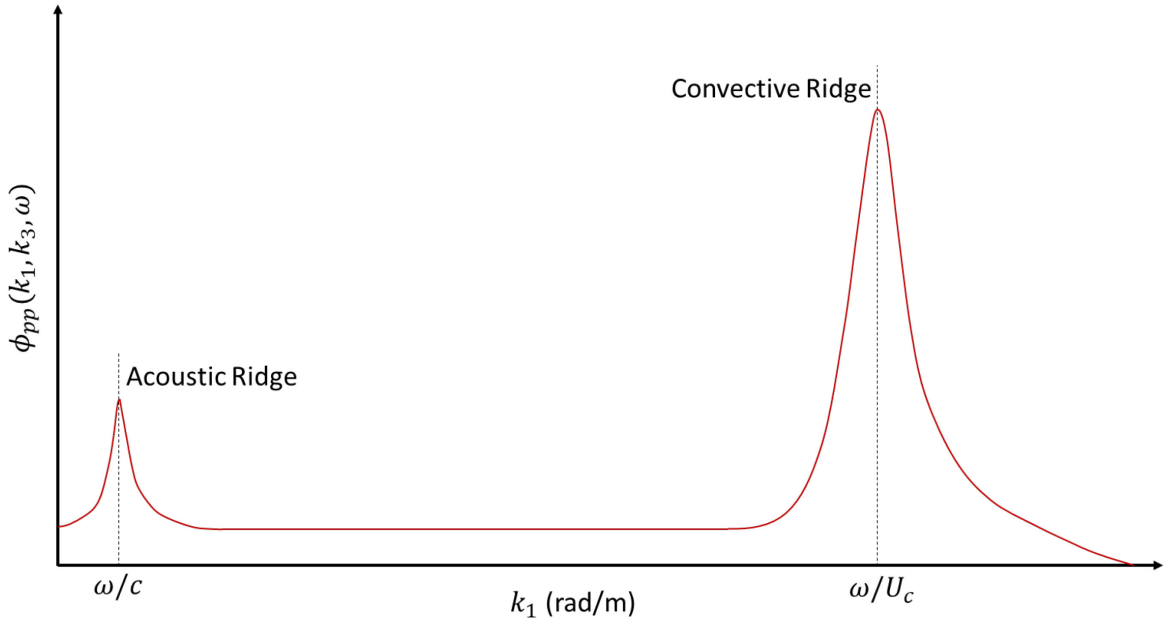

Figure 1.3, Form of wavenumber-frequency wall pressure spectrum at constant frequency.

When the above plot is shown in the $k_1 - k_3$ plane, circular contours form around the origin ($k_1 = k_3 = 0$) and ellipsoid contours stretched in both k_3 directions form around the convective ridge. This shows that streamwise convective wavenumbers are the dominant range of wavenumber contributions to the frequency spectrum. Many attempts have been made to model the acoustic region of the wavenumber-frequency wall pressure spectrum, but it remains near impossible to measure because any measurement made by a microphone will be thoroughly dominated by the convective ridge. Thus, it is difficult to assign values to empirical constants.

An early model of the wavenumber-frequency wall pressure spectrum was obtained by Corcos [17]. By curve fitting measured space-time correlation data in turbulent boundary layers, Corcos produced the following model as written by Howe [18]:

$$\phi_{pp}(k_1, k_3, \omega) = \frac{\phi_{pp}(\omega)}{\pi^2} \frac{\alpha_1}{\left[1 + \alpha_1^2 \left(k_1 - \frac{\omega}{U_c}\right)^2\right]} \frac{\alpha_3}{[1 + \alpha_3^2 k_3^2]} \tag{1.19}$$

where $\alpha_1 = 9U_c/\omega$ and $\alpha_3 = 1.4U_c/\omega$. This model is algebraically quite simple and is thus attractive for use with measured or predicted single point spectra. It provides a good measure of the spectrum in the region of the convective ridge but tends to overpredict the low wavenumber region of the spectrum.

Another very common model of the wavenumber-frequency wall pressure spectrum is the Chase spectrum [10,19]. Chase sought to derive a relation for the entire incompressible, inviscid regime, and in particular believed that the boundary layer thickness δ played a major role in determining this relationship. His relation is defined for low Mach number flow over a smooth, rigid flat plate with zero pressure gradient. He also assumed that the stream was homogeneous in the x_1 direction, as to ignore the changing boundary layer thickness, and thus define the surface pressure spectrum solely as a function of $k_1, k_3,$ and ω. The Chase spectrum is given by:

$$\phi_{pp}(k_1, k_3, \omega) = \frac{\rho_0^2 u_\tau^3}{[K_+^2 + (b\delta)^{-2}]^{\frac{5}{2}}} \left\{ C_T K^2 \left[\frac{K_+^2 + (b\delta)^{-2}}{K^2 + (b\delta)^{-2}} \right] + C_M k_1^2 \right\}$$
$$K_+^2 = \left(\frac{\omega - U_c k_1}{h u_\tau} \right)^2 + K^2, K^2 = k_1^2 + k_3^2 \tag{1.20}$$

where u_τ is the friction velocity $\sqrt{\tau_f/\rho_0}$ and C_T, C_M and b are empirical constants. Chase proposed values of $h = 3, C_T h = 0.014, C_M h = 0.466,$ and $b = 0.75$ based on experimental data. Here, C_M and C_T (and their respective terms) represent the contribution of the mean shear and the pure turbulence.

As is to be expected with any prediction method for a necessarily unpredictable statistic, there are limitations to the applications of this prediction method. In the derivation of the model, Chase assumed an incompressible medium, which captures the convective region

well, but underpredicts the acoustic region, as compressibility is required to have an acoustic region. However, as will be explained later, this particular shortcoming is of little detriment to the usefulness of its application in this work.

Although the form of Chase's model is frequently used in prediction models, the integrated form of Chase's spectrum is not the best representative a zero-pressure gradient turbulent boundary layer. A different empirical model conceived by Goody (2004) [20], though not actually a wavenumber frequency wall pressure spectrum model, is simply a frequency wall pressure spectrum model, which is similar in form to that of Chase, but integrated over all k_1 and k_3. The reduced complexity of this model makes it much easier to derive empirical constants for. To use Goody's model as a wavenumber frequency wall pressure spectrum, it can be applied to the normalized form of the Chase model, spreading the single-point pressure predicted by the Goody spectrum across the convective ridge modelled by Chase. Another way to think of this is as integrating the Goody model in reverse, revealing the substructure of wavenumbers that make up the integrated form.

Goody's model is based on the notion that the Reynolds number affects the ratio of time scales between the outer layer and inner layer of the turbulent boundary layer. Using both his own and several others' spectral data of surface pressure measurements, he modified the Chase spectrum in the form presented by Howe [18] to ensure $\phi_{pp}(\omega) \sim \omega^{-5}$ decay as $\omega \rightarrow \infty$, as seen in experimental data, and changed other empirical parameters in the model to better agree with the experimental data, establishing an emphasis on the time scales of the outer and inner layers. The model, based on traditional boundary layer scaling variables like Chase's, was determined to be:

$$\frac{\phi_{pp}(\omega)U_e}{\tau_w^2\delta} = \frac{3\left(\frac{\omega\delta}{U_e}\right)^2}{\left[\left(\frac{\omega\delta}{U_e}\right)^{0.75} + 0.5\right]^{3.7} + \left[(1.1R_T^{-0.57})\left(\frac{\omega\delta}{U_e}\right)\right]^7} \tag{1.21}$$

with R_T, the ratio of outer to inner time scales, defined as:

$$R_T = \frac{u_\tau \delta}{\nu}\sqrt{\frac{C_f}{2}} \tag{1.22}$$

This model, like Chase's, predicts the spectrum beneath a two-dimensional zero-pressure-gradient flow over a flat plate. Additionally, Goody presented an empirical model for R_T's dependence on Reynolds number:

$$R_T = 0.11 Re_\theta^{3/4} \tag{1.23}$$

This relation was shown to be valid for a wide range of Reynolds numbers, confirming that Goody's surface pressure spectrum model was accurate for such a range.

In 1997, Graham [21] compiled a list of models of the wavenumber-frequency wall pressure spectrum, including Corcos' and Chase's, and gave a nondimensional form of the full Chase model normalized on the single point spectrum derived from Chase's model. Graham gives this single point spectrum as:

$$\begin{gathered}\phi_{pp}(\omega) = \left[\frac{2\pi h \rho^2 u_\tau^4}{3\omega(1+\mu^2)}\right](C_M F_M + C_T F_T) \\ F_M = \frac{[1+\mu^2\alpha^2+\mu^4(\alpha^2-1)]}{[\alpha^2+\mu^2(\alpha^2-1)]^{3/2}} \\ F_T = \frac{3(1+\mu^2)(1+\alpha^2)}{2\alpha^3} \\ \alpha = \sqrt{1+\left(\frac{U_c}{b\omega\delta}\right)^2} \quad \mu = \frac{hu_\tau}{U_c}\end{gathered} \tag{1.24}$$

This form of the Chase spectrum represents the spectrum integrated over all k_1 and k_3 like Goody and can be applied to the normalized spectrum just like Goody's spectrum.

While modeling frequency-dependent surface pressure spectra can be easily experimentally validated, modeling the wavenumber-frequency spectrum is much more difficult in regions

outside the convective ridge. This is because the content measured by each microphone represents a sum of all wavenumber components at a particular frequency; low-wavenumber contributions are not only dominated by the convective ridge, but are also contaminated by tunnel and facility noise in the acoustic regime. Thus, being able to theoretically model these regions is key for making accurate predictions.

1.6 Methods of Trailing Edge Noise Reduction

The potential technical applications of studying trailing edge noise center around reducing noise. Common trailing edge noise reduction methods are bio-inspired; many owl species, such as those studied by Graham (1934) [22], are capable of extremely quiet flight. Graham studied several owl species and concluded that three features of owl wings were notable: the leading edge comb, the trailing edge fringes, and a soft downy coat over the upper surface of the wing. Since then, efforts have been made to understand why these features reduce the noise of flight and how they can be adapted to human technology.

1.6.1 Porous Airfoils

Porous airfoils reduce trailing edge noise by modifying the surface pressure field that passes over the trailing edge. The porous surface reduces the energy of the turbulence via surface friction, and therefore reduces the noise; additionally, depending on the material, some attenuation can be achieved by the structure of the porous material within the airfoil itself.

Geyer *et al.* (2010) [23] noted that the feathers of owls are more porous than that of non-stealth birds, allowing air flow more easily from the pressure side to the suction side. They constructed airfoils out of a wide range of materials to examine the effect of porosity on noise reduction. The resistivity of a porous material can be roughly stated as how easily a flow can pass through it and is inversely related to the porosity. The group observed that the reduction effect was strongest in the airfoils with higher resistivities at frequencies between 7 and 12.5 kHz, but at high frequencies the sound emission was increased, especially at lower resistivities. The increase in high-frequency noise is attributed to roughness noise from flow over the porous material.

The aerodynamic consequences of changing the material of the airfoil must naturally be studied as well. Geyer *et al.* observed that porous airfoils produce lower lift and higher drag than their solid counterparts; this is because the porous airfoil allows air to pass through it, reducing the pressure differential between the two sides of the airfoil, and the surface roughness creates additional drag. Clearly, if porous airfoils were to be made practical, some trade-off would have to be made between acoustic gains and aerodynamic losses.

Geyer *et al.* suggested that partially porous airfoils, i.e. airfoils with the section upstream of the trailing edge being replaced by a porous insert, would be a worthwhile pursuit. Carpio *et al*. (2017) [24] performed experiments with just such an airfoil, using a metal foam material for the porous insert. After confirming that the porous extent does not affect the surface pressure field upstream of the extent, concluding that the lift reduction must come from the modified pressure distribution along the extent itself, they experimented with three different metal foams, two different porous extension lengths, and varying angles of attack. Increasing the angle of attack increased noise at lower frequencies, but significantly decreased noise at higher frequencies; the airfoils with larger pore diameter (less resistivity) were more sensitive to this effect. Increasing the percentage length of the porous insert increased noise attenuation at low frequencies and low velocities, and using the shorter porous extension produced more effective noise reduction at mid-level frequencies. In general, the shorter insert performs better acoustically than the longer insert for frequencies above 1 kHz, and this effect fades as the freestream velocity increases.

Further experiments by Carpio *et al.* [25] continued to explore the effect of the porosity of the insert and characterize the aerodynamic effects of the insert. Using PIV, they reported that increasing the porosity of the material increased the boundary layer and displacement thicknesses, resulting in a decreased mean velocity, indicating higher surface drag due to the porous material. They concluded from their observations of velocity fluctuation spectra that the reduction of turbulence energy within the boundary layer was at least partially responsible for the attenuation of noise. In particular, they observed that the porous material decreased the Reynold stresses ($\rho v_i v_j$), which is one of the components of T_{ij}, the source term. This

indicates a reduction in overall turbulence velocity fluctuations. They reported that increasing the porosity enhanced the attenuation of low-frequency noise, and showed that this was because the porosity reduces the length of the vertical length scale Λ_{22}, increasing the anisotropy (and thus decreasing the coherent length) of the turbulent eddies. Lastly, they showed that the porous surface decreases convection velocity, again due to surface drag from the porous material.

Porous airfoils are debatable as a practical solution for application – the decreased aerodynamic efficiency is a major factor in determining whether or not pursuit of a commercial application is worthwhile, especially while other potential solutions that do not compromise the structural or aerodynamic integrity of the airfoil exist.

1.6.2 Finlets

Clark *et al.* (2014) [26] observed the structure of the upper coating of owl feathers with a microscopic camera and observed that the hairs rise nearly straight up before suddenly bending to align with the flow, creating a canopy similar to that of a forest. A series of experiments measuring surface pressure fluctuations beneath both unidirectional and mesh-like canopies suspended over rough surfaces showed that such a canopy was capable of reducing surface pressure fluctuations beneath it by nearly 30 dB, despite having an open-air ratio of 70%. This motivated further research when it was realized that a similar aeroacoustic device could be placed near the trailing edge to attenuate surface pressure fluctuations there, as the strength of the surface pressure fluctuations ϕ_{pp} is shown by Amiet to be directly related to the far field noise. Clark *et al.* (2017) [27] tested two different types of trailing edge treatments – a "fence"-type treatment of solid finlets aligned with the flow, and a "rail"-type treatment of cylindrical rails suspended on a slope above the trailing edge, again aligned with the flow. Far field measurements on the treated airfoils showed that the treatments were capable of reducing noise by as much as 10 dB. Clark *et al.* postulated that the mechanism by which the finlets reduce trailing edge noise was through the deformation and decorrelation of turbulent structures in the boundary layer, noting that the finlets' performance increased with increased finlet height and decreased with decreased finlet density. Decorrelation of

turbulent structures occurs because the finlets "cut" the turbulent eddies, breaking up the spanwise length scale of the serrations, and reducing this length scale reduces the magnitude of the source term, as seen in Equation (1.13).

In an investigation of the mechanism behind the far field noise reduction, Bodling and Sharma (2018) [28] simulated the finlet structure in a LES-based CFD solver. They found that the drag increase was small and on the order of the amount of extra wetted area on the wing surface due to the finlets (a result previously found by Clark *et al.* [27]), and that while a taller fence was ineffective at reducing noise at lower frequencies, it was more effective at reducing noise at higher frequencies. They observed two noise reduction mechanisms – that the larger turbulent structures were "lifted up" from the surface, which reduces the high-frequency noise produced by smaller eddies, and that the spanwise coherence is reduced, which reduces the low-frequency noise as shown in Equation (1.14). This second result is analogous to Clark *et al.*'s conclusion that the turbulent structures are "broken up". The first result is also consistent with Clark *et al.*'s observation that as the spacing between the finlets approaches zero, they begin to behave as a single blunt trailing edge.

Seeking to further understand the mechanisms of finlets' effectiveness, Afshari *et al.* (2019) [29] performed a series of experiments with a heavily instrumented flat plate with trailing edge finlets. They experimented with placing the finlets slightly upstream of the trailing edge, as suggested by Clark *et al.* [27]. They found that the trailing edge noise reduction was very sensitive to the finlet spacing. In the case of coarser finlet spacing, the surface pressure spectral density was reduced at moderate to high frequencies, and the spanwise length scale was increased. They theorized that this was due to a "channeling" effect, where the finlets increase spanwise correlation in the channels between them, an effect analogous to eddies being convected through them. This would allow for the turbulent energy of these eddies to dissipate via friction with the "channel walls". Reducing the coarseness of the spacing would increase this effect. However, when the space between the finlets becomes too small, like Clark *et al*., they observed that a shear layer forms downstream at the finlet height. This leads to an increase in the levels of the low-frequency region of surface pressure fluctuations.

However, the high frequency regime is reduced significantly, similarly to the results of Bodling and Sharma. Furthermore, the effectiveness of the finely spaced finlets was much more sensitive to distance from the trailing edge than the coarsely spaced finlets. They concluded that both effects identified by Bodling and Sharma play a role in the reduction of the trailing edge noise, with the effectiveness of each mechanic being determined by the finlet spacing.

Finlets are a promising method of reducing trailing edge noise because they can theoretically be added to an already-existing trailing edge, minimizing development costs. Overall, they have low aerodynamic impact, though they tend to be detrimental at high angles of attack; of particular note is minimal drag increase and virtually no loss of lift. Finlets are quite fragile, however, especially when they are finely manufactured. Additionally, modifying the trailing edge characteristics to optimize the reduction potential of any applied finlets is likely to be a better solution than simply attaching finlets to an already-existing system [27].

1.6.3 Serrations

Serrations are the primary tool for reducing trailing edge noise in practical applications. Like finlets, serrations are aimed at limiting the correlated spanwise loading across the edge at wavenumbers which couple with radiating acoustic waves. They accomplish this by changing the edge geometry to a smooth or discontinuous waveform.

Serrated trailing edges were first investigated theoretically by Howe (1991) [30], who proposed a prediction model for the amount of attenuation provided by a serrated trailing edge. Howe solved a problem very similar to that of Amiet's theory – a diffraction problem featuring a semi-infinite plane with infinite span, but without a straight trailing edge. Instead, the trailing edge was described by a function of x_3, with a mean value of $x_1 = 0$. Howe proposed that the dominant contributions to the radiated sound in terms of surface pressure fluctuation wavevector would be from wavenumber components for which $\vec{k}$ is normal to the radiating edge. This is analogous to the assumption of Amiet – for a straight trailing edge, the dominant wavevector contributions would be from $k_3 = 0$. Howe primarily examined a

trailing edge that varied as a sinusoid. As the dominant surface pressure fluctuations are in the range $|k_3| \leq 1/l_p$, and $l_p \sim U_c/\omega$ [13], Howe concluded that the effective wetted length of the trailing edge, l_e, was reduced even though the actual path length of the trailing edge increases. Only the regions of the sinusoid where the angle between the trailing edge and the flow is greater than 45° should radiate noise, and narrower serrations reduce the length of the regions of trailing edge that meet this criterion. For sinusoidal serrations with an amplitude h and wavelength λ, this corresponds to a reduced far field noise of $S_{pp}(\vec{x}, \omega) = S_{pp,0}(\vec{x}, \omega)/(\pi^2 h/\lambda)$, where $S_{pp,0}$ is the spectrum produced by a straight trailing edge. This expression is based on the wetted length reduction, l_e/l, where l is the wetted length of the straight trailing edge; as Equation (1.10) shows, the wetted length of the airfoil (analogous to b in Amiet's formula) directly influences the far field sound spectrum, and reducing it should therefore reduce the far field noise. Howe concluded that the best way to reduce the noise was to use serrations with sharp "teeth", with all angles of each serration at an angle of less than 45° to the mean flow.

Howe made several key assumptions to perform the analysis. First, to approximate a Green's function for the semi-infinite flat plane, he used the Green's function for such a plane with a straight trailing edge. Furthermore, he used the slender wing approximation, which is intended to be used for low aspect ratio wings, to be applied at local areas where the angle of the trailing edge is normal to the wavevector. This fails to account for the interaction between adjacent serrations, as shown by Lyu *et al.* [31]. Finally, he used the statistically frozen field assumption, which was discussed in Section 1.2.

Howe's analytical formulation showed that the far field noise was proportional to $\phi_{pp}(\omega)$, the frequency surface pressure spectrum, and that the ratio λ/h was the primary factor to which the attenuation level was sensitive. He predicted that noise at low frequencies would be largely unaffected by the serrations, as they would be too small to influence the eddies, introducing the limiting factor of $K_1 h \gg 1$, but that attenuations of high frequency noise in this region would be substantial. In the case of λ/h = 1, he predicted a high frequency noise

reduction of 8 dB. The important takeaway is the dependence of the noise reduction efficiency on the serration geometry.

Howe released a follow-up paper [32] exploring the case of sharp teeth used as serrations. He found that this sawtooth configuration of serrations could be expected to reduce the far field noise by $10\log(1+(4h/\lambda)^2)$ dB, in contrast to the $10\log(6h/\lambda)$ reduction predicted for the sinusoid serrations. Using Chase's [19] model of the wavenumber-frequency wall pressure spectrum integrated with respect to k_1 and keeping only leading-order terms, he gave the following expression for the predicted far field spectrum of a sawtooth serrated edge:

$$\frac{S_{pp}(\vec{x},\omega)}{(\rho u_\tau)^2(b/c_0)(\delta/|\vec{x}|)} = \left(\frac{C_m}{\pi}\right)\sin^2\left(\frac{\theta}{2}\right)\sin(\alpha)\,\Psi(\omega) \tag{1.25}$$

In the above expression, c_0 is the freestream speed of sound, $C_m \approx 0.1533$ is the empirical constant given by Chase [19] in Equation (1.20), θ and α are the angles from the origin to the observer with θ as defined in Figure 1.2 and α defined as $\cos^{-1}(x_3/|\vec{x}|)$, and $\Psi(\omega)$ is the nondimensional frequency spectrum associated with the serration geometry. For a sawtooth edge, this is given by:

$$\Psi(\omega) = \left(1+\frac{1}{2}\epsilon\frac{\partial}{\partial\epsilon}\right)f\left(\frac{\omega\delta}{U_c},\frac{h}{\lambda},\frac{h}{\delta},\epsilon\right) \tag{1.26}$$

Substituting A for $\omega\delta/U_c$, B for h/λ, and C for h/δ, $f(A,B,C,\epsilon)$ is given by:

$$\begin{aligned} f(A,B,C,\epsilon) &= \frac{1}{\{A^2[1+(4B)^2]+\epsilon^2\}} \\ &\times\left(1+\frac{64B^3C^{-1}A^2\left(\cosh\left\{\left(\frac{C}{2B}\right)\sqrt{[A^2+\epsilon^2]}\right\}-\cos(2AC)\right)}{\sqrt{[A^2+\epsilon^2]}\{A^2[1+(4B)^2]+\epsilon^2\}\sinh\left\{\left(\frac{C}{2B}\right)\sqrt{[A^2+\epsilon^2]}\right\}}\right) \end{aligned} \tag{1.27}$$

where $\epsilon = 1.33$ is another empirical constant. When h is zero, as for a straight trailing edge, Equation (1.26) reduces to $\Psi_0(\omega) = A^2/(A^2+\epsilon^2)^2$.

An experimental paper showing both that trailing edge noise was the dominant source of wind turbine noise for an observer near the ground and that serrations were an effective mechanism for reducing the overall noise at the observer location was published by Oerlemans *et al.* in 2009 [5]. Using a horizontal microphone array placed on the ground in front of the turbine and using a beamforming algorithm, it was shown that nearly all of the noise observed was produced during the downward motion of the blade, and from the outer 25% of the blade. This is the region at which the highest local-velocity flow occurs, and since the directivity of trailing edge noise is dominant upstream, this confirms that the dominant noise source of a wind turbine is trailing edge noise. However, contrary to Howe's prediction, the modified serrated blade was effective at reducing noise at low frequencies, and actually increased noise at high frequencies. Regardless, the overall noise level of the serrated blade was about 3 dB lower than that of the unmodified blade. As was shown by Gruber *et al.* [33], it is likely that the source of the increased high-frequency noise is the flow rushing through the serrated teeth due to the angle of attack of the blades.

Gruber *et al.* (2011) [33] performed experiments in an open-jet aeroacoustic wind tunnel on a NACA 65(12)-10 cambered airfoil with a series of 0.8 mm-thick serrated trailing edge inserts ranging from $h/\lambda = 0.167$ to 10. He observed that between 400 and 7000 Hz and with the airfoil at an angle of attack of 5°, the serrations were capable of reducing noise by up to 5 dB for an amplitude of $h = 10$ mm and up to 7 dB for an amplitude of $h = 15$ mm. The noise reduction tended to increase as λ became smaller and the serrations became sharper and narrower. Above 8 kHz, the noise was increased for all serration shapes, with a greater noise increase for wider serrations. They found that Howe's theory far over-predicted the amount of potential noise reduction from sawtooth trailing edge serrations, and confirmed the high-frequency noise increase observation of Oerlemans *et al.* [5]. Nonetheless, an overall reduction in sound level was achieved. The general transition point from noise reduction to noise increase was at the δ-based Strouhal number, $St_\delta = \omega\delta/U_c$. They theorized that the cause of the high-frequency noise increase is the flow passing between the teeth and interacting with the flow on the other side, a feature that would not be present for large low-wavenumber eddies. They confirmed this by releasing smoke on the pressure side of the

airfoil and observing its convection past a straight trailing edge and a sawtooth trailing edge. Naturally, this implies that at a high angle of attack, more high-frequency noise will be produced, reducing the effectiveness of the serrations. The group confirmed Howe's prediction that a serrated trailing edge would be ineffective if the sawtooth amplitude was smaller than the eddies. Additionally, they observed that the reduction in noise was equally sensitive to both h and λ, rather than simply their amplitude. They concluded that the turbulence at the roots and tips of the teeth was largely uncorrelated, and that there were three conditions upon which noise reduction would be dependent: $f\delta/U_\infty < 1$, $h/\delta > 0.5$, and small λ.

In his dissertation, Gruber [34] provided further data obtained from the same configurations as Gruber [33]. In this work, he also measured the surface pressure on serrations using flush pressure taps connected to microphones. These taps were mounted in a serrated edge on two adjacent serrations, with dimensions $\lambda = 9$ mm and $2h = 30$ mm. He recorded a significant increase in the surface pressure autospectrum along the serration in a hump centered at 350 Hz and ranging from 100 Hz to 2 kHz. This was attributed to acoustic backscatter from the trailing edge being measured by the microphones. As the measurement location moves downstream, the two sides of the serration approach convergence, the distance between them decreases, and this increases the radiation measured by the transducers. Additionally, Gruber measured the surface pressure coherence for microphone pairs along the edge of the serration and spanwise microphone pairs on the same serration, and compared along-the-edge serrations to direct microphone pairings on a flat plate, rather than to separate streamwise and spanwise pairs. He observed an increase in along-the-edge coherence below a frequency threshold that increased with the microphone pair's proximity to the tip. This was again attributed to backscatter, as the coherence of acoustic radiation decays far less rapidly than turbulent eddies [34]. A reduction of about 15% of the coherence in the region where trailing edge noise reductions were observed was also recorded. Significant increases in spanwise coherence were also observed with the same frequency cutoff trend observed in the along-the-edge measurements, and the same cause was attributed.

Additionally, Gruber [34] observed that the phase speed of the turbulent eddies was reduced in the frequency ranges where a noise reduction was observed. This reduction was attributed to interaction between the acoustic pressure and the boundary layer incident pressure. The reduction in phase speed indicates a reduction of the speed at which scattering of turbulent energy takes place, which was postulated as a noise reduction mechanism by Howe [32]. The coherence reduction along the edge in the frequency range of noise reduction also indicates that the correlation length l_p along the edge is decreased, which is another potential factor in the noise reduction according to Amiet's equation.

Moreau and Doolan (2013) [35] performed further experiments on sawtooth trailing edge serrations, and measured velocity fluctuations in the near-trailing edge wakes. They used a flat plate with two different geometries, $\lambda/h = 0.2$ and 0.9. They noted that both the narrow and wide serrations attenuated noise well in the low and high frequency regions, and increased noise in the mid frequency region. They concluded that the wide serrations performed better overall due to the increased attenuation at the low frequencies. This was in contrast to theory, which predicted that narrow serrations would outperform wider ones, but agreed with experimental data gathered by Chong *et al.* [36], who found that wider serrations are more effective at reducing tonal noise. The velocity fluctuation measurements showed that Howe's frozen field assumption was inaccurate – the serrations altered the behavior of the flow field around the trailing edge quite significantly, and that the noise reduction and increases observed directly corresponded with changes in the turbulent energy distribution close to the trailing edge. Moving a downstream hotwire probe in a spanwise sweep, the turbulent energy was observed to be highest at points nearest to the tip of a serration, and lowest at the roots; this is because points on the tip are closer to the measurement point, meaning the probe is closer to the boundary layer it is measuring. This means that the boundary layer stays attached longer due to the presence of the serration, another alteration to the flow field. Additionally, the narrow serrations appear to cause a mid-frequency (600-6000 Hz) increase in turbulent fluctuations, explaining the observed increase in mid-frequency trailing edge noise. They concluded that rather than the wavevector-trailing edge interaction, it was the observed alterations to the hydrodynamic field's turbulent energy

distribution that was the primary driver of the reduction capabilities of a serrated trailing edge.

Lyu *et al.* (2016) [31] sought to create an improved model for predicting the noise reduction from serrated trailing edges. Like Howe, they assumed a semi-infinite plate and a frozen turbulent field, but they solved the problem for sharp teeth, as seen in experiments, rather than a sinusoid. They used an approach similar to that of Amiet, using the Schwarzschild technique [11] to solve an edge noise problem based on a sawtooth trailing edge geometry. The study found that the serration geometry as defined by the "sharpness" of the teeth and the length of the serration relative to the size of the turbulent eddies were key factors in the potential for sound reduction, like Howe. A key difference between their model and Howe's was including the coupling effect between adjacent serrations. The acoustic field radiated by a sawtooth affects adjacent teeth, and Howe's use of the straight-edge Green's function as the model for the trailing edge was valid, but only locally. They concluded that the mechanism of noise reduction was destructive interference of the scattered pressure, caused by the sound radiating off of serrations. At low frequencies, or for wide serrations, the net effect of serration-induced phase interference can be constructive, which they posited as the reason for increased low-frequency noise in these cases. They found this destructive interference effect to be most significant at angles near that of the leading edge. However, this was not experimentally validated, as placing a microphone at upstream locations is often made difficult by the geometry of the measurement chamber – placing a microphone at this location would place it in the flow.

Using the same technique Howe used to non-dimensionalize the far field acoustic spectrum, and using the same integration and reduction of the Chase spectrum, Lyu *et al.* posited the following model:

$$\frac{S_{pp}(\vec{x},\omega)}{(\rho u_\tau^2)^2(b/c_0)} = \frac{C_m}{2\pi}\Psi(\vec{x},\omega) \tag{1.28}$$

where, as before, $\Psi(\vec{x}, \omega)$ represents the nondimensional frequency spectrum of the serration influence on the radiated sound, and is given by:

$$\Psi(\vec{x}, \omega) = \left(\frac{x_3 c}{r_e^2}\right)\left(\frac{U_c}{c_0}\right) \sum_{m=-\infty}^{\infty} \left|\mathcal{L}\left(\omega, K_1, \frac{2\pi m}{\lambda}\right)\right|^2 \frac{(\omega\delta/U_c)^4}{[(\omega\delta/U_c)^2 + (2m\pi\delta/\lambda)^2 + \epsilon^2]^2} \quad (1.29)$$

The infinite sum in Equation (1.29) is similar to that which was derived by Howe in the process of coming to Equation (1.26). A major difference between the two models is the introduction of the far field sound gust response function $\mathcal{L}$, a concept that mirrors Amiet's idea of the airfoil response function. Lyu *et al.* showed that a second order approximation of this term was adequate for prediction of trailing edge noise from both wide and narrow serrations; however, it is a very complex function that requires an iterative solver. For the full form of $\mathcal{L}$, the reader is referred to Reference [31].

The model predicted overall reductions much lower than those of Howe, and which agreed much better with experimental data, representing a significant amount of progress in the theoretical understanding of trailing edge serrations. Another advantage to their model is its validity at any Mach number, since Howe's model neglected the effects of convection and therefore is only valid at low Mach numbers. Their model failed to explain the high-frequency noise increase that was observed by Gruber *et al.* [33], which suggests that it needs additional refinement with more flow parameters incorporated.

1.6.4 Summary of Trailing Edge Noise Reduction Methods

All of the techniques mentioned in this section are reliant on modifying the way the turbulent boundary layer interacts with the trailing edge. All three are shown to change the structure of the boundary layer in some way. However, particularly with serrations, there is much to be learned regarding modification of the surface pressure spectrum near the trailing edge, especially since they are the most commonly used method of reducing trailing edge noise. As shown, the common assumption of similarity between a straight trailing edge and a serrated trailing edge is inaccurate, and it is necessary to understand just how the serrations

affect the surface pressure spectrum to maximize the potential of trailing edge noise reduction.

1.7 Objective

The objectives of this work are as follows:

- Understand the noise produced by an undercut step trailing edge in a wall jet tunnel and relate it to the production of trailing edge noise for fundamental studies of the sound source and its control.
- Assess the impact of serrations on the unsteady surface pressure and the noise produced by the undercut edge.
- Evaluate the variation of the surface pressure spectrum and coherence between points on a single serration and across the serrated edge.

Amiet's theory is based on the turbulent boundary layer's manifestation as surface pressure fluctuations; to explore the validity of the statistically frozen flow assumption, surface pressure measurements at various points along the serrated trailing edge, including the teeth themselves, have been made. These are compared to the pressure field for a straight trailing edge and used to show that the flow field is indeed affected by the presence of the serrations.

Chapter 2. Apparatus and Instrumentation

In this section, the facilities and instruments used for the experiments will be described.

2.1 Wall Jet Tunnel

All of the experiments, aside from some microphone calibrations, were performed in the anechoic wall jet tunnel at Virginia Tech. This facility, built in 2017-2018, is the successor to a previous facility, which was originally intended to be a temporary structure [37]. Experiments in the old facility (including the work in references [26,27,38]) have proven the utility of the anechoic wall jet design for aeroacoustic research.

2.1.1 Wall Jet Tunnel Geometry

The wall jet tunnel at Virginia Tech comprises a driving fan, settling chamber, contraction nozzle, and anechoic chamber, with the flow exhausting to the ambient outside the anechoic chamber. The driving fan is a Cincinnati Fan model HP 8D20, capable of pushing 0.945 m^3/s of air [37]. It is equipped with an SSA-8 steel discharge silencer, which reduces broadband noise significantly, up to 10 dB [37]. This blower is capable of producing nozzle velocities up to $U_j = 70$ m/s.

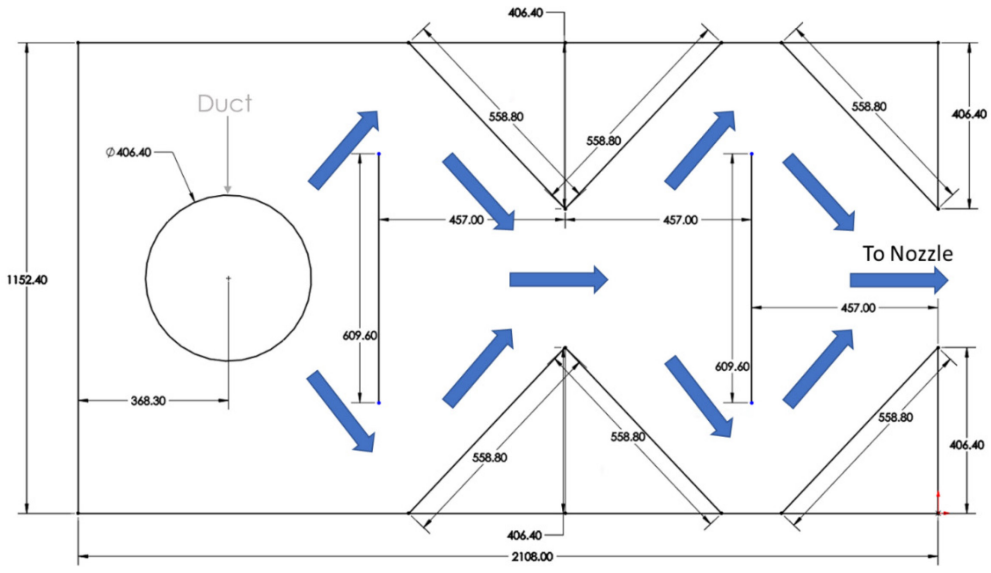

Figure 2.1, Wall jet settling chamber internal structures, top-down view.

After the flow leaves the settling chamber it is passed into the nozzle. The nozzle is a horizontally-oriented contraction chamber that vertically narrows the flow until it passes through the nozzle, a 12.7 mm (1/2") x 1206.75 mm slit [37]. The slope of each of the contraction chamber's walls is defined by a cubic function and prescribed inflection point, which is a common method of wind tunnel square and 2D nozzle design developed by Morel [39] and furthered by Fang *et al.* [40]. The method is designed to eliminate separation in the tunnel flow, producing a clean, quiet flow, and maximize uniformity in the test section [39]. While the previous facility used a splice into a rounded edge for the upper side of the nozzle, a piece of aluminum angle bracket has been added to the top of the nozzle in the new tunnel to ensure that the flow separates from the upper lip of the nozzle instead of producing a Coanda effect [37].

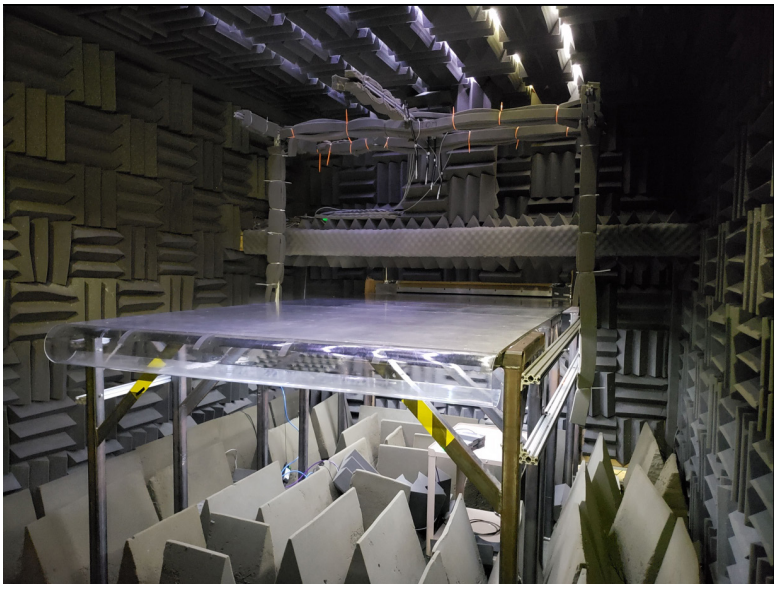

Figure 2.2, Wall jet anechoic chamber.

The flow passes through the rectangular nozzle exit and exhausts in a generally uniform manner across the 3.048x1.524 m (x_1, x_3) flat aluminum plate that serves as the "wall". The inside of the anechoic chamber, which has dimensions 4.572x2.744x3.098 m (x_1, x_2, x_3), contains the test section, a horizontal and vertical baffle to help shield the microphones from jet noise from the nozzle, and an overhead gantry made from 25.4 mm (1") 1010 80/20

aluminum beams from which to mount far field microphones. This gantry provides the means to mount microphones in a linear array spanwise or streamwise, or some combination of the two if desired. All surfaces aside from those comprising the support structure for the wall are acoustically treated with foam.

2.1.2 Characteristics of Wall Jet Flow

In a wall jet flow, there are two primary regions: the inner boundary layer, which forms much like a traditional boundary layer along the plate, and a mixing layer between the stagnant air in the anechoic chamber and the top of the inner layer. The inner and outer layers of the wall jet flow are self-similar over a wide range of Reynolds numbers when normalized on U_m, the local maximum velocity, and $y_{1/2}$ or δ, the height above the wall at which the local velocity in the mixing layer is half of U_m or the inner layer thickness [41]; this makes the task of predicting the flow characteristics at a given location trivial once the tunnel has been calibrated.

To calibrate the tunnel, flat head pitot tube measurements were taken of the velocity profile at different x_1 locations along the plate. The data was calibrated and collapsed well using U_m and $y_{1/2}$, which can be seen in reference [37]. The power law relations for wall jet velocity profiles proposed by Narasimha *et al.* [42] and developed by Wygnanski *et al.* [43] are as follows:

$$\frac{U_m}{U_j} = A_U Re_j^{n+1} Re_x^n \tag{2.1a}$$

$$\frac{\delta^*}{b} = A_\delta Re_j^{p-2} Re_x^p \tag{2.1b}$$

$$\frac{y_{1/2}}{b} = A_y Re_j^{m-2} Re_x^m \tag{2.1c}$$

$$\delta = A\delta^* \tag{2.1d}$$

$$\theta = B\delta^* \tag{2.1e}$$

In the above equations, Re_j is the Reynolds number based on the nozzle height b and the jet velocity U_j, Re_x is the Reynolds number based on the distance from the nozzle to the measurement point and the jet velocity, $n, p,$ and m are power law empirical constants, and A_U, A_δ, A_y, A, and B are empirical coefficients. The empirical constants are determined from a multitude of velocity profiles taken at different nozzle exit velocities and streamwise locations along the plate, and are given in the table below [37].

Table 2.1, Self-similarity coefficients for Virginia Tech wall jet tunnel.

$\boldsymbol{n}$	-0.4684
$\boldsymbol{p}$	0.9232
$\boldsymbol{m}$	0.9649
$\boldsymbol{A_U}$	1.497
$\boldsymbol{A_\delta}$	0.0049
$\boldsymbol{A_y}$	0.1972
$\boldsymbol{A}$	16.012
$\boldsymbol{B}$	0.8387

With these relations, the values of U_m, δ^*, $y_{1/2}$, δ, and θ can be easily predicted for a given test location given b, U_j and ν, the kinematic viscosity of the flow, which can be estimated from the flow's temperature and density using the Sutherland equation.

A key advantage offered by a wall jet facility is the ability to place microphones wholly outside of the flow. This makes the wall jet flow extremely useful for acoustic applications, as the microphone data does not have the acoustic contamination from the microphones being mounted in the flow (see Ref. [1]). The sound from the wall jet test section must still pass through the mixing layer; however, any shear layer corrections are assumed to be negligible at the low speeds considered in this study.

2.1.3 Experimental Conditions

In these experiments, data were taken from speeds of $U_j = 15$ m/s and $U_j = 20$-70 m/s in increments of 10 m/s. Equations (2.1a-e) predict the following values of these parameters at the location of the trailing edge, which is 1.283 m downstream of the nozzle. The values of ambient temperature and pressure must be known to compute the ambient density, which is used to estimate the viscosity. Table 2.2 reports the boundary layer parameters for the straight trailing edge experiments based on ambient conditions on the day of testing, with $p_\infty = 94.327$ kPa and $T_\infty = 295.2$ K.

Table 2.2, Estimated boundary layer parameters for wall jet flow in experimental conditions, straight trailing edge conditions.

U_j (m/s)	U_m (m/s)	δ (mm)	δ^* (mm)	θ (mm)	$y_{1/2}$ (mm)
15	4.671	16.76	1.047	0.878	111.5
20	6.343	16.04	1.002	0.84	109.3
30	9.761	15.07	0.941	0.789	106.2
40	13.25	14.42	0.9	0.755	104.1
50	16.80	13.93	0.87	0.73	102.5
60	20.40	13.55	0.846	0.71	101.2
70	24.03	13.23	0.826	0.693	100.1

The analysis was repeated for each of the trailing edge testing ambient conditions, and it was found that the maximum normalized standard deviation of the five estimated parameters $\left(\frac{\sigma(\phi)}{\phi}\right)$ was 0.044%. Thus, it will be assumed that the boundary layer parameters remain constant for all tests.

2.2 Microphones and Data Acquisition

To capture the surface pressure spectrum and far field noise, various microphones were used. Microphones measure pressure fluctuations and output a voltage signal by measuring the capacitance of a cavity created by the microphone's diaphragm, usually a very thin piece of metal, and a charged metal wall inside the microphone.

Bruel & Kjaer (B&K) Type 4190 1/2” microphone-preamplifier units were used in the far field and in the beamforming array. Knowles FG-23329 microphones were used for all surface pressure measurements. B&K Type 4138 1/8” microphones were used for calibration of the Knowles microphones and validation of their functionality within the frequency range of interest.

2.2.1 Far Field – B&K 1/2” Microphones

B&K Type 4190 microphones were used for far field measurements. These microphones were chosen for their excellent free field response; the response is relatively flat at 0 degrees incidence, meaning that the microphone is pointed directly at the source, up to 20 kHz [38]. As our source is a trailing edge, it is a compact location that can be easily identified and aligned with.

Figure 2.3, B&K Type 4190 1/2" microphone-preamplifier unit.

The microphones are purchased as units from Bruel & Kjaer pre-attached to Type 2669-L preamplifiers. They are mounted upon the overhead gantry shown in Figure 2.2. Aluminum rods with plastic microphone holders are attached to the gantry using rubber-lined ring clamps that screw in to the 80/20 material of the gantry, as shown below:

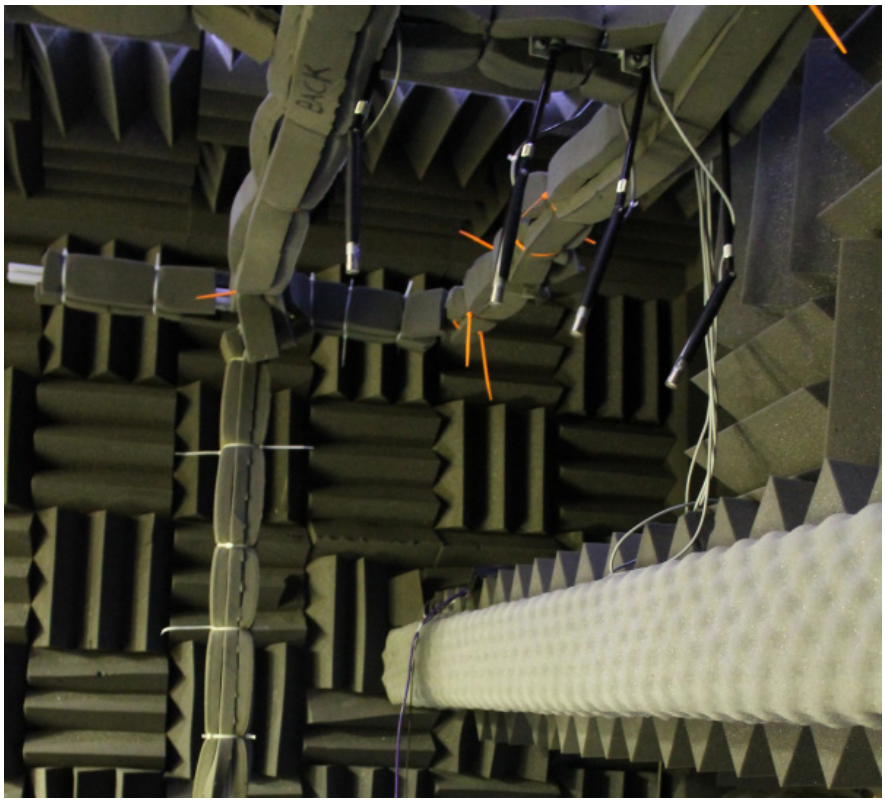

Figure 2.4, B&K Type 4190 microphones mounted on gantry.

The microphones are mounted in an arc to capture a range of different measurement locations. Full geometries of the mounting locations will be given in the sections regarding trailing edge geometry.

2.2.2 Surface Pressure – Knowles FG-23329-P07 Microphones

The Knowles FG-23329 microphone was chosen for surface pressure measurements due to its physically small size and flat response. The microphone body is 0.101” in diameter and 0.101” tall. The -P07 version of the microphones are pre-wired, meaning the signal, power, and ground wires were soldered to the microphone by the manufacturer and wrapped in a shielded cable. They have a nominal sensitivity of 33.0 $\pm$ 3.0 dB re 1 V/Pa between 100 Hz and 10000 Hz, and a pinhole diameter of 0.76 mm (0.030”) [44].

The microphones were assembled into two boxes. Each box consists of ten microphones wired to a breadboard for power and to externally mounted BNC female plugs, which can be modularly used via BNC cables to connect to our data acquisition system. Each microphone's cable shield is connected to the power supply ground to curtail interference from any intermittent electrical signal.

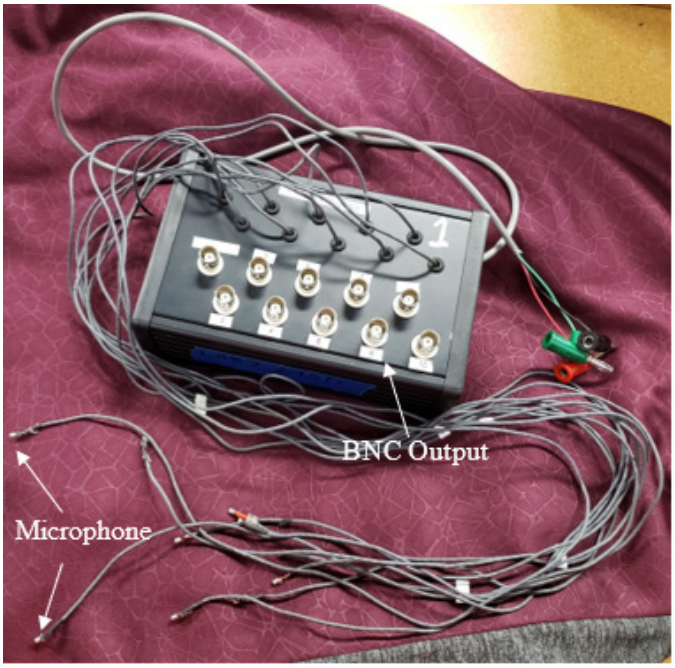

Figure 2.5, Knowles microphone box.

The breadboard is connected to the lead wires, which can be seen in Figure 2.5 as the large gray wire that terminates in three banana plugs. These plugs are connected to the power supply, which supplies 2.8 V to power the breadboard, which distributes the power to the microphones.

2.2.3 Surface Pressure – B&K 1/8" Microphones

The final type of microphone used was the B&K 4138 1/8" microphone. These are paired with B&K 2670 preamplifiers.

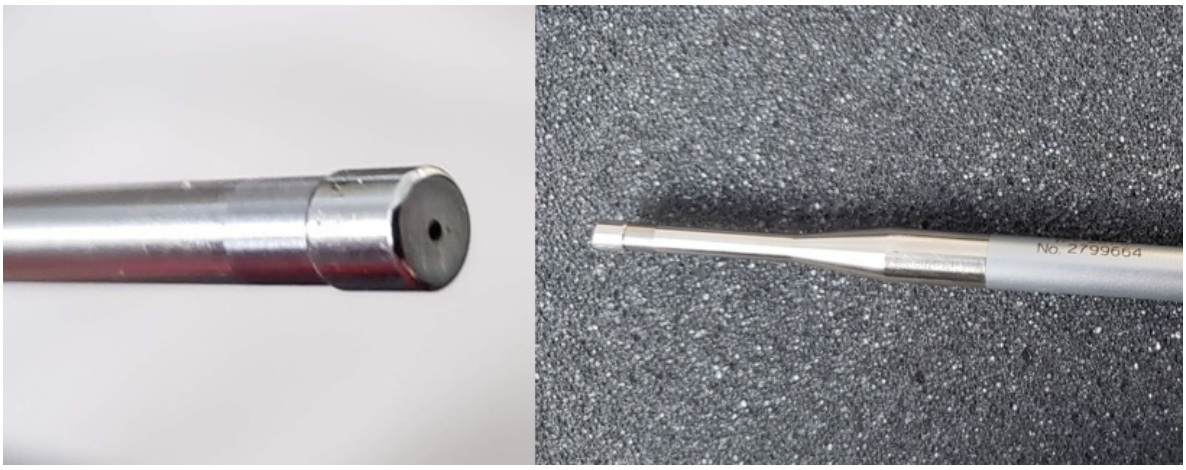

Figure 2.6, B&K Type 4138 microphone-preamplifier unit with pinhole cap.

These microphones have a flat frequency response up to 140 kHz [38] and are thus ideal for use in calibration of the Knowles microphones and ensuring that the Knowles data can be treated with high confidence in its accuracy. These were not used in large numbers because of their large size relative to the Knowles microphones, meaning a higher spatial resolution could be achieved by using the Knowles microphones.

2.2.4 Data Acquisition System and Processing

All pressure data were acquired using Bruel & Kjaer Type 3050 DAQs and B&K Pulse 14 software. Both the three-channel module and six-channel modules were used; microphone data were acquired using a series of six-channel modules and tunnel temperature and dynamic pressure data were collected using a three-channel module. These DAQs were chosen as front-end instrumentation because of their high sample rate and compatibility with the microphone equipment. The B&K 4190 and 4138 can connect to the DAQs using the UA-2101 200V microphone front panel. This panel is capable of providing the polarization voltage which drives the condenser microphones' function, as well as reading the microphone's serial number and nominal sensitivity. The Knowles FG-23329 and other data are acquired using the UA-2100 front panel, which contains six BNC ports. Data were sampled at 65536 Hz, well above the Nyquist frequency for the acoustic range (20 – 20,000 Hz), ensuring that no aliasing would occur in the spectra. To reduce uncertainty, all

microphone time series were divided into records of $N = 8192$ samples and processed with 50% record overlap; additionally, Hanning windows were applied to each record to reduce spectral leakage in comparison with a square window. This gives a frequency resolution of 8 Hz, which is more than fine enough for a study of broadband noise. The equation for determining the confidence interval of a power spectral density estimator is given by [1,45]:

$$\delta_{95} = \frac{2}{\sqrt{n_d}} \tag{2.2}$$

where δ_{95} is the 95% confidence nondimensional averaging uncertainty and n_d is the number of records, in this case 511. The 95% confidence interval is then given by [45]:

$$\left[(1 - \delta_{95})\hat{G}_{xx}(f)\right] \leq G_{xx}(f) \leq \left[(1 + \delta_{95})\hat{G}_{xx}(f)\right] \tag{2.3}$$

where $\hat{G}_{xx}(f)$ is the estimated power spectral density. It is expected that 95% of estimates of the power spectral density will lie within this range. For the processing method outlined above, $\delta_{95} = 0.0885$; this corresponds to a dB 95% confidence interval of $\delta G_{xx,dB}(f) = \pm 0.366$ dB.

2.3 Microphone Calibration

The sensitivity of a microphone relates the voltage signal it outputs to the pressure data which it is recording. The microphone must thusly be calibrated to establish the transfer functions by which the pressure data can be determined from the voltage data. While some calibration factors for our microphones were provided by the manufacturers, other analyses were performed based on the geometry and frequency response of the microphones used. These steps are critical to obtaining and understanding the signal measured by the microphone. Two analyses must be done to account for spatial averaging and frequency response.

2.3.1 Microphone Spatial Averaging

Consider a plane wave in an acoustic medium traveling in the x_1 direction, as shown in Figure 2.7. A circular microphone with diaphragm radius R measures the total pressure

applied to its diaphragm as a spatial average of the pressure at each point on the diaphragm. A microphone aligned perfectly normal to the propagation direction of this plane wave would experience the entirety of the wave's pressure at once, and thus the microphone signal would perfectly capture that wave, as the average pressure across the diaphragm would be equal to the wave pressure.

However, to avoid disturbing the flow with the surface pressure microphones, the surface pressure microphones must be mounted flush with the surface, oriented upwards, as shown in Figure 2.7.

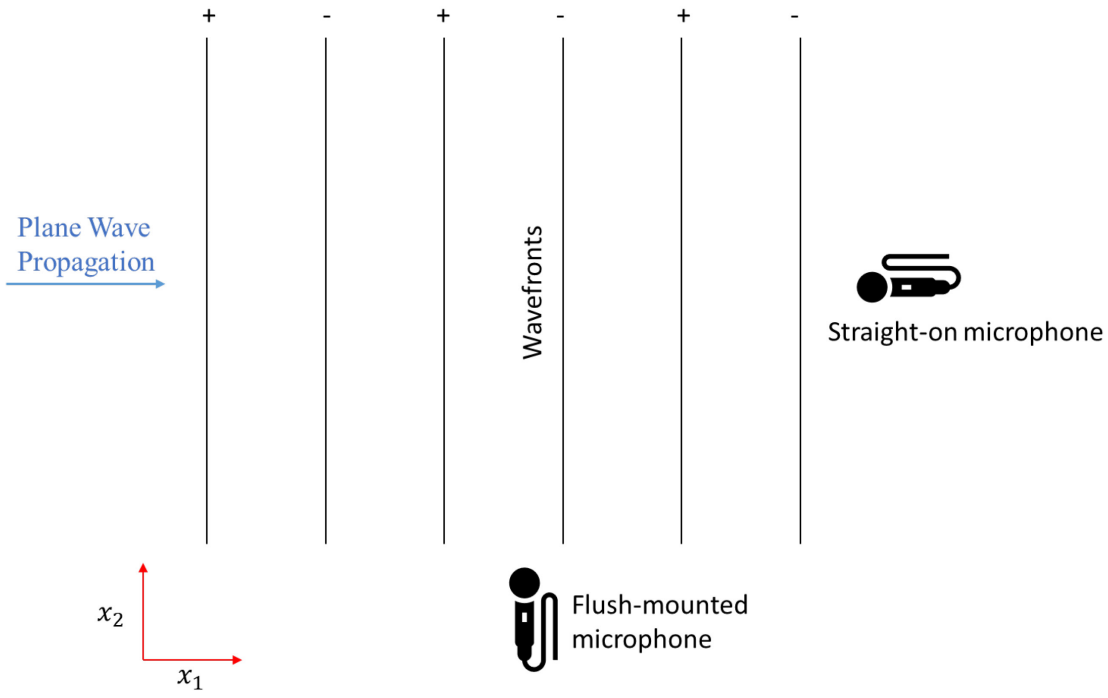

Figure 2.7, Example of flush-mounted microphone spatial alignment.

For large low-frequency waves this is not a problem, but for small high-frequency waves this orientation will cause the microphone signal to represent the spatial average of the signal distributed over its diaphragm, rather than the exact wave profile. This is illustrated in Figure 2.8, which shows a sine wave distributed in space.

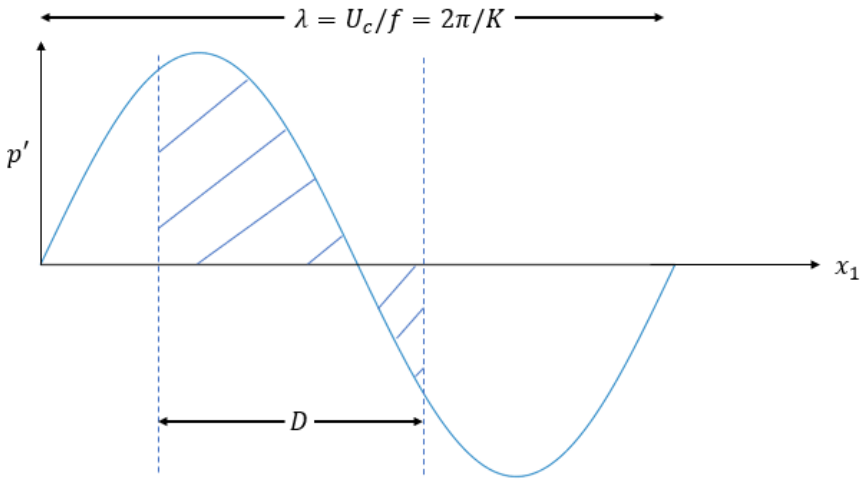

Figure 2.8, Sine wave pressure signal spatial averaging.

As the frequency of the wave increases, the transducer size $D = 2R$ begins to approach the wavelength λ; thus, the percentage of the waveform that is captured in the average reported by the microphone increases, and it becomes a less accurate representation of the actual waveform. When the transducer diameter equals the wavelength, the microphone will report no signal at all; any measurements at frequencies beyond this will be severely attenuated. This spatial response must be accounted for when studying the surface pressure data at high wavenumbers.

The wavenumber response function of a transducer is simply expressed as the Fourier transform of the spatial response function. Assuming a spatially homogeneous and temporally stationary turbulence field, the wavenumber response function is expressed by [46]:

$$H(\vec{k}) = \iint_m S(\vec{x}) e^{-i\vec{k}\cdot\vec{x}} d^2\vec{x} \tag{2.4}$$

where, as before, $\vec{k} = k_1\widehat{x_1} + k_2\widehat{x_2} + k_3\widehat{x_3}$, m indicates the microphone face, and $S(\vec{x})$ is the normalized spatial response function of the transducer face and is necessarily zero outside

of the transducer, with $\vec{x}$ measured from the center of the transducer face. The normalization of this function is such that:

$$\iint_m S(\vec{x}) d^2\vec{x} = 1 \tag{2.5}$$

The function $H(\vec{k})$ essentially represents a transfer function that relates the frequency response of the microphone to the wavenumber-frequency spectrum of the pressure field it is attempting to measure. To show this, Blake and Chase [46] write:

$$\phi_{pp,m}(\omega) = \iint_{-\infty}^{\infty} \phi_{pp}(k_1, k_3, \omega) |H(k_1, k_3)|^2 dk_1 dk_3 \tag{2.6}$$

where $\phi_{pp,m}(\omega)$ is the spatially averaged frequency response of the microphone.

Farabee and Geib [47] presented the following form of the microphone spatial sensitivity function, which is derived from the work of Blake and Chase:

$$\frac{S(r/R)}{S(0)} = \frac{J_0(\alpha) - J_0(\alpha r/R)}{J_0(\alpha) - 1} \tag{2.7}$$

where the function is assumed to be circularly symmetric and r/R is a coordinate based on the distance from the center of the diaphragm r and the total radius of the diaphragm R. J_n is a nth order Bessel function of the first kind. This function is bounded by $S(r/R) = 0$ at and beyond the diaphragm radius ($r \geq R$). The constant α was obtained by curve fitting data obtained by the manufacturer for a similar microphone diaphragm and was chosen to be 2.675 by Farabee and Geib. Performing the Fourier transform described in Equation (2.4), they obtain:

$$\left|H\left(\left|\vec{k}R\right|\right)\right|^2 = \left| \frac{2\alpha^2 \left[\left|\vec{k}R\right| J_0\left(\left|\vec{k}R\right|\right) J_1(\alpha) - \alpha J_0(\alpha) J_1\left(\left|\vec{k}R\right|\right)\right]}{\left|\vec{k}R\right| \left(\left|\vec{k}R\right|^2 - \alpha^2\right) \left[\alpha J_0(\alpha) - 2J_1(\alpha)\right]} \right|^2 \tag{2.8}$$

This equation decays quickly as $2R$ approaches λ, then quickly regains value before plummeting again as $2R$ approaches 2λ, and so forth. Using the characteristics of the flow, the wavenumber response at each flow speed can be calculated in terms of the frequency associated with each wavenumber, assuming a constant convection velocity at each flow speed.

Devenport *et al.* [48] experimentally measured the convection velocity in a wall jet boundary layer by studying the way a sinusoid pattern on the surface scattered the surface pressure spectrum. They measured values of $U_c/U_m = 0.44$ at $U_j = 40$ m/s and $U_c/U_m = 0.41$ at $U_j = 60$ m/s, which are lower than the traditionally reported value of $U_c = 0.6 - 0.8U_e$, and this was attributed to the turbulence in the mixing layer above the flow slowing down the turbulence. However, during this work, the convection velocity was measured using two-point correlation data over a separation distance of 6.15 mm, and was found to range from $0.796U_m$ to $0.896U_m$ over the velocity range of $U_j = 15$ m/s to 70 m/s. A detailed analysis is conducted in Section 3.1.3; the convection velocity values are reported in Table 2.3.

Table 2.3, Convection velocity measured using two-point correlation data.

U_j (m/s)	U_c/U_m
15	0.796
20	0.796
30	0.819
40	0.853
50	0.875
60	0.890
70	0.896

Because of this difference, computations were performed for both the Devenport *et al.* convection velocities and the measured convection velocities.

The far field 1/2" B&K microphones were aligned normal to the wave front, and thus needed no spatial resolution correction. The Knowles FG-23329 and B&K Type 4138 microphones were not aligned this way and therefore required analysis of their spatial resolution. The B&K

Type 4138 microphones were fitted with custom pinhole caps; these effectively reduce the size of the diaphragm of the microphone, allowing for much higher wavenumber resolution per transducer, as the domain of wavelengths that suffer from attenuation is much higher. In the model, the value of the function $\left|H\left(\left|\vec{k}R\right|\right)\right|^2$ stays close to 1 longer for a smaller pinhole diameter. The manufacturer pinholes on the Knowles FG-23329 have a diameter of 0.76 mm and the caps on the Type 4138 have a diameter of 0.52 mm. The resulting spatial response function can be seen in Figure 2.9.

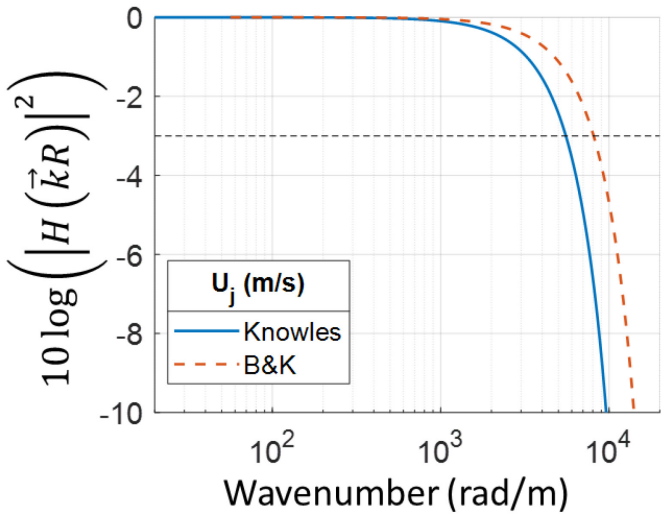

Figure 2.9, Microphone spatial response function $\left|H\left(\vec{k}R\right)\right|^2$.

Using -3 dB as a lower cutoff for the region at which the spatial averaging does not significantly affect the microphone response, the Knowles microphone data is trustworthy up to $\left|\vec{k}\right| \approx 5500$ rad/m, and the B&K microphone data is trustworthy up to $\left|\vec{k}\right| \approx 8100$ rad/m. Numerous further response lobes occur for higher wavenumbers than shown here, but these are attenuated well below -10 dB and are thus not included.

The wavenumbers in Figure 2.9 were converted to their corresponding hydrodynamic frequencies to show the spatial averaging effects in the context of our spectra, which are

plotted against frequency. These values are converted using both the measured convection velocity and that of Devenport *et al.* and are shown in Figure 2.10 as a function of frequency.

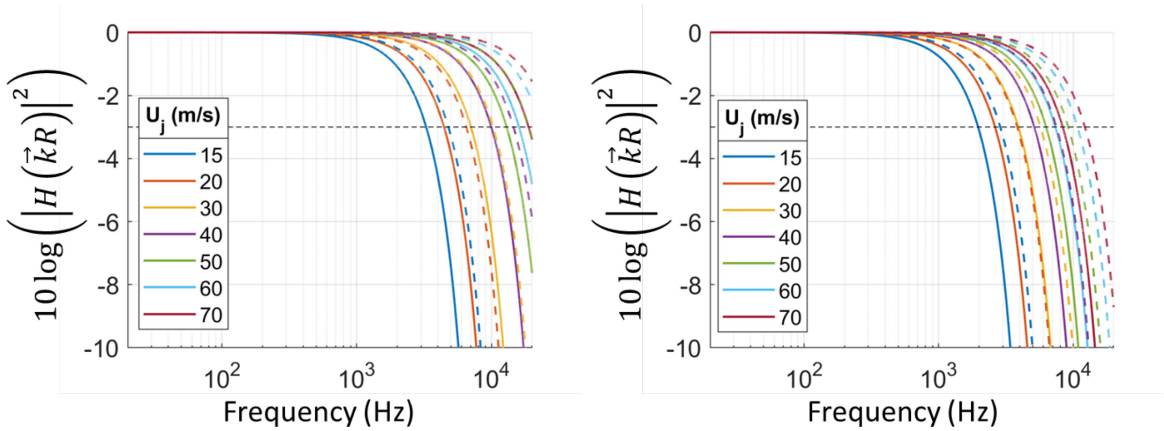

a) Measured U_c **b) Devenport *et al.* U_c**

Figure 2.10, Microphone spatial response function $\left|H\left(\vec{kR}\right)\right|^2$ as a function of frequency (dashed – B&K response, solid – Knowles response).

Figure 2.10 shows that the spatial averaging effects for the Knowles microphones at the measured convection velocities begin to exceed -3 dB at frequencies ranging from 3300 Hz at $U_j = 15$ m/s to 18.8 kHz at $U_j = 70$ m/s, and for the B&K microphones the cutoff frequencies range from 4800 Hz at $U_j = 15$ m/s to over 20 kHz at $U_j = 70$ m/s. Conversely, for the Devenport *et al.* convection velocities, these ranges are 1950 Hz to 8350 Hz and 2870 Hz to 12.2 kHz, respectively.

2.3.2 Frequency Response Calibration

Attaching pinhole caps to the microphones comes with an unfortunate side effect – this effectively turns them into Helmholtz resonators. At a certain fluctuation frequency the geometry of the cavity and pinhole causes the diaphragm and air to become a second-order resonating system, similar to that of a forced spring-mass oscillator [1]. This effect manifests in the frequency response of the pinhole microphones as a large peak at high frequencies, which must be accounted for and used to calibrate the frequency response of the microphones.

To do such a calibration requires the calculation of a transfer function. The process outlined by Joseph [49] was used: the frequency response of a microphone with a known flat response to a white noise signal emitted by a speaker is computed; then, the pinhole microphone records the same white noise signal from the same speaker, and a transfer function is calculated which relates the pinhole microphone's response to that of the flat-response microphone. This function can then be applied to future signals recorded by that pinhole microphone to correct for the Helmholtz resonance response. This is formalized in the following equation:

$$H_p(f) = \frac{G_{ps}(f)}{G_{fs}(f)} \frac{G_{ss_1}(f)}{G_{ss_2}(f)} S_f \tag{2.9}$$

In the above equation, $H_p(f)$ is the frequency response of the pinhole microphone, $G_{ps}(f)$ and $G_{fs}(f)$ are the cross spectra of the pinhole and flat response microphones with the white noise signal, respectively, $G_{ss_1}(f)$ and $G_{ss_2}(f)$ are the autospectra of the white noise signal during the flat response and pinhole microphone measurements, respectively, and S_f is the sensitivity of the flat response microphone.

The above calibration procedure was performed in two different setups: one in the anechoic chamber of the wall jet wind tunnel, and one in the anechoic chamber in Durham Hall. The two setups are shown in Figure 2.11.

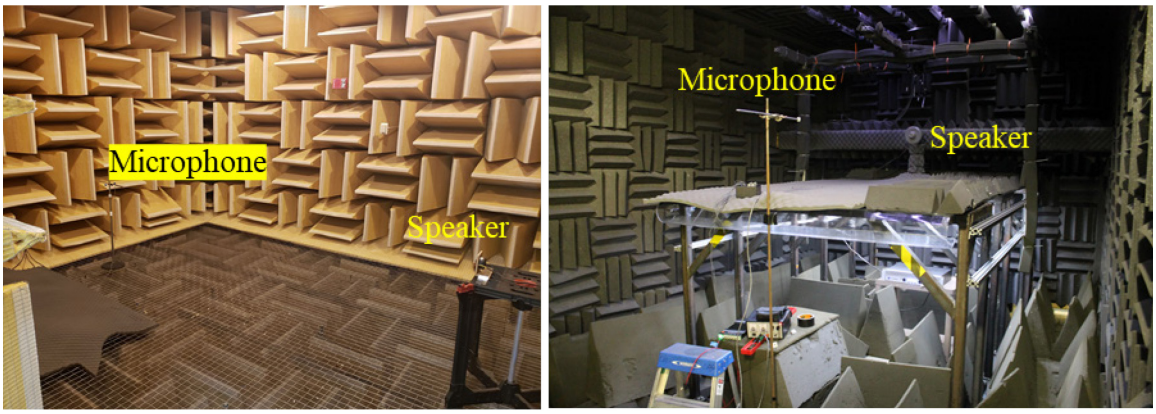

a) b)

Figure 2.11, Frequency response calibration setups.

Figure 2.11a shows the Durham Hall anechoic chamber setup, and Figure 2.11b shows the wall jet anechoic chamber setup. In both setups, an NTi Audio Minirator MR2 signal generator was used to generate a white noise signal that was collected by a DAQ and simultaneously fed into a Crown XTI 4000 power amplifier, which boosts the signal and sends it to the speaker. In setup a), the speaker is an Abaca Audio AAT414 4Ω tweeter, which is a speaker designed to have good, flat output at high frequencies; in setup b), the speaker is a University Sound ID60C8 model, another tweeter-type speaker with an impedance of 8Ω. The microphone is mounted to a horizontal rod suspended from a vertical mounting pole, and its position constant is kept constant throughout the calibration process; this ensures that each microphone measures the same signal measured by the reference microphone without any spatial effects, and that any sound reflecting off of the surfaces of the anechoic chamber is statistically repeatable. The reference microphone used was a B&K Type 4138 with a salt-and-pepper-shaker cap attached, similar to that shown in Figure 2.3. The 250 Hz sensitivity of this microphone was determined using a B&K Type 4228 pistonphone calibrator, and this sensitivity was used as the flat response sensitivity for the entire frequency range.

The amplitude calibration results for the Type 4138 with 0.5 mm pinhole cap microphones are shown below:

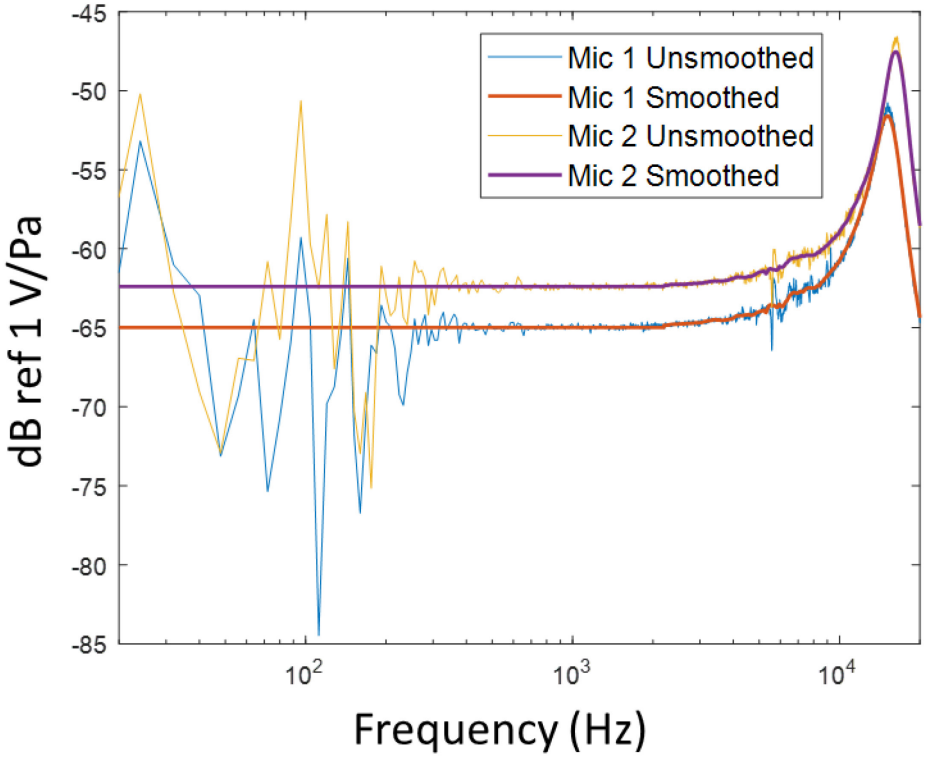

Figure 2.12, Amplitude calibration of B&K Type 4138 microphones.

The Helmholtz resonance effect and flat response can be clearly seen in Figure 2.12. For microphone 1, the peak occurs at 15.4 kHz, and for microphone 2, it occurs at 16 kHz. The noisy calibration curves have been smoothed using a piecewise method. Smoothing minimizes the large fluctuations and reduces uncertainty particularly at low frequency below the anechoic limits of the calibration facilities and at frequencies beyond the speakers' range of response. The levels below 808 Hz have been flattened to the average value in the flat region (above 256 Hz). The levels above 808 Hz are smoothed by 1/3-octave-band logarithmic binning, as this captures the overall shape of the resonant peak well while eliminating much of the noise from the measurement. The additional benefit of enforcing a flat frequency response at lower frequencies is the ability to use the pistonphone calibrator to capture the day-to-day 250 Hz sensitivity changes of the Type 4138 microphone and apply this difference to the calibration curve by a simple transfer function.

As Equation (2.9) includes cross spectra, there is a complex component to the calibration curve as well. This is the phase delay of the microphone response to a pressure signal. For a good quality microphone, this delay should be near zero at low to medium frequencies and increase at high frequencies. The difference at high frequencies can be attributed to the physical properties of the microphone, but microphone positioning error during the calibration procedure can also manifest in the phase calibration. This would appear as a linear change in the phase angle with frequency. The phase response curve for the Type 4138 microphones is shown in Figure 2.13.

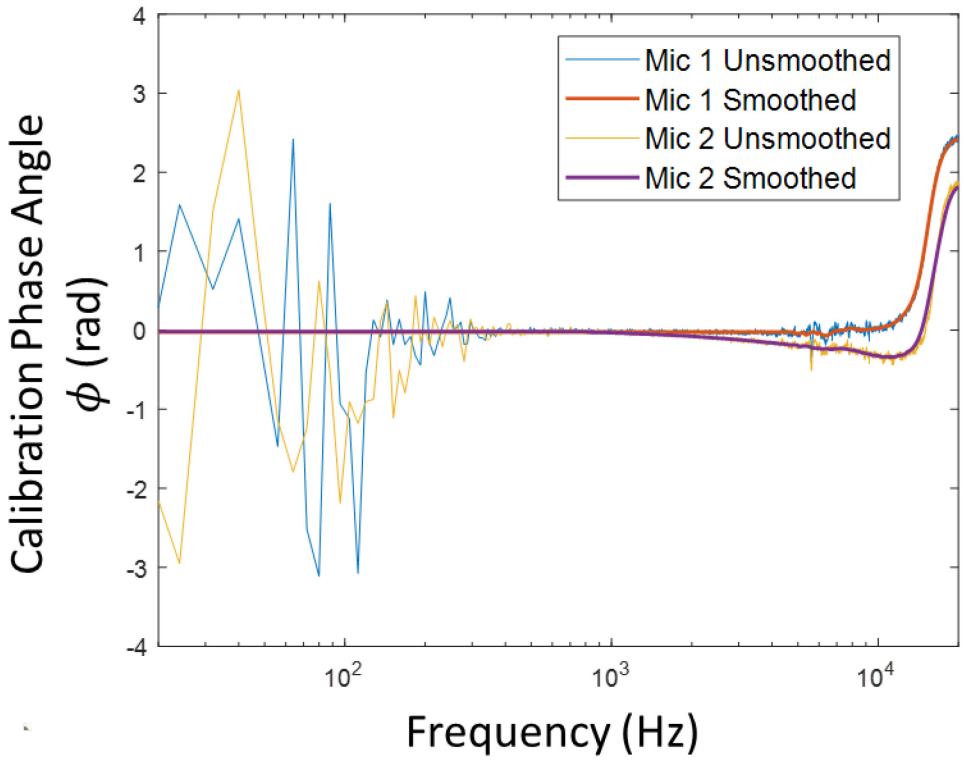

Figure 2.13, Phase response calibration of B&K Type 4138 microphones.

B&K microphones normally have a flat phase response in the audible range, but the Helmholtz resonance introduced by the pinhole caps results in a significant amount of phase delay. This phase delay must be accounted for in measurements made by these microphones,

and is done here. The slight decrease in the flat region for microphone 2 can be explained by the microphone being placed slightly farther away from the speaker than the reference microphone, causing a small time delay in the measured signal. For B&K Mic 2, which has a notable phase delay, this extra distance was calculated to be 2.2 mm using the relation $\theta = kr$, where k is the acoustic wavenumber and r is the distance between the reference microphone's position and the calibrated microphone's position. The computed displacement for B&K Mic 1 is less than 0.3 mm, and the effect on the phase angle is negligible.

The Knowles microphones were calibrated in this manner as well. While the Helmholtz resonance effect is not as strong on the Knowles microphones, as these microphones are designed with the pinhole cap, it is still necessary to have a good measure of both the actual flat response level and the range over which that flat response is valid. They were calibrated in the same facility and in the same manner as the B&K Type 4138 microphones.

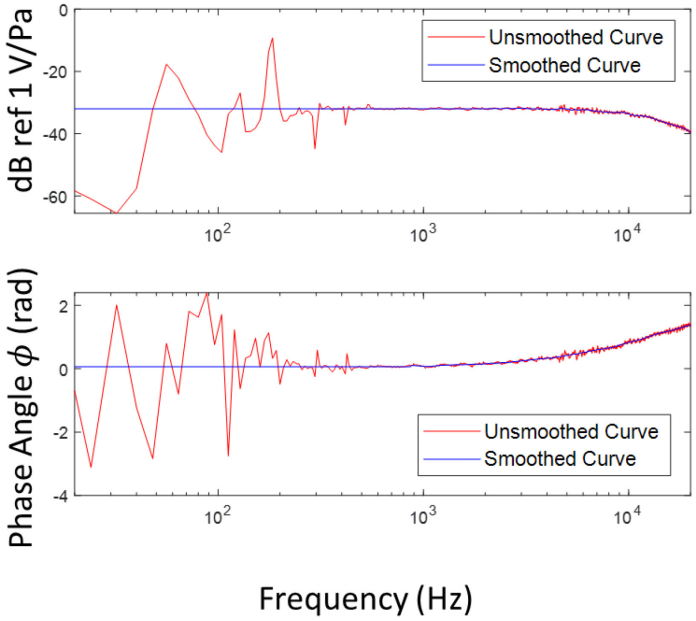

Figure 2.14, Frequency and phase response calibration curves for Knowles box 1 microphone 1.

Figure 2.14 shows an example calibration of one of the Knowles microphones. The frequency response is smoothed above 2200 Hz using 1/6 octave bands, and the phase response is smoothed above 872 Hz using 1/3 octave bands. The flat response is computed in the same away as the B&K flat response. As is to be expected, the performance of the less expensive microphones begins to drop off at lower frequencies than the B&K microphones. The sensitivity drops sharply above 10 kHz.

Figure 2.15 illustrates the spread of the sensitivity for all of the Knowles microphones used in this study. All but one of the flat region responses fall within the sensitivity range prescribed by the manufacturer (-36 to -30 dB ref 1 V/Pa).

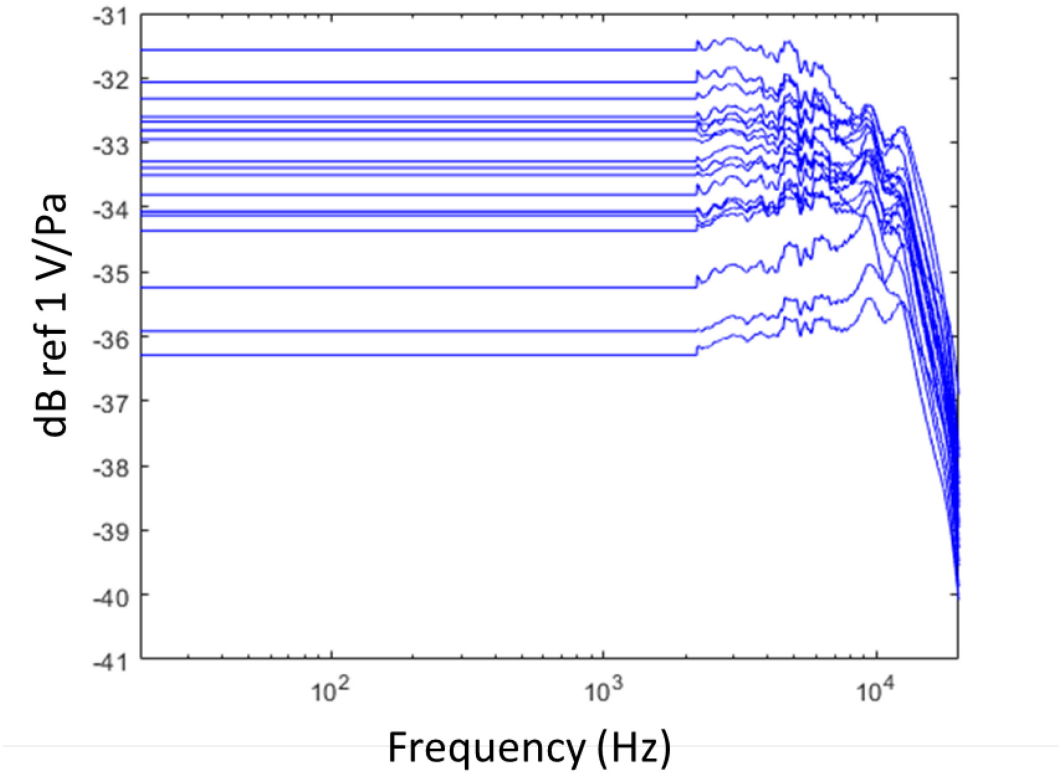

Figure 2.15, Sensitivity range of Knowles microphone frequency response.

Each of the calibrations appears to have a small hump at 12.6 kHz; this is likely the Helmholtz resonance of the microphones. Using these calibration files, the contamination this imposes on the cross-spectral and auto-spectral data can be eliminated, as illustrated in Equation (2.10).

$$\widetilde{p_{ij}^2}(\omega) = \frac{\widetilde{V_{ij}}(\omega)}{S_{ij}(\omega)} \; i,j = 1 \dots N \tag{2.10}$$

Here, $\widetilde{V_{ij}}$ and S_{ij} are the cross spectrum of the voltage measured by each microphone and the microphone calibration matrix, which comprises the combined frequency response and phase response of each microphone, and N is the number of microphones. Each component of the microphone calibration matrix is calculated by:

$$S_{ij}(\omega) = S_i S_j^*, S_i = A_i(\omega) e^{-i\phi_i(\omega)} \tag{2.11}$$

where A_i and ϕ_i are the frequency response in V/Pa^2 and phase response in rad of microphone i.

2.3.3 Microphone Dynamic Range

The B&K microphones have a manufacturer-provided dynamic range, and their performance limits were never reached during the course of the experiments. However, it became clear that it was necessary to evaluate the performance of the inexpensive Knowles microphones to determine if they were adequate for our purposes. Every microphone has a threshold above which it can no longer effectively record noise. This can be provided as the dynamic range of a microphone or the acoustic overload point. In the measured surface pressure spectra this tends to show up as a flattening of the low-frequency content of the signal, where the highest portion of the energy content resides.

To conclusively determine the range of jet speeds and frequencies over which the Knowles microphones could provide an adequate result, a Knowles microphone and two B&K Type 4138 microphones were recorded at the same streamwise position, in the region in which the

flow is expected to be relatively uniform across the span [37]. The Knowles data was evaluated in comparison to the B&K data to determine the performance of the microphone. The recording setup as constructed in the wall jet is shown in Figure 2.16, with B&K microphones 1 and 2 mounted flush in the two holes to the left of the Knowles microphone in Figure 2.16.

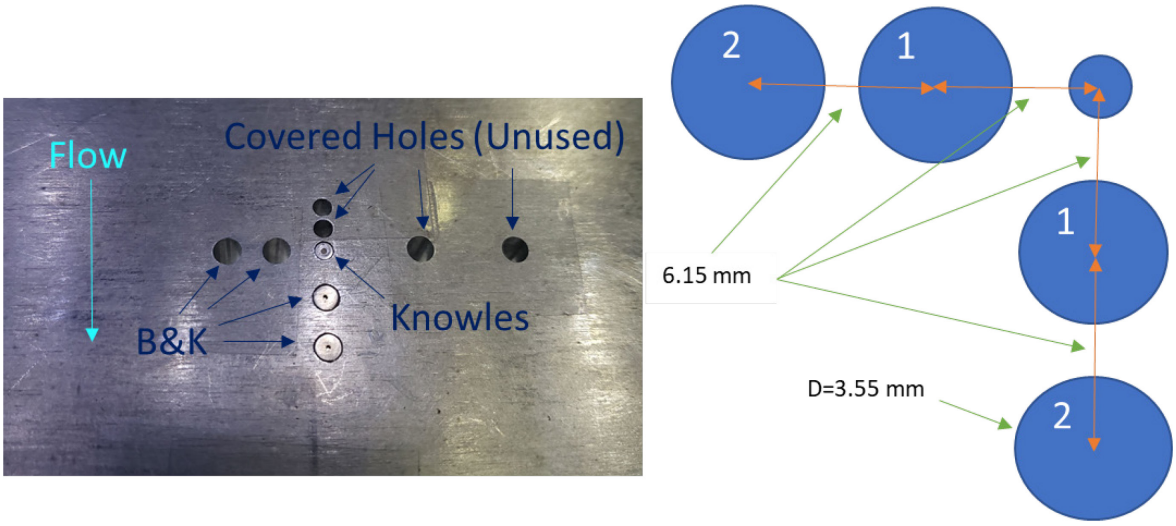

Figure 2.16, Layout of Knowles performance validation experiment.

Measurements were taken at nozzle exit velocities of 15 m/s and 20 m/s to 70 m/s in 10 m/s increments. The results for each microphone are shown in Figure 2.17. The autospectra for each microphone are presented as well as the both the coherence between B&K microphone 1 and microphone 2 and the coherence between B&K microphone 1 and the Knowles microphone at each tunnel velocity.

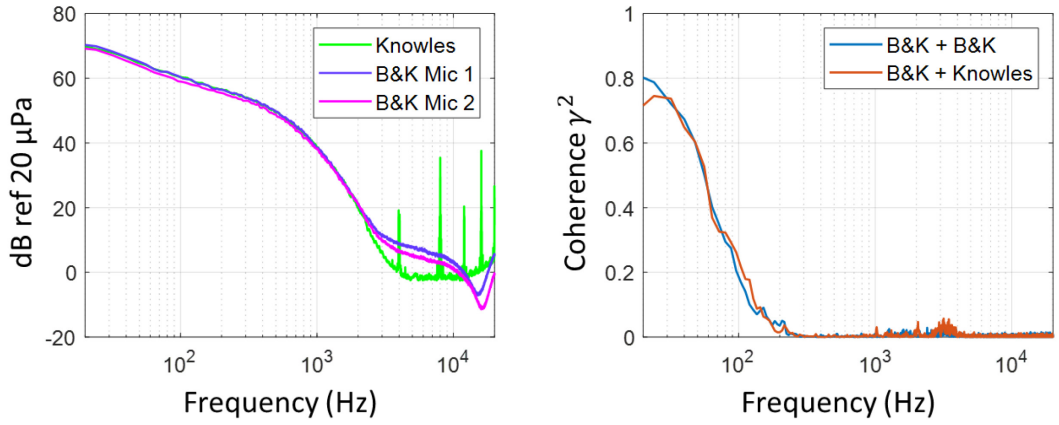

a) U_j = 15 m/s

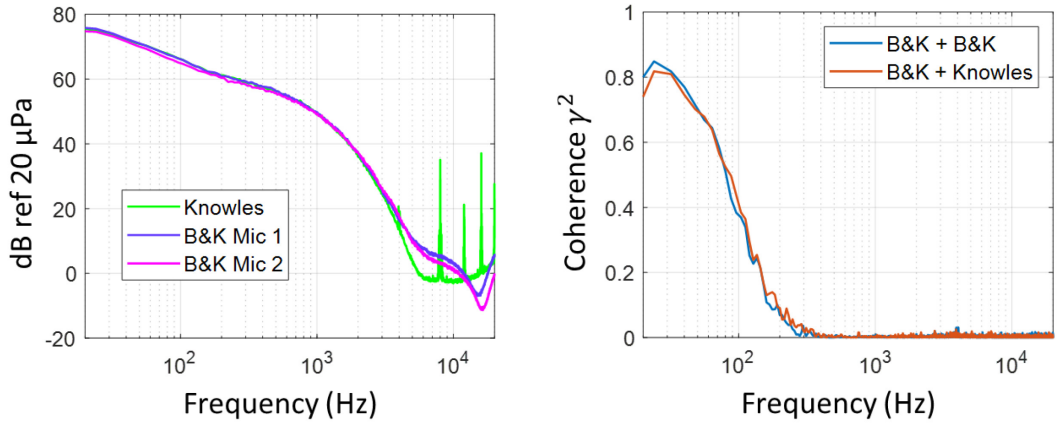

b) **U_j = 20 m/s**

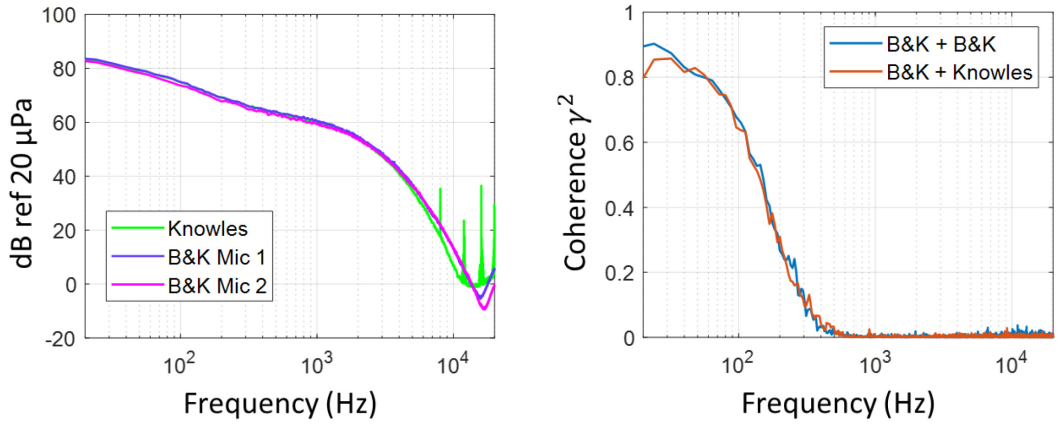

c) U_j = 30 m/s

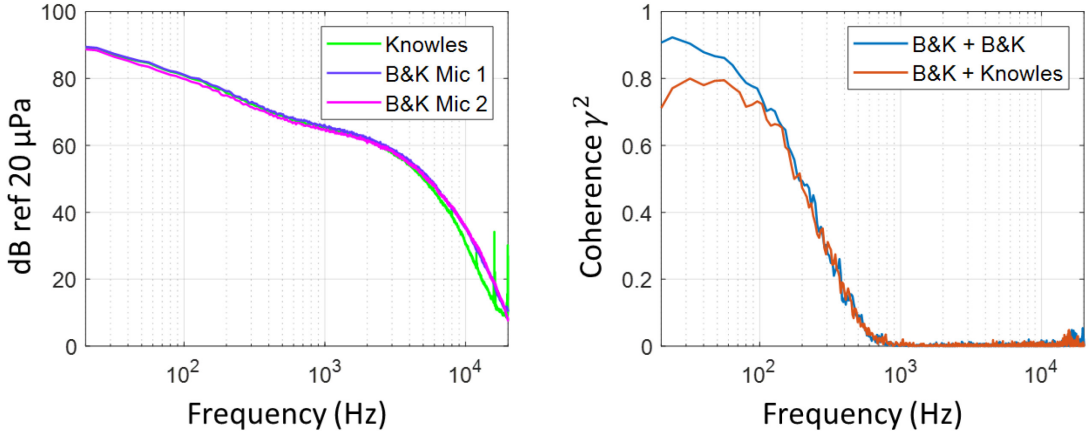

d) $U_j = 40$ m/s

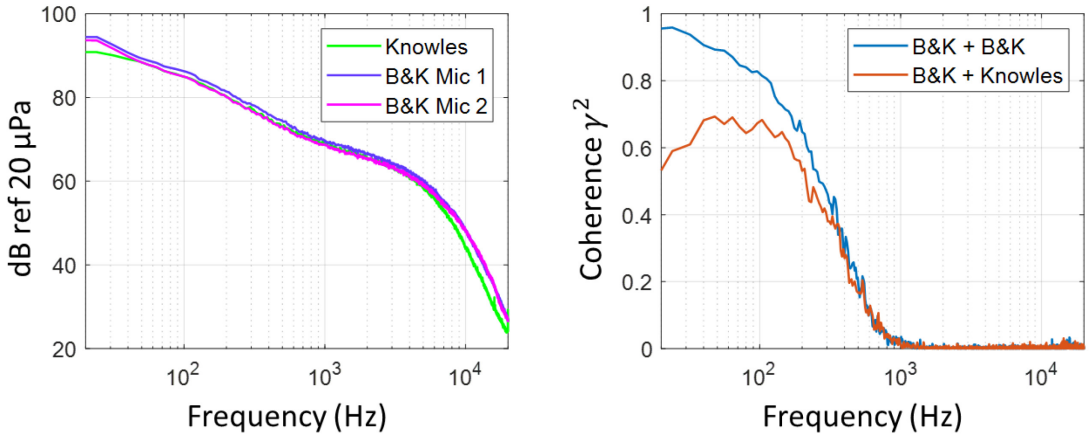

e) $U_j = 50$ m/s

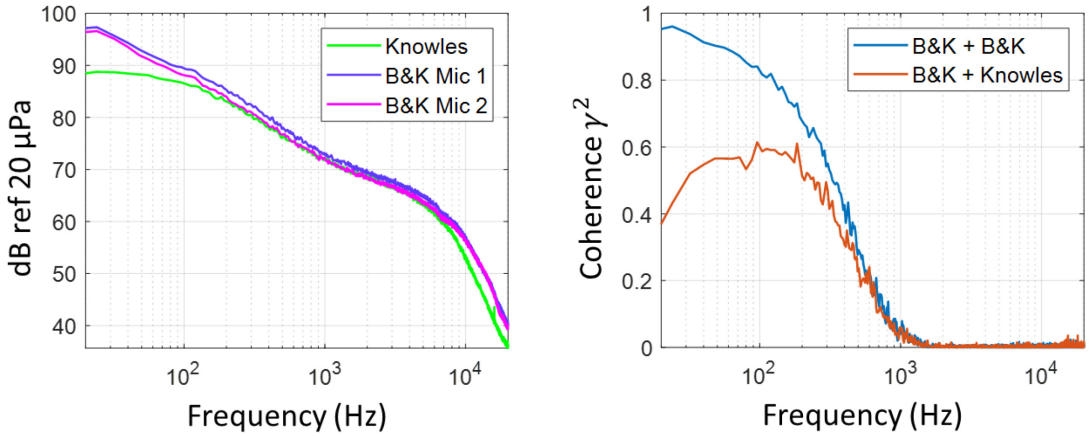

f) $U_j = 60$ m/s

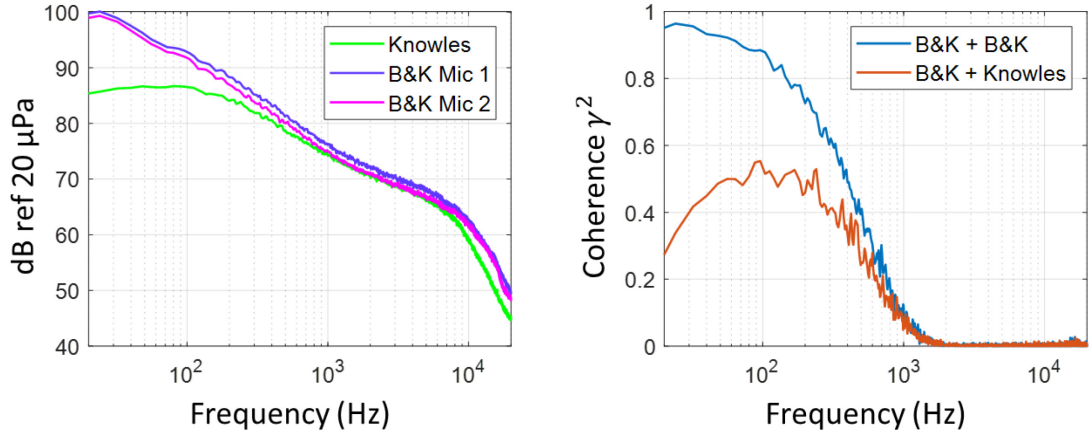

g) U_j = 70 m/s

Figure 2.17, Comparison of flat-plate Knowles and B&K Type 4138 autospectra (left) and spanwise coherence between equally-spaced pairs of microphones (right).

Figure 2.17 shows good agreement between the Knowles and B&K microphones for most of the velocity and frequency range of interest. Data are only displayed in the acoustic range (20-20000 Hz). From a), b), and c), the Knowles microphones appear to have a noise floor of 0 dB. The erroneous dip in the B&K spectra at the pinhole frequency is due to the noise floor of the microphone being reached before the pinhole frequency; thus, the frequency response designed to eliminate the pinhole response is applied incorrectly. To determine the B&K noise floor, the B&K data were calibrated by applying the flat-response level through the entire frequency range. This is shown in Figure 2.18.

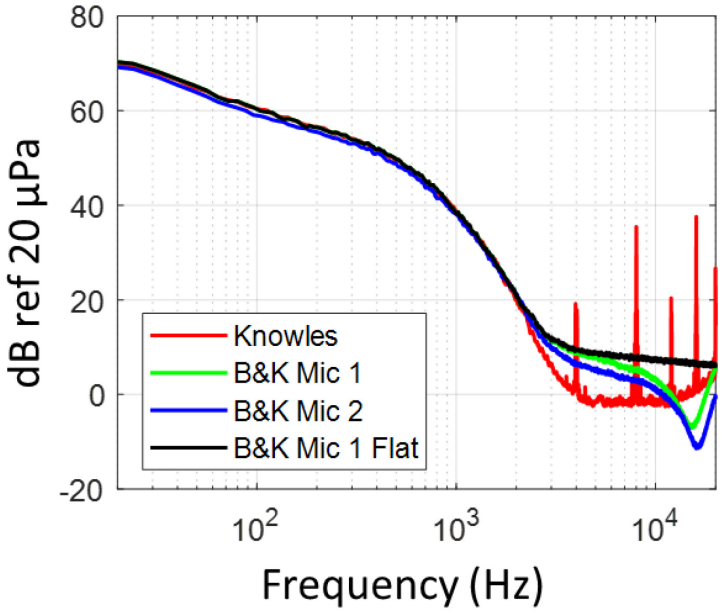

Figure 2.18, Comparison of B&K pinhole response and flat response at low speed. $U_j = 15$ m/s.

From Figure 2.18, the noise floor of the B&K microphones is estimated to be 10 dB. The upper cutoff frequency for the Knowles and B&K microphones can be estimated by determining when the spectrum begins to deviate from the linear roll-off at higher frequencies.

There is also low-frequency attenuation at higher speeds, which indicates that the upper limit of the Knowles' dynamic range is being reached. Integrating the spectra between 16 and 20000 Hz (or the noise floor) gives the overall sound pressure level for the given spectrum. The OASPL at each speed in Figure 2.17 is shown in Figure 2.19 as the relationship between the OASPL and the local maximum velocity corresponding with each jet speed. A straight line indicating the expected relationship of $S_{pp} \sim U_m^4$, which extrapolates the $q \sim U^2$ relationship of dynamic pressure, is also plotted in this figure, as well as a line showing the relationship $S_{pp} \sim U_m^{4.4}$, which better fits the data.

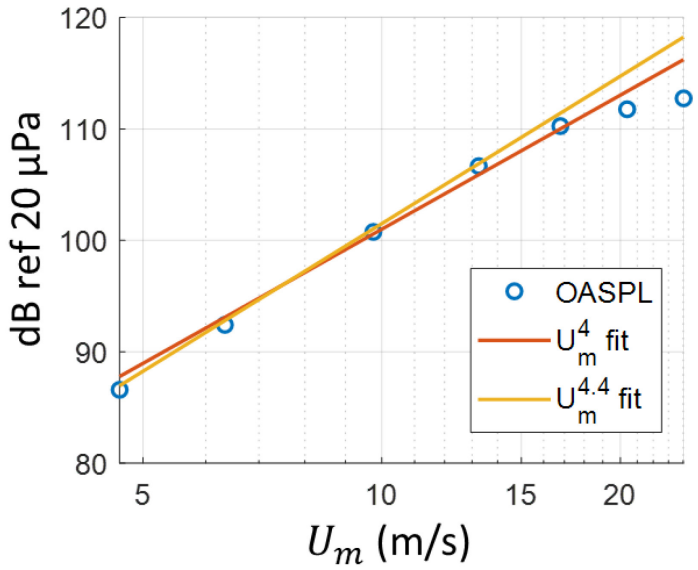

Figure 2.19, OASPL of Knowles microphone spectrum vs. nozzle velocity.

Figure 2.19 shows that the OASPL of the Knowles microphone measurements begins to asymptote to a value of around $SPL \approx 115$ dB. This is the maximum sound pressure level that the microphone is capable of measuring, and as shown in Figure 2.19, this limit begins to affect the spectrum at speeds of $U_j \geq 50$ m/s, where the OASPL measurements begin to diverge from the $U_m^{4.4}$ fit. As shown in Figure 2.17, this effect is primarily at the lowest frequencies in both the autospectrum and coherence, and the lower cutoff for this frequency increases with increasing edge velocity.

Additionally, at all speeds, the spatial attenuation of the Knowles microphones above a particular frequency becomes apparent, as predicted by Figure 2.9. This cutoff frequency increases with flow speed because as the speed increases, the wavenumber at a particular frequency decreases. In other words, eddies of a particular size convect faster, and thus their frequencies increase. This region is not apparent at nozzle velocities of 20 m/s and below, and for $U_j = 30$, 40, 50, 60, and 70 m/s, the Knowles autospectrum diverges from the B&K autospectrum by >3 dB on average above approximately $f = 6800$ Hz, 8300 Hz, 8960 Hz, 9550 Hz, and 10200 Hz, respectively. These cutoff frequencies are higher than those

predicted by using the Devenport *et al.* convection velocity in Section 2.3.1, but lower than those predicted by the measured two-point correlation convection velocity. Unlike the noise floor cutoff and clipped data cutoff, the spatial attenuation region can still be useful for analysis, as the decrease in measured value can be estimated, and thus data beyond these frequencies will not be entirely ignored in the analysis. From Figure 2.17, at $U_j = 30$ m/s, the attenuation due to spatial averaging slowly increases up to about 5 dB before the cutoff, and at $U_j = 40$ m/s, up to 6 dB. At $U_j = 50$ m/s, the attenuation increases up to 5 dB by 14 kHz, at which point it remains constantly 5 dB until the acoustic region maximum. The same is true at $U_j = 60$ m/s. At $U_j = 70$ m/s, the same is true, but the data for B&K mic 2 are about 2 dB lower than mic 1. The Knowles data is still 5 dB lower than mic 1 in this region.

Table 2.4 compiles the estimated valid frequency ranges for the Knowles and B&K microphones across the full domain of test conditions.

Table 2.4, Valid frequency range for surface pressure microphone autospectra and spanwise coherence measurements.

	Autospectra		**Spanwise Coherence**
U_j (m/s)	**Knowles**	**1/8" B&K**	**Knowles**
15	$f \leq 3000$ Hz	$f \leq 2500$ Hz	$f \geq 24$ Hz
20	$f \leq 5500$ Hz	$f \leq 5000$ Hz	$f \geq 24$ Hz
30	$f \leq 10500$ Hz	$f \leq 11000$ Hz	$f \geq 32$ Hz
40	$f \leq 16500$ Hz	N/A	$f \geq 96$ Hz
50	$f \geq 40$ Hz	N/A	$f \geq 352$ Hz
60	$f \geq 176$ Hz	N/A	$f \geq 560$ Hz
70	$f \geq 800$ Hz	N/A	$f \geq 800$ Hz

The acoustic limits, 20-20000 Hz, are implied. The Knowles lower frequency limit was defined as the point where the measured autospectrum deviates by >1 dB from the B&K-measured autospectrum. The upper frequency limit for both microphones is defined as the inflection point where the slope of the autospectrum departs from the high frequency linear slope region. The spanwise coherence lower limit is defined as the point where the spanwise coherence between the B&K and Knowles microphones deviates from the coherence

between the B&K and B&K microphones by 0.05 or more. The autospectral frequency ranges are hard cutoffs, outside of which data cannot be trusted. The spanwise coherence cutoff may still show useful trends below the cutoff line, although the data should be interpreted with greater scrutiny.

2.4 Straight Trailing Edge

The straight trailing edge used in this work was originally used by Millican [50,51] in experiments at Virginia Tech regarding trailing edge noise reduction via fence and rail finlets, like the work of Clark *et al.* [26,27]. Called a "mock" trailing edge due to the one-sided flow design, it was designed to sit on top of the solid plate of the wall jet test section, so flow only passes over the top of the piece. This edge was manufactured as two pieces due to machine limitations and is milled from solid aluminum. The total span of the two pieces is 971.55 mm, and the height of each piece is 12.7 mm. The trailing edge itself has a thickness of 0.794 mm. To ensure smooth flow transition from the wall jet plate to the top of the trailing edge piece, an aluminum ramp with a gradual curve is placed upstream of the edge. The upstream portion of this ramp is sealed to the wall jet plate using aluminum foil tape to ensure a smooth transition from the wall jet plate to the ramp and beyond. Millican showed that in the previous wall jet facility, this ramp had minimal effect on the flow speed, increasing U_m by up to 1% [50]. For additional smooth transition, edge-rounding pieces were 3D printed that smooth the 12.7 mm spanwise edges of the trailing edge as they transition down onto the plate, similar to the upstream ramp. The sharp 12.7 mm edge of the ramp that extends well beyond the trailing edge is smoothed by a rounded piece of aluminum that minimizes the amount of noise scattered by this edge.

Figure 2.20 shows the full setup described above as mounted in the wall jet tunnel. Figure 2.21 shows the geometry of the "mock" trailing edge as it sits mounted on the plate.

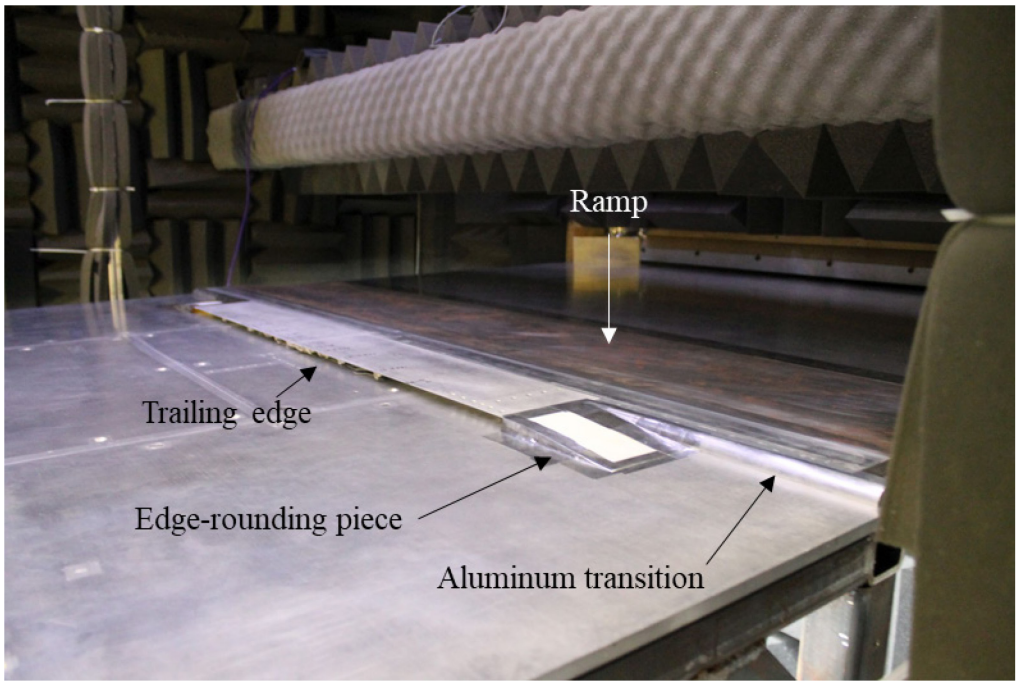

Figure 2.20, Straight trailing edge setup in wall jet tunnel.

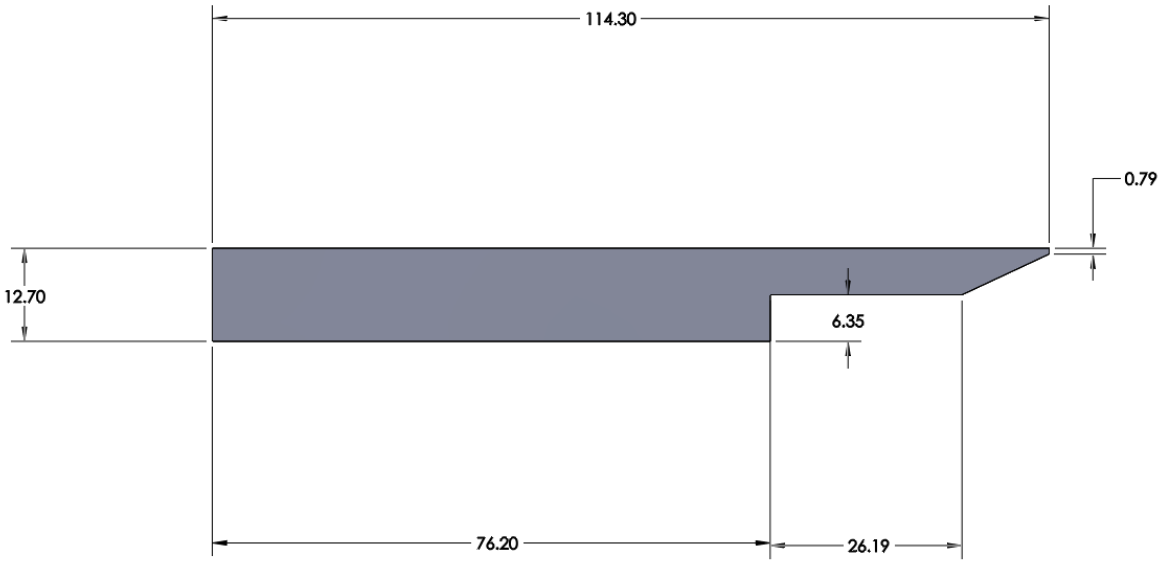

Figure 2.21, Geometry of "mock" trailing edge (dimensions in mm).

Above the straight trailing edge are the far field microphones, arranged in the following locations, as shown in Figure 2.22.

Table 2.5, Far field microphone positions for straight trailing edge experiments.

Mic	x_1 (m)	x_2 (m)	x_3 (m)	$\lvert\vec{x}\rvert$ (m)	θ (°)
1	-0.3493	0.6239	-0.00476	0.715006	119.23
2	-0.2397	0.6683	-0.00476	0.710042	109.73
3	-0.1524	0.6888	-0.00318	0.705636	102.48
4	-0.00635	0.7080	-0.0127	0.708167	90.514

The dimensions in Table 2.5 are referenced to the coordinate system described in Figure 1.1 and Figure 1.2. Mounting the microphones in an arc like this is unlikely to allow for a good study of trailing edge noise directivity, as the expected change in trailing edge noise levels is +1.69 dB between Mic 4 and Mic 1, according to Equation (1.12). However, the arc can still be used to find a location with a good signal-to-noise ratio. The upstream microphones are expected to have much better signal-to-noise ratios than the downstream microphones because of the horizontal and vertical baffle shielding. The far field microphones are shown mounted in Figure 2.22 to illustrate their location relative to the trailing edge.

The Knowles microphones are mounted flush with the surface of the trailing edge 3 mm from the edge itself. It is desirable to mount the microphones as close to the trailing edge as possible, as this increases the validity of the statistically frozen field assumption. Figure 2.23 shows some of the microphones mounted within the straight trailing edge to illustrate this.

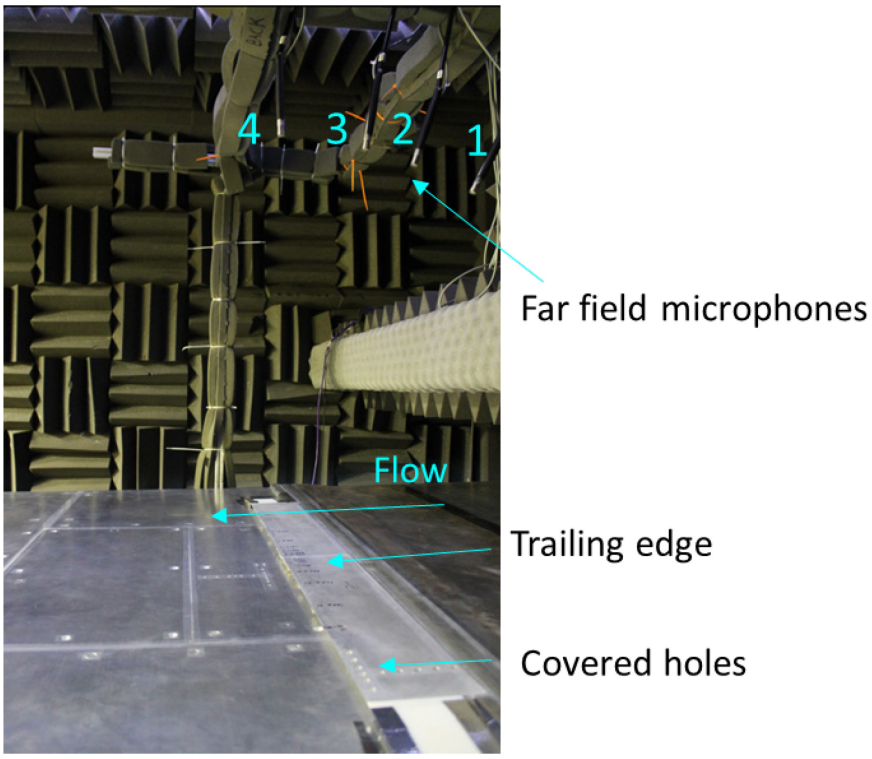

Figure 2.22, Far field microphone arc in straight trailing edge configuration.

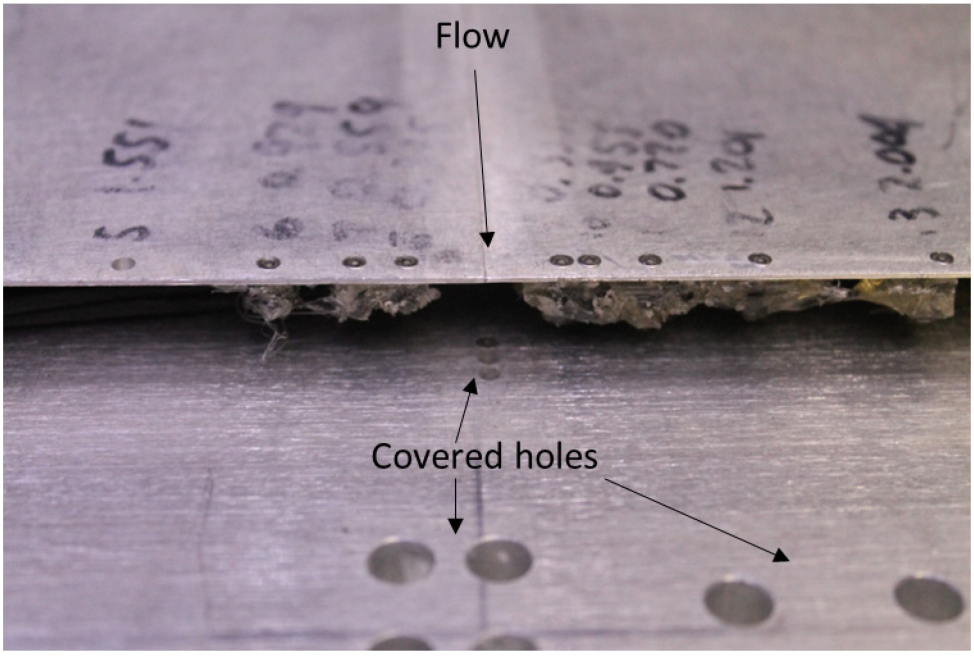

Figure 2.23, Knowles microphones mounted flush with mock trailing edge surface.

Beneath the trailing edge, hot glue was used to both hold the microphones in place and to ensure that no air could flow around the microphones to the underside of the edge, which would affect the lift response function. The hot glue shown in Figure 2.23 is fully recessed under the edge and is not visible from the top side. The microphones are distributed irregularly along the x_3 axis; this is by design, to form a wavenumber filter that rejects high-order spanwise wavenumbers. In addition, slots are cut in the top of the wall jet plate to allow the microphone wires to feed through to the power supply and DAQs beneath. This slot was sealed from the underside with aluminum foil tape to prevent flow between the top and bottom of the wall jet plate.

Table 2.6 shows the microphone locations on the straight trailing edge that form the wavenumber filter. Each microphone is located at $x_1 =$ -3 mm.

Table 2.6, Surface pressure microphone spanwise distribution for straight trailing edge.

Mic	x_3 (mm)	Mic	x_3 (mm)	Mic	x_3 (mm)	Mic	x_3 (mm)
1	304.8	5	39.40	9	-8.509	13	-50.90
2	182.8	6	23.60	10	-11.56	14	-84.91
3	109.6	7	14.20	11	-18.29	15	-141.5
4	65.71	8	8.509	12	-30.50	16	-236.0

This spacing is visualized in Figure 2.24.

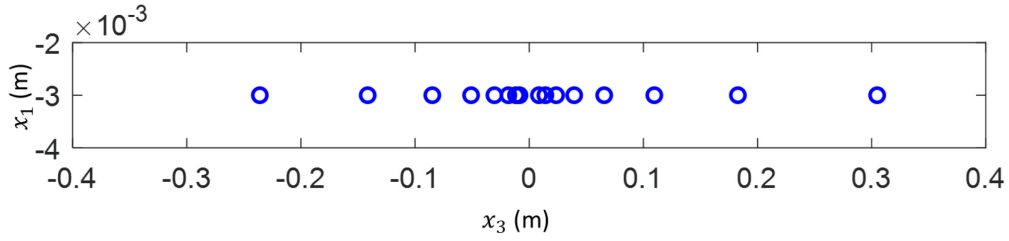

Figure 2.24, Surface pressure microphone spanwise distribution for straight trailing edge.

This uneven spacing is determined logarithmically and will be discussed in Section 2.7.

In Figure 2.22 and Figure 2.23, holes can be seen in the surface of the wall jet test plate. These holes were drilled in a previous experiment, and in this experiment are covered with clear tape that has a thickness of 40 μm, hereafter referred to as micron tape. This tape is used to smooth out any discontinuities as much as possible and is used over every bolt hole and seam in the setup, including the joint between the two halves of the trailing edge. A surface with nondimensional roughness of height $y_+ = yu_\tau/\nu < 5$ can be considered to be hydrodynamically smooth [52]; as $y_+ \sim u_\tau$, the largest value will occur at the highest speed; for $U_j = 70$ m/s, the value of y_+ for micron tape at the trailing edge is 3.0, indicating that the micron tape is hydrodynamically smooth at all tunnel speeds.

To verify the result of Millican [50], a study of the surface pressure field on the flat plate compared to the surface pressure field on the mock trailing edge was done using the setup in Figure 2.16. First, two Knowles microphones were placed in the two holes upstream of the central Knowles microphone; the distance between these holes is 3 mm. Surface pressure data from the experiment in Section 2.3.3 were compared to these data and surface pressure data taken from the configuration in Figure 2.20. The surface pressure fields at $U_j = 20$ m/s, 40 m/s, and 60 m/s are shown in Figure 2.25.

Figure 2.25 shows that at each speed, there is a region where the trailing edge surface pressure autospectrum is increased by about 2 dB. For $U_j = 20$ m/s, this region begins at 120 Hz and continues through the rest of the frequency range; for $U_j = 40$ m/s, this region is approximately 250 to 3000 Hz; and for $U_j = 60$ m/s, this region is from approximately 400 Hz to 8000 Hz. The increase in pressure can likely be attributed to the maximum speed increase reported by Devenport *et al.* [48] and Millican [50], though it is of somewhat greater magnitude, as the measured discrepancy is outside of the uncertainty of the individual microphones, though not outside of the range of surface pressure uniformity. Both of these results are shown in Section 2.8.

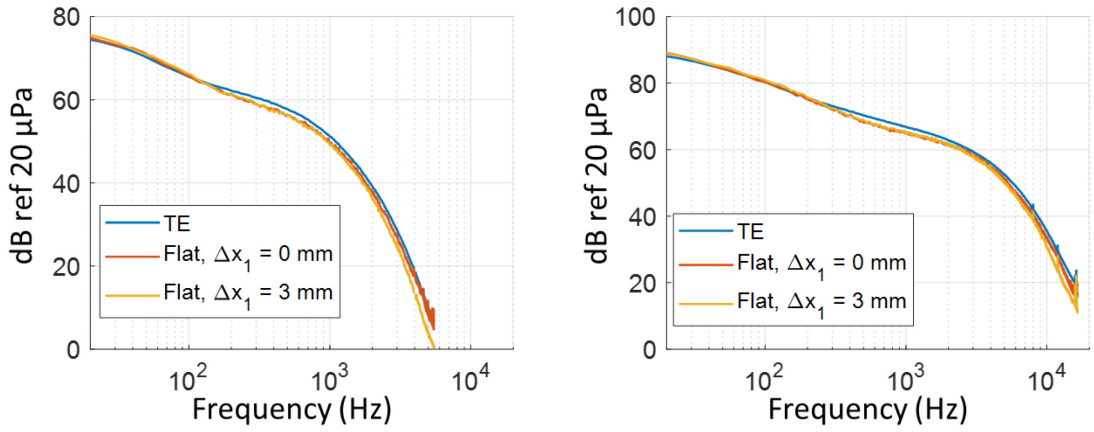

a) $U_j = 20$ m/s **b) $U_j = 40$ m/s**

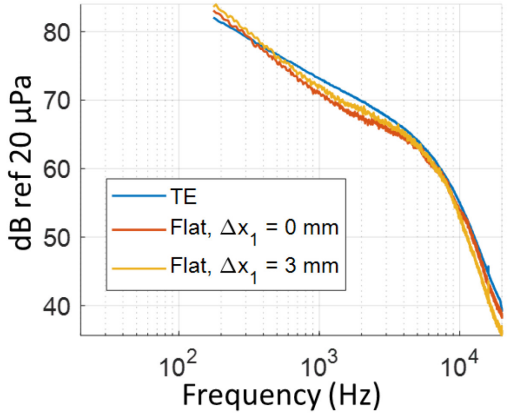

c) $U_j = 60$ m/s

Figure 2.25, Comparison between flat plate surface pressure and trailing edge surface pressure autospectra.

2.5 Serrated Trailing Edge

The serrated trailing edge was designed to resemble the mock trailing edge as closely as possible. It was designed with the same height, 12.7 mm, and to be used with the same ramp and rounded aluminum. The serrations had a sawtooth shape with a wavelength λ of 1.5 cm and an amplitude $2h$ of 1.5 cm, as shown in Figure 2.27, which comprise the entire trailing edge span. The serrated trailing edge was manufactured by Proto Labs, Inc., and the printed microphone holes were further drilled out by the Virginia Tech AOE machine shop. It was

again manufactured in two pieces, each with a span of 457.2 mm. The length was chosen such that the centers of the serrations were located in the same x_1 position as the previous straight trailing edge. New edge-rounding pieces were printed to fit the new trailing edge dimensions. The full geometry of the serrated trailing edge can be seen in Figure 2.26 and Figure 2.27.

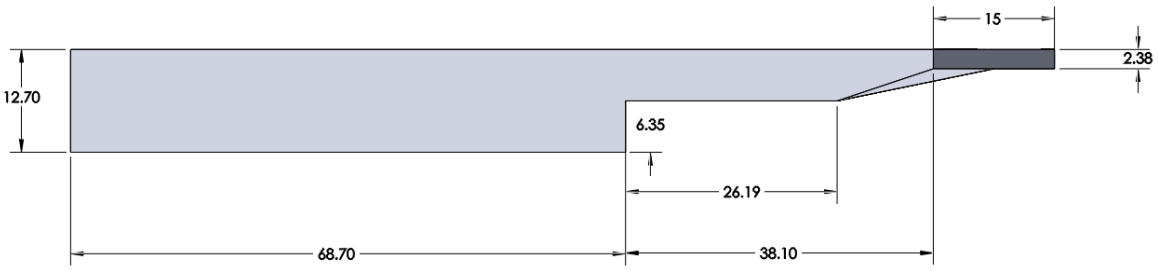

Figure 2.26, Side view of serrated trailing edge (dimensions in mm).

One key difference between the serrated edge and the straight edge is the thickness of the serrations, which had to be made 2.38 mm thick in order to remain structurally sound. This is a notable deviation from theory [30,31], which assumes an infinitesimal edge thickness.

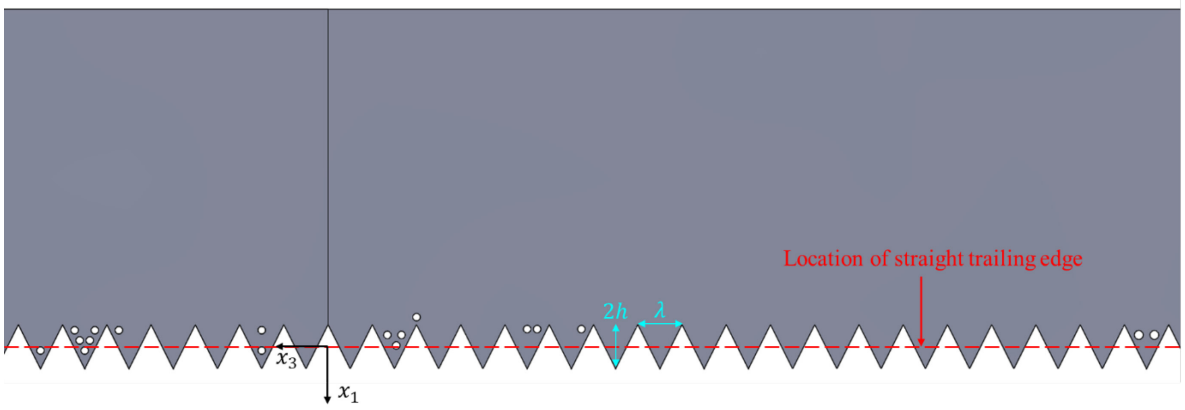

Figure 2.27, Top view of serrated trailing edge. $\lambda = 1.5$ cm, $2h = 1.5$ cm.

In Figure 2.27, a top view of the serrated trailing edge is shown. Each trailing edge piece has 30 serrations, for a total of 60 serrated teeth across the whole span. Additionally, as shown in Figure 2.26, reinforcing ribs were added beneath each serration to prevent them from

flexing and/or breaking during installation and experiments. These ribs extend out to the midpoint of each serration and have a thickness of 0.794 mm. The microphone holes are numbered 1-18 from left to right as shown in Figure 2.27.

In Figure 2.28, the locations of the working microphones are shown and labeled. As before, they are flush with the top surface and sealed underneath with hot glue. The microphone locations were chosen to study the surface pressure field in as many different locations on each serration as possible, and singular microphones were placed on separate serrations to measure coherence and to compare the result from each tooth, to see if the measurements at each tooth in the same location are consistent. A local coordinate system defined for each serration is shown in Figure 2.28 to match the locations of similarly placed microphones on different serrations.

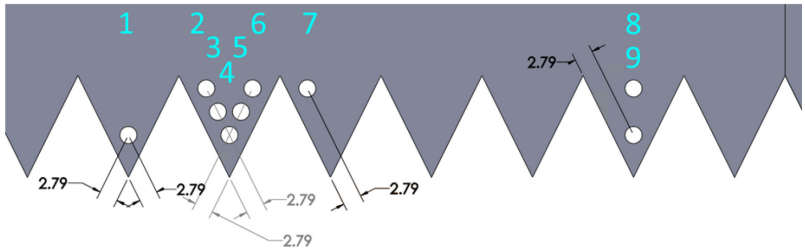

a)

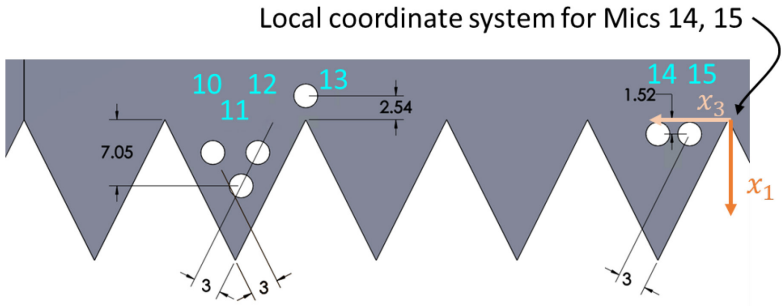

b)

Figure 2.28, Close up view of microphone locations on serrated trailing edge (dimensions in mm).

The remaining three microphones on the right side of Figure 2.27 were not used. Microphone 16 was found to not work after installing the system, and Microphones 17 and 18 were installed but not used, due to a manufacturing defect in the serration that prevented the microphones from sitting flush with the top surface. Data were taken from these microphones uncovered, covered, and covered with micron tape with a hole punched to expose the diaphragm of the microphone while sealing the mounting hole. Despite our efforts, the data from these two microphones were significantly contaminated by the effects of not being flush to be useful for the study. Thus, a total of fifteen microphones were available for data collection.

Table 2.7 reports the locations of the surface pressure microphones in both local and global coordinates. These local coordinates are defined from the nearest root in the $-x_3$ direction as shown in Figure 2.28 and are used to cross-reference microphone positions for comparison.

Table 2.7, Actual surface pressure microphone positions for serrated trailing edge.

Mic	x_1 (mm), local	x_3 (mm), local	x_1 (mm), global	x_3 (mm), global
1	8.76	7.46	1.26	97.45
2	1.85	10.88	-5.66	85.88
3	5.30	9.12	-2.20	84.12
4	8.81	7.40	1.31	82.40
5	5.29	5.70	-2.21	80.70
6	1.80	4.05	-5.70	79.05
7	1.78	10.89	-5.72	70.89
8	1.75	7.42	-5.75	22.42
9	8.75	7.32	1.25	22.32
10	3.39	9.85	-4.11	-20.15
11	6.97	6.91	-0.53	-23.10
12	3.37	5.07	-4.13	-24.93
13	-2.69	0.00	-10.19	-29.99
14	1.49	7.56	-6.01	-67.44
15	1.51	4.14	-5.99	-70.86

Note that Table 2.7 lists the actual positions of the microphones, while Figure 2.28 shows the prescribed positions of the microphones. The drilling out performed by the machine shop

necessitated an examination of the actual locations of the microphones, and the locations were determined using overhead photo measurements performed in MATLAB. The manufacturing error is tabulated in Table 2.8.

Table 2.8, Prescribed surface pressure microphone positions and placement error.

Mic	Prescribed x_1 (mm), global	Prescribed x_3 (mm), global	$\lvert\Delta x_1\rvert$ (mm)	$\lvert\Delta x_3\rvert$ (mm)
1	1.27	97.5	0.01	0.05
2	-5.60	85.93	0.1	0.05
3	-2.16	84.22	0.04	0.1
4	1.27	82.5	0.04	0.1
5	-2.16	80.78	0.05	0.08
6	-5.60	79.07	0.1	0.02
7	-5.60	70.93	0.12	0.04
8	-5.60	22.5	0.15	0.08
9	1.27	22.5	0.02	0.18
10	-4.00	-20.10	0.11	0.05
11	-0.45	-23.12	0.08	0.02
12	-4.00	-24.90	0.13	0.03
13	-10.04	-30	0.15	0.01
14	-5.98	-67.5	0.03	0.06
15	-5.98	-70.88	0.01	0.02

Table 2.8 shows that that maximum absolute placement error is on the order of 0.15 mm. This length is 1% of λ and h, indicating that the microphones are placed with a good degree of accuracy. Additionally, some measurement error could come from the extremely small scale being measured on and the pixel resolution of the photos examined in MATLAB. This error is estimated to be ± 0.02 mm.

Figure 2.29 shows the serrated trailing edge mounted in the tunnel with the far field microphones situated above it, and Figure 2.30 shows the Knowles microphones mounted in the serrated edge. The far field microphones are in very slightly different positions from their positions in the straight trailing edge runs, due to them being moved between the straight trailing edge runs and the serrated edge runs. The new locations are tabulated in Table 2.9.

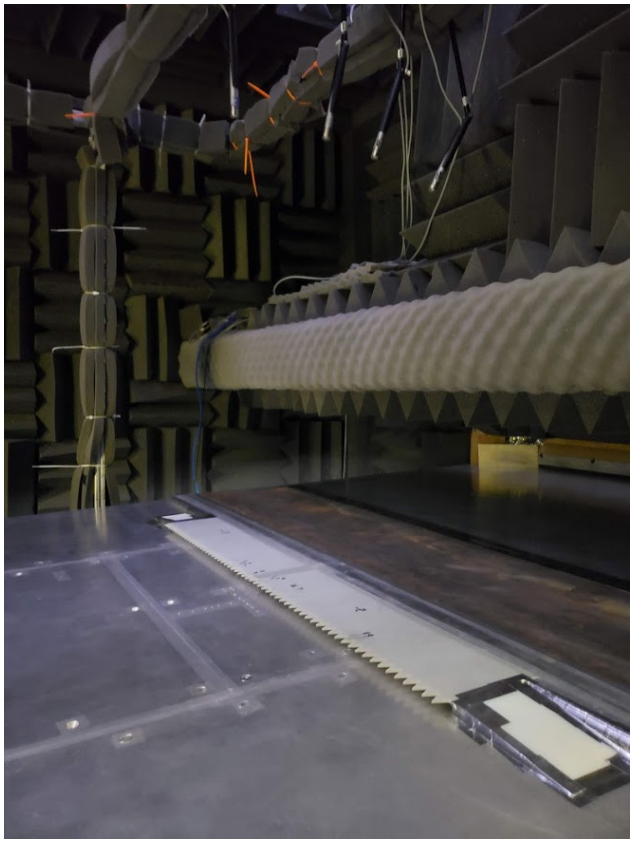

Figure 2.29, Serrated trailing edge and far field microphones in wall jet.

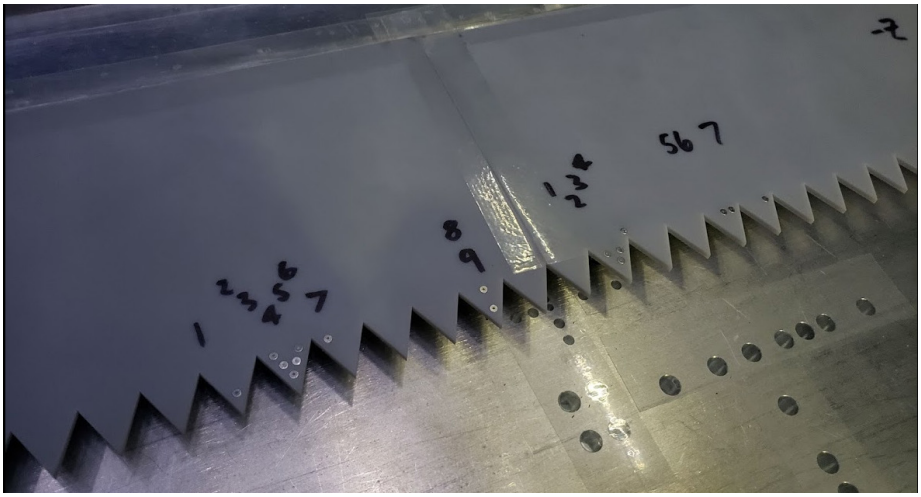

Figure 2.30, Microphones mounted in serrated trailing edge.

Table 2.9, Far field microphone positions for serrated trailing edge experiments.

Mic	x_1 (m)	x_2 (m)	x_3 (m)	$\lvert\vec{x}\rvert$ (m)	θ (°)
1	-0.3620	0.6286	-0.00635	0.7254	119.9
2	-0.2492	0.6715	0	0.7163	110.4
3	-0.1556	0.6905	0.00635	0.7079	102.7
4	-0.003175	0.7033	0.009525	0.7033	90.26

As before, the far field microphones were aligned to point directly at the trailing edge using a laser. To correct for the slight radial distance differences between this setup and that of the straight trailing edge for comparison, the measured pressures in both setups were normalized to $|\vec{r}|$ = 1 m using the inverse square law.

2.6 Beamforming Array

An important step in characterizing the sound production of the straight trailing edge was to ensure that the source of the observed sound is the turbulence being scattered by the trailing edge. This is done using a technique called beamforming, which is used in a wide variety of acoustics applications to determine the locations of sound sources. In this work, a common beamforming technique, delay and sum beamforming, was used to characterize the sound produced by the trailing edge.

2.6.1 Array Design

In this experiment, the linear microphone array designed and manufactured by Alexander [38] was used. A long Delrin block with aluminum mounting pins on each end has 36 holes drilled into it, each designed to fit a B&K Type 4190 microphone-preamplifier such that its face is flush with the face of the block. The microphones are spaced 15.1 mm apart, which was the closest spacing possible. The mounting pins are connected to aluminum mounts, which can be attached to the 80/20 gantry hanging over the plate.

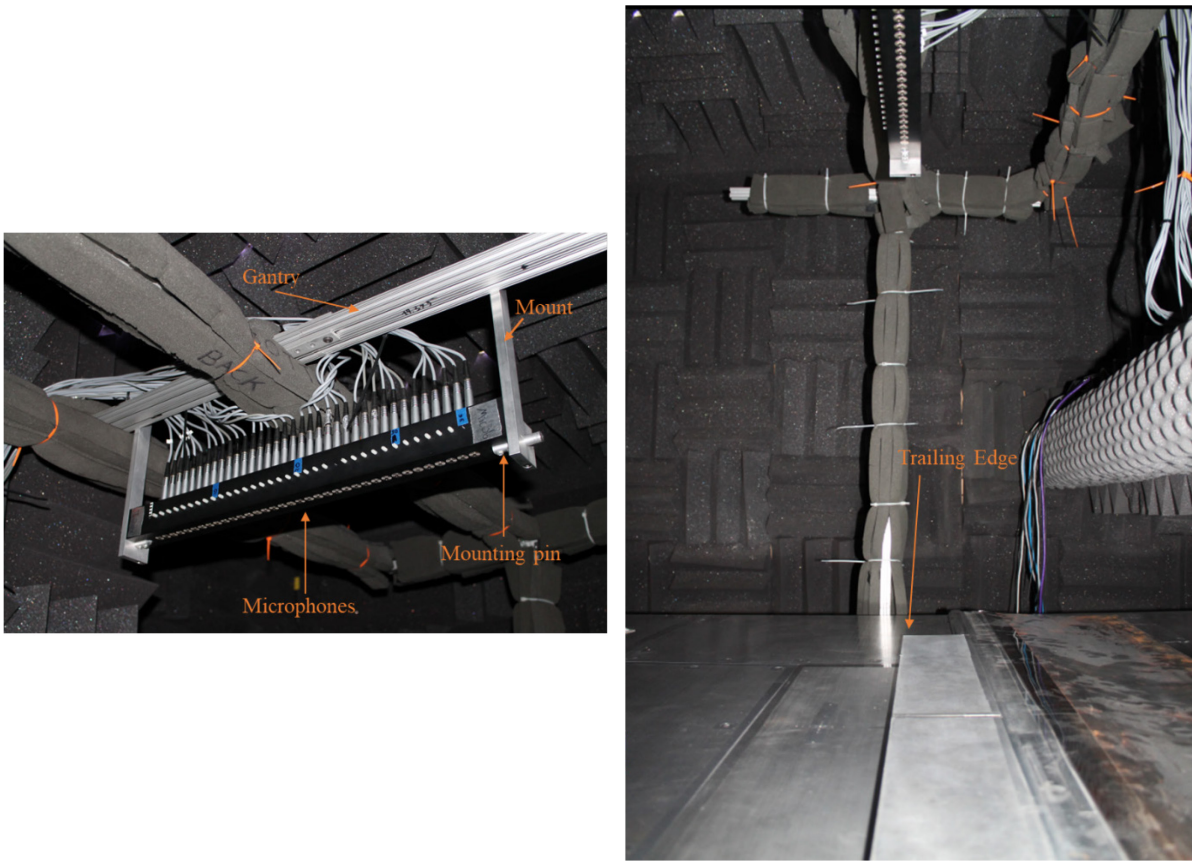

Figure 2.31, Linear microphone array for beamforming experiment.

Figure 2.31 shows the linear array in both orientations, streamwise and spanwise, mounted within the wall jet. The center of the array, between Microphones 18 and 19, is placed directly overhead of the coordinate system origin. In the streamwise orientation, this height is 0.8041 m, and in the spanwise orientation, this height is 0.7818 m. Note that the edge rounding pieces are not present for this experiment; the beamforming results are what prompted the addition of these rounding pieces.

2.6.2 Delay and Sum Beamforming

Delay and sum beamforming is commonly used in aeroacoustic applications because it is capable of characterizing a wide range of potential sources and their distribution.

Billingsley and Kinns [53] contributed an early study of how a microphone array could be used to ascertain a spatial distribution of sound sources. Consider a monopole in free space with a linear array of microphones distributed along x_1, as shown in Figure 2.32:

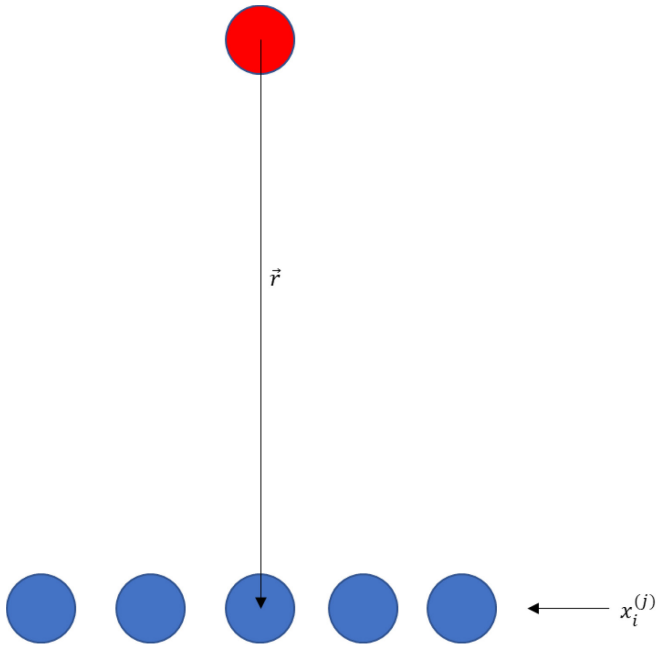

Figure 2.32, Acoustic monopole in free space with linear array of microphones.

Assume that the source is in the acoustic far field. The wave fronts striking the linear microphone array can then be approximated as linear themselves, and thus each microphone would see the same instantaneous signal, and the array output could be calculated by simply summing the microphone signals and dividing by the number of microphones. If the position of the source is moved such that it is no longer aligned with the center of the array, but the positions of the microphones stay the same, the microphones will no longer all see the same signal. The signal at each microphone is phase-shifted.

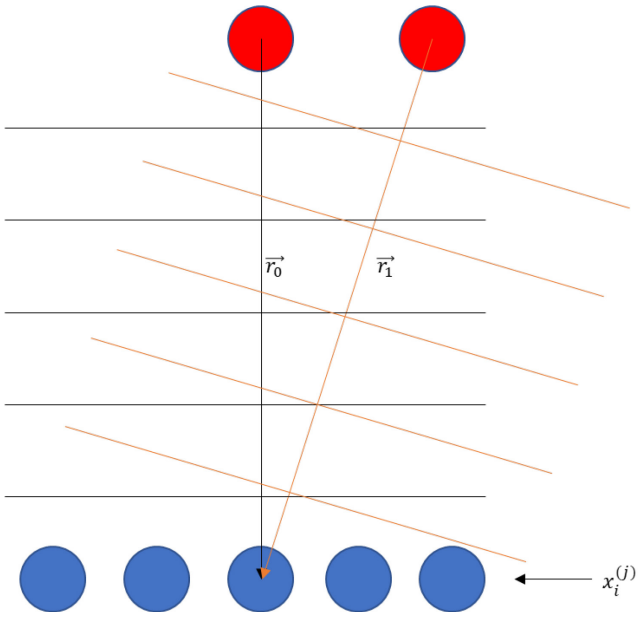

Figure 2.33, Two acoustic monopoles in free space with linear array of microphones.

As shown in Figure 2.33, the signal seen by the array microphones from the source at position $\vec{r_1}$ introduces a time delay component to each microphone signal, and this is the key to forming a map of the acoustic source.

As the microphone signals are summed, there will be destructive interference introduced by phase delay. To determine a source location, the array can either be physically rotated to point at a known source, or a time delay can be introduced to the signals during processing that simulates rotating the array. This time delay is introduced as a phase delay in the Fourier-transformed pressure signal given by each microphone. It is this delay that gives the procedure its name, "delay-and-sum beamforming".

When delay-and-sum beamforming is used as a diagnostic, a map of source locations is prescribed and the array is mathematically focused onto each point to determine the output. If the source is at or near the investigated location, the array output at that focus point will be higher; otherwise, the array output will be very weak. By repeating this procedure over a large range of focal points, an acoustic "image" can be formed of the distribution of source

strength within the source region; Billingsley and Kinns originally proposed the method as a way to characterize jet engine noise.

If the cross spectral density matrix of the individual recorded signals in the array is known, it can be used to calculate the output of the array at a given focal point as well. Tester and Glegg [54] showed that the output of the phased array for a range of sources can be written as

$$\boldsymbol{B}(\omega) = \boldsymbol{G_{inv}} \boldsymbol{C} \boldsymbol{G_{inv}^{H}} \tag{2.12}$$

where each row of $\boldsymbol{G_{inv}}$ is a steering vector that focuses the array on the jth focal point, and $\boldsymbol{C}$ is the cross spectral density matrix at the investigated frequency ω. The superscript H denotes the Hermitian transpose, which is a complex-valued matrix transpose that additionally replaces all its values with their conjugates. If the source field is assumed to be composed of uncorrelated monopole sources, then each diagonal element of $\boldsymbol{B}$ is the output from focusing the array at the jth investigation point and each off-diagonal element is ignored. Therefore, to use this matrix calculation, the investigated points must be rearranged into a single vector and later reshaped into a mapping of the source distribution.

Following Alexander [38], the steering vectors are calculated as the inverse of the Green's function for a monopole, given by:

$$G_{inv}^{(jm)} = \frac{e^{-ikr_{jm}}}{\sqrt{M}} \quad r_{jm} = \left|\vec{x}_m - \vec{y}_j\right| \tag{2.13}$$

This formulation for $\boldsymbol{G_{inv}}$ accounts for both phase delay and amplitude decay of the propagating sound. The designation of $\boldsymbol{B}$ as a function of ω becomes clear here, as each investigated frequency will result in a different steering vector acoustic wavenumber. Additionally, a factor of $M^{-1/2}$, where M is the number of microphones, is included; this accounts for the division by number of array elements, as there are two factors of $\boldsymbol{G_{inv}}$ in the formulation.

2.6.3 Beamforming Performance of the Linear Array

To understand the results of the beamforming algorithm, it is also important to note the response characteristics associated with the specific array configuration. To this end, two parameters must be calculated: the point spread function and the beamwidth. The point spread function is the array's theoretical response to a monopole in the target region. This is determined by computing the theoretical cross spectral density matrix of the monopole signal as measured by the array. The beamwidth is a portion of the point spread function and is defined as the range about the peak at which the signal is within 3 dB of the peak value along the axis of the array ($x_3 = 0$). This is shown in Figure 2.34, with the 3 dB cutoff marked.

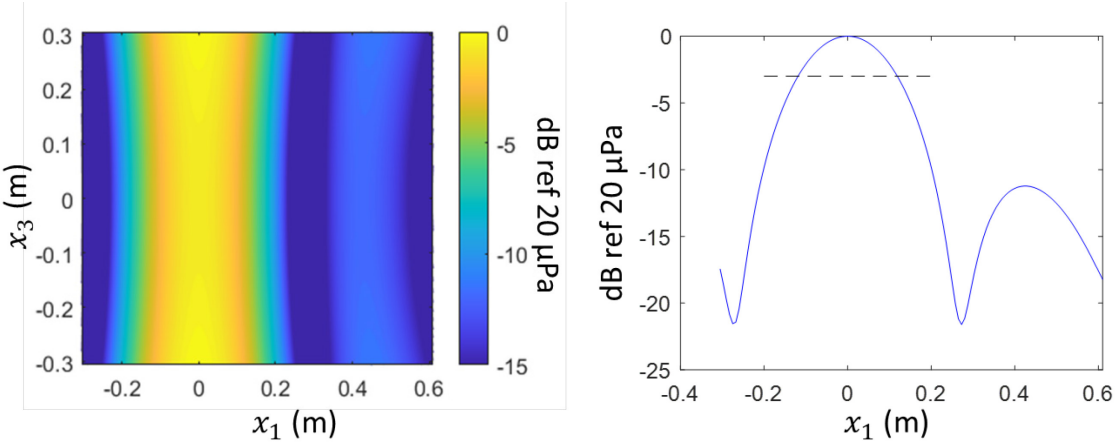

a) Point spread function **b) Beamwidth**

Figure 2.34, Point spread function and beamwidth for $f = 2000$ Hz monopole at origin, normalized on peak value.

Knowing the point spread function of the array at a given frequency is important because it shows how the array will interpret a point source at a given frequency due to the spatial resolution that the algorithm provides. The result in Figure 2.34, for example, shows that even though the source is a single point, it will manifest as a spanwise band of width 0.235 m. This means that a widely spread band at lower frequencies does not represent a wide region of sources spread out over the region of the trailing edge, but rather that the trailing edge itself is definitively the noise source. The beamwidths for $f = 6000$ Hz, 10000 Hz, and

15000 Hz are 0.07 m, 0.04 m, and 0.025 m, respectively. Another important detail to note is that even though the source is a point source, it manifests as a wide band. This is because the array has zero resolution in the spanwise direction (when in the streamwise configuration), and thus only points along $x_3 = 0$ represent real data for the streamwise results, and vice versa for spanwise results.

Another feature to be noted in Figure 2.34a is the spurious lobe appearing in the point spread function at and above 2000 Hz; at higher frequencies, these lobes are more numerous. This is due to the linear, equally spaced arrangement of the array microphones and will be further discussed in Section 2.7.

2.7 Wavenumber Filtering

As stated in Section 1.2, it is desirable to measure the surface pressure spectrum at zero spanwise wavenumber to make a prediction using Amiet's theory. This represents the case of plane waves with wave fronts that are parallel to the trailing edge. This wavevector content is the dominant source of trailing edge noise within the turbulent boundary layer.

Measuring this zero-wavenumber content requires use of a wavenumber filter. Corcos [55] modeled the response function of a single transducer to show how a single transducer of finite size could act as a wavenumber filter all by itself. He also showed that a very large transducer is capable of differentiating between convective and acoustic components of the surface pressure spectrum. As the size of the transducer increases, the magnitude of the needed attenuation correction increases. This effect was later developed by Blake and Chase [46] and Farabee and Geib [47], and becomes the analysis laid out in 2.3.1. However, using a large transducer is quite impractical and can be disruptive to the flow.

Thus, it becomes practical to use an array of surface pressure microphones to discretely sample the pressure field in space. As before, the data from each individual transducer in the array is summed and divided by the total number of transducers, and the array will have a different response depending on the spatial scale of the waves it is measuring. The response function of the array, therefore, depends on both the response functions of the individual

microphones and the response characteristics of the array, which can be affected by both the arrangement of the microphones and how each signal is weighted.

The measured response of a wavenumber array to a surface pressure field is written as:

$$\phi_m(\omega) = \iint |S(k_1, k_3, \omega)|^2 \phi(k_1, k_3, \omega) dk_1 dk_3 \tag{2.14}$$

where $S(k_1, k_3, \omega)$ is the spatial and temporal response of the microphone array. The temporal response is encapsulated in the frequency calibration performed in Section 2.3.2. The total wavenumber response component $|W(k_3)|^2$ of a microphone array that is linear along $\overrightarrow{x_3}$ can be generalized by [46,56]:

$$|W(k_3)|^2 = |H(k_3)|^2 |A(k_3)|^2 \tag{2.15}$$

where $H(k_3)$ is the response function of a single microphone and $A(k_3)$ is the array response function. The function $|H(k_3)|^2$ has already been shown in Section 2.3.1.

Literature regarding wavenumber filtering arrays is largely focused on equally spaced linear arrays with identical microphones. Maidanik and Jorgensen [56] described the construction of a wavenumber filter from linearly spaced circular microphones, and showed that in an arrangement of equally spaced microphones, altering the weighting of the sensitivities could produce different response functions from the same arrangement of microphones. The geometry of each individual transducer and the way they are arranged affect the output of the array as well; each different shape of diaphragm will have its own spatial response function, and the arrangement of the microphones and the weighting on each signal can be tuned to accept or reject specific ranges of wavenumbers, as Maidanik and Jorgensen showed. As an example, their derived $\left|A\left(\vec{k}\right)\right|^2$ takes the following form when the microphone signals from an equally spaced array of N microphones in the $\overrightarrow{x_3}$ direction (each transducer separated by Δx_3) are simply added together:

$$\frac{|A(k_3)|^2}{s^2} = \frac{\sin^2(1/2Nk_3\Delta x_3)}{N^2\sin^2(1/2k_3\Delta x_3)} \tag{2.16}$$

Note that this formulation of $|A(k_3)|^2$ is sensitivity-normalized, where s is the sensitivity of each microphone, assuming that all microphones have equal sensitivity. At first glance, this function has an obvious peak value and narrow lobe at $k_3 = 0$, and since this function is part of a greater transfer function between the measured pressure spectrum and the actual pressure spectrum, this should theoretically suppress signals measured from wavenumbers $k_3 \neq 0$. However, this is actually not the case; it can be clearly seen in Equation (2.16) that at each $k_3 = \frac{j2\pi}{\Delta x_3}$, where j is an integer, a response lobe of equal magnitude is produced. While this does account for $k_3 = 0$, it also adds strong unwanted side lobes. Maidanik and Jorgensen proposed countering this by coupling the size of the transducers and their transducer response functions to the separation distance to suppress the unwanted side lobes by nature of the individual transducer response functions. This principle is used in the works of Blake and Chase [46] and Farabee and Geib [47], who both attempted to measure the low-wavenumber components of the wall pressure spectrum of a turbulent boundary layer. In both cases, facility noise was found to be a significant contaminant. Blake and Chase suggested that adding more microphones to the array would help reduce this problem.

As shown in Figure 2.7, the strong side lobe contamination is due to the repetition of microphone spacings (Δx_3). Logically, it follows that these strong side lobes can be reduced by using an unequal spacing of microphones. For example, using this concept, Arguillat *et al.* [57] used a circularly arranged, rotating, flush-mounted array of 63 microphones and were able to obtain measurements of the two-dimensional wavenumber spectrum of flow in an acoustically treated wind tunnel. Their array was able to separate the convective and acoustic fluctuations. They found that the convective region was up to 15 dB stronger than the acoustic region and that pure acoustic fluctuations accounted for just 5% of the total pressure fluctuations, illustrating the difficulty of measuring the acoustic region. They also found that the measured convective region agreed well with Corcos's model of the convective region [55]. Ehrenfried and Koop [58] showed that an array of 48 sensors in which nearly every

combination of sensors had a unique total separation distance was able to adequately deconvolve the measured frequency spectrum into its wavenumber components with a more uniform resolution in wavenumber space. They used the DAMAS2 beamforming technique on the array signals with steering vectors based on the separation distances between microphones. While they were able to measure the convective ridge quite well, they were unable to confidently identify acoustic components of the wavenumber spectrum, suspecting contamination from trailing edge noise radiating upstream and side lobes of the beamforming result, as well as background noise. They concluded that the deconvolution technique is able to help reduce the influence of background noise, but it is unable to fully overcome the shortcomings of the limited number of sensors, which reduces the spatial resolution of the array. Regardless, they were still able to show that the influence of the acoustic region is much greater at lower frequencies relative to high frequencies.

In this work, for the straight trailing edge a logarithmic spacing of 16 microphones over a total x_3 range of 540.8 mm was used. The logarithmic spacing was chosen to have a good range of both shorter and longer separations, while avoiding repetition of microphone spacings which would give unwanted side lobes in the array response $|A(k_3)|^2$. The (sensitivity-normalized) array response can be calculated by:

$$|A(k_3)|^2 = \frac{1}{N^2}\sum_{i=1}^{N}\sum_{j=1}^{N} e^{-ik_3 r_{ij}} \qquad (2.17)$$

$$r_{ij} = \left|\overrightarrow{x_i} - \overrightarrow{x_j}\right|$$

In this equation, r_{ij} is the distance between microphones x_i and x_j in the array. Summing the cross spectral density of the entire array at each separation distance gives the total wavenumber response of the array at each wavenumber.

The wavenumber response function of this array assuming each microphone is an ideal sensor is shown in Figure 2.35 as a fraction of the maximum output and compared to an equally

spaced array with $\Delta x_3 = 36.1$ mm, which represents Equation (2.16) evaluated for $N = 16$ (as is the case here), and an equally spaced array with $\Delta x_3 = 3$ mm.

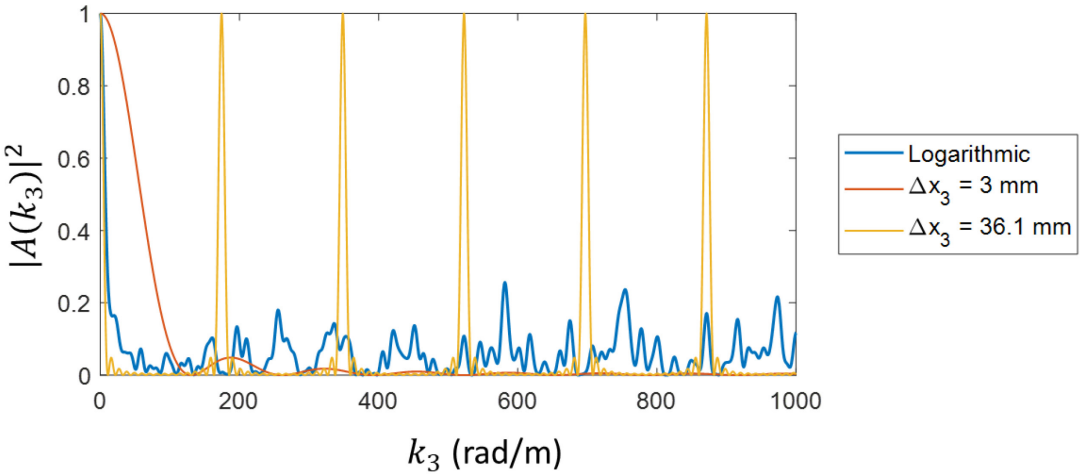

Figure 2.35, Wavenumber response function $|A(k_3)|^2$ for different microphone spacings.

Figure 2.35 shows that the logarithmic array rejects wavenumber content by an average of about 90% for $k_3 = 0$, with some spurious lobes adding up to 20% of their content. It becomes immediately obvious that a tight microphone spacing is better for rejecting high wavenumber content than a sparse spacing in the context of equal spacing, but for an equal number of microphones the total aperture is reduced. This reduces the spacing between sidelobes in the response. Ehrenfried and Koop showed this in their work in an experimental context, though it has been known since the work of Maidanik. The logarithmic array has its strongest lobe at $k_3 = 0$, with several weak spurious lobes distributed throughout the entire wavenumber spectrum. As the response function is squared, these side lobes will have drastically reduced magnitude relative to the zero-wavenumber content, providing an adequate rejection of undesired wavenumber content for our purposes.

Finally, the full function $|W(k_3)|^2$ can be computed from Equations (2.8) and (2.17). The results of this computation are shown in Figure 2.36.

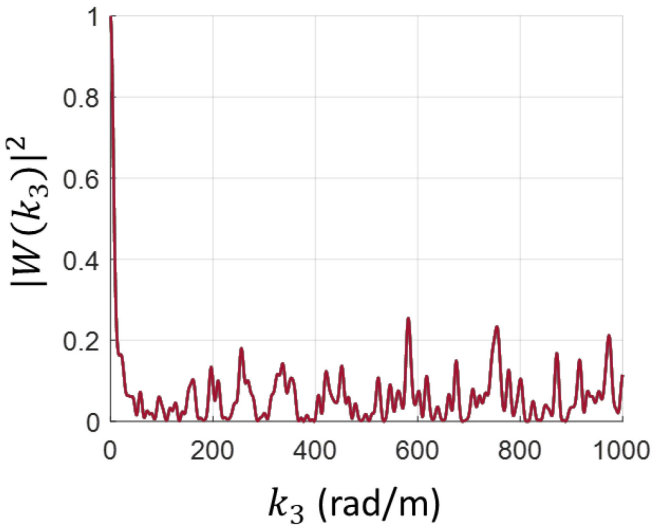

Figure 2.36, Full array response $|W(k_3)|^2$ of wavenumber filter array.

Comparing with Figure 2.35, it is clear that the full array response is virtually unaffected by the individual microphone response. This is due to the very small microphone pinhole diameter, which confines spatial averaging effects to very high frequencies, above 6 kHz.

2.8 Measurement Uncertainty

Before any further results are presented, an analysis of the measurement uncertainty is necessary to contextualize the presented data. Of primary concern are the repeatability of the surface pressure microphone data and far field data recorded by the Knowles FG-23329 microphones and B&K Type 4190 microphones. The uncertainty is introduced in several different manners, including but not limited to inconsistencies in flow conditions due to unsteadiness of nozzle conditions, structural imperfections in the flow region including the sealing tape and flat plate surface, imperfections in the mounting of surface pressure and far field microphones, placement errors in positioning the trailing edge, and averaging uncertainty, as defined in Section 2.2.4.

A potentially major source of uncertainty was the unsteady conditions in the tunnel as measured at the nozzle. The tunnel speed was controlled by measuring the flow temperature

and dynamic pressure and using them to compute the flow speed at the nozzle. The measured velocity was observed to fluctuate by about ± 0.3 m/s throughout the course of a data run. Additionally, the atmospheric pressure and temperature were not constant between data runs. The atmospheric pressure changed over a total range of about 5.2 mbar, and the temperature changed by about 0.3 K. Using the Wygnanski functions (Equation (2.1)), the expected variation in the flow parameters at the edge due to variations in atmospheric conditions and nozzle velocity was found to be less than 1% for all values except for U_e at $U_j = 15$, 20, and 30 m/s. These uncertainties are $\pm 2.11\%$, $\pm 1.58\%$, and $\pm 1.05\%$, respectively. With the U^5 scaling predicted by Ffowcs Williams *et al.* and Amiet, this predicts a maximum far field noise variation of ± 0.45 dB at low speeds.

After computing averaging and nozzle uncertainty, the measurement uncertainty can be examined. This involves taking repeated measurements and comparing them to show the repeatability of a given measurement. Measurements taken at the same flow conditions from the same location are expected to be the same between runs, and the variation in the curves determines the measurement uncertainty. In Figure 2.37, the surface pressure measurement uncertainty is assessed; it shows a view of the full acoustic spectrum as well as a zoomed-in section at medium frequency, the region of highest confidence in validity of Knowles measurements.

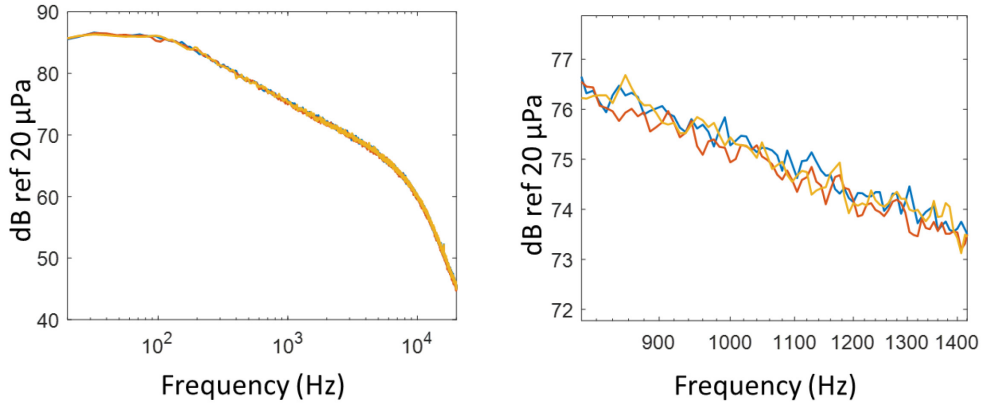

Figure 2.37, Repeatability comparison for three runs of data measured by microphone 13 on the straight trailing edge at $U_j = 70$ m/s.

Figure 2.37 implies a total uncertainty of ± 1 dB for surface pressure measurements from the Knowles microphones. This accounts for averaging uncertainty, flow condition fluctuations, and structural imperfections in the flow region; however, it does not account for uncertainty introduced by taking down and re-setting up the testing apparatus. Nonetheless, this is a reasonable amount of uncertainty for such a measurement.

Data from these same three 70 m/s runs were used to examine the far field noise repeatability in Figure 2.38.

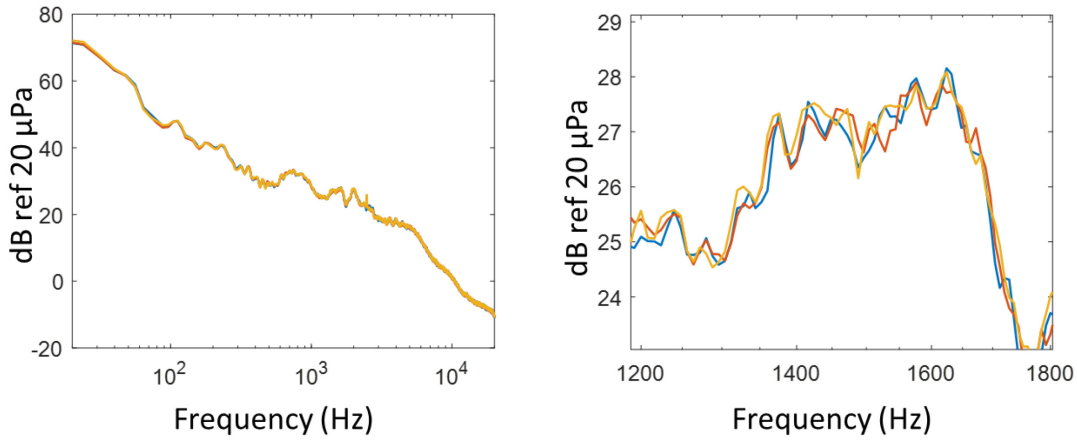

Figure 2.38, Repeatability comparison for three runs of data measured by microphone 1 in the far field of the straight trailing edge at $U_j = 70$ m/s.

Taking the previous statements into consideration, the uncertainty in the far field noise is estimated to be ± 1 dB as well. This is because while the far field microphones are of much higher quality than the surface pressure microphones, the number of factors contributing to far field noise that can introduce uncertainty is much greater, as detailed above.

Finally, the uniformity of the spanwise surface pressure spectrum must be considered. While variations in the boundary layer across the flow are small [37], they must still be considered as the dynamic pressure varies with velocity squared. Additionally, inconsistencies and errors in installation can introduce discrepancies to the surface pressure spectrum downstream. To

this end, autospectrum data from all microphones embedded in the straight trailing edge at once are presented in Figure 2.39.

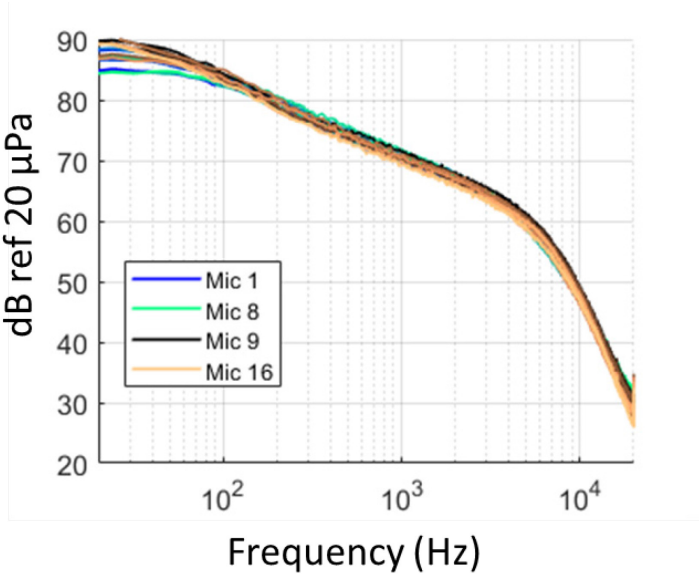

Figure 2.39, Surface pressure spectrum uniformity measured at $U_j = 50$ m/s.

Figure 2.39 shows that the spread of the surface pressure spectrum across the trailing edge is about 3 dB across the full valid frequency range. These values appear to be randomly distributed throughout the full frequency range; though certain microphones consistently measure lower levels than others, there is no arrangement or pattern to these that is consistent with the geometry. Therefore, this spread is likely due to uncertainty in the sensitivity calibrations and installation inconsistencies. This and the previous uncertainty estimates should be considered when examining the data to be presented in this paper.

Chapter 3. Results and Discussion

3.1 Characterization of Wall Jet Turbulent Boundary Layer

Before any analysis or prediction can be made of the trailing edge noise emitted by the straight trailing edge, the characteristics of the boundary layer producing the noise must be known. Presented here are the results of several experiments done to characterize the flow.

3.1.1 Evaluating the statistically frozen flow hypothesis

To provide baseline expectations of the streamwise flow characteristics, further experiments were conducted with the smooth wall setup shown in Figure 2.16 with the surface pressure microphones in the streamwise orientation (as pictured). The results of this experiment will provide confirmation of the expected valid range of the Knowles microphones, establish a baseline measure of streamwise coherence for comparison with the serrated trailing edge, and confirm that the wall pressure spectrum does not significantly evolve between the measurement location of the spanwise microphone array and the trailing edge, allowing for the prediction of downstream flow conditions from those upstream. The surface pressure autospectra for nozzle velocities of $U_j = 15$ m/s, 40 m/s, and 70 m/s are shown in Figure 3.1.

At low speed, the noise floor of the microphones is visible in the spectra above a frequency of approximately 3 kHz, and at high speed, the low-frequency content of the Knowles microphone is suppressed due to clipping. The increasing spatial attenuation cutoff can be seen as well. In the ranges where the Knowles microphone is expected to work adequately, the spectral levels are similar between the microphones. As the total spatial separation between all three microphones is $\Delta x_1 = 12.3$ mm, this is a good indicator that the single-point measurements made by Knowles microphones 3 mm upstream of the trailing edge will be good representations of the surface pressure spectra scattered by the trailing edge for valid frequency ranges of the Knowles response, a function of flow velocity.

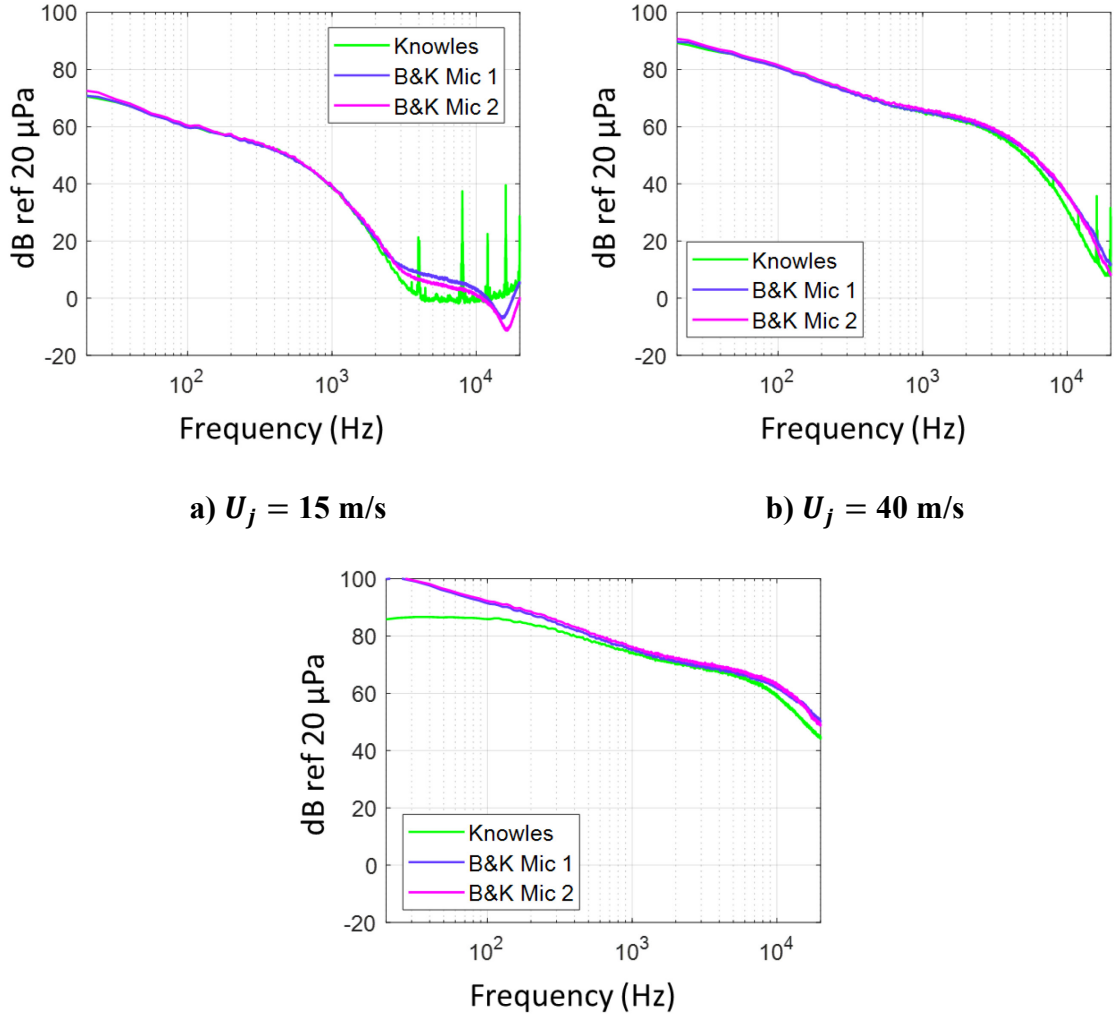

a) $U_j = 15$ m/s

b) $U_j = 40$ m/s

c) $U_j = 70$ m/s

Figure 3.1, Autospectra of surface pressure microphones $\left(\phi_{pp}(f)\right)$ in streamwise orientation in wall jet flat plate.

The streamwise coherence for $\Delta x_1 = 6.05$ mm was also calculated and compared to the model proposed by Leclercq and Bohineust [59], who measured an open-jet turbulent boundary layer flowing along a wall with 42 embedded wall pressure transducers and proposed the following semi-empirical model for streamwise coherence:

$$\gamma^2(\Delta x_1, \Delta x_3 = 0, f) = e^{-2\sqrt{\nu f^3 \alpha^2 \Delta x_1^2 / u_\tau^2}} e^{-2\sqrt{\beta \Delta x_1 u_\tau / (f\delta^2)}} \tag{3.1}$$

In the above equation, ν is the kinematic viscosity of the mean flow, and α and β are empirical constants determined by Leclercq and Bohineust to be 0.43 and 0.25, respectively. Using a wall profile obtained from Equation (2.1), the predicted coherence curves are plotted atop the experimental data in Figure 3.2.

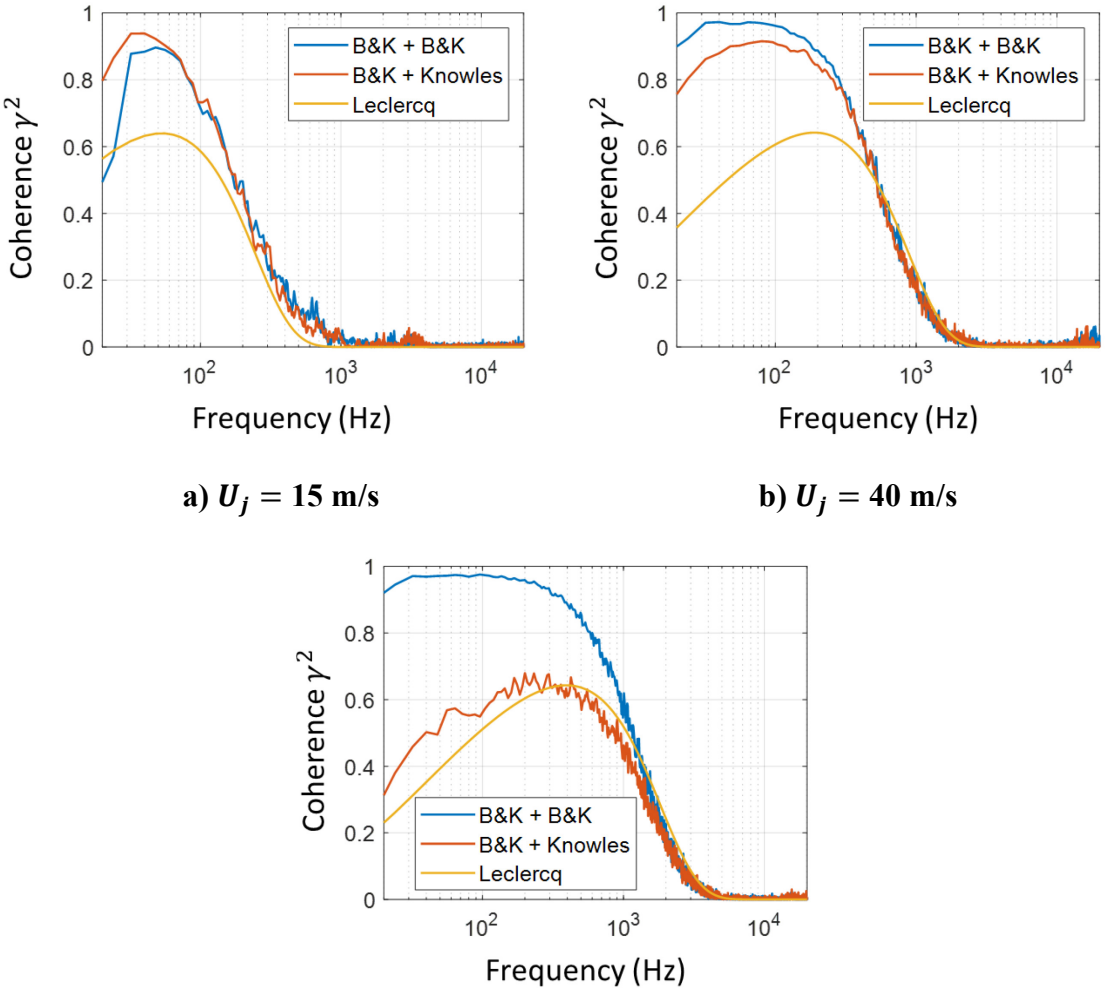

a) $U_j = 15$ m/s **b) $U_j = 40$ m/s**

c) $U_j = 70$ m/s

Figure 3.2, Experimental and predicted streamwise coherence curves for wall jet flat plate.

Leclercq and Bohineust's model is not intended to be used for a wall jet boundary layer, but Figure 3.2 shows relatively good agreement above the frequency at which the coherence is 0.5, with all curves within 0.05 of each other. The model underpredicts the low-frequency coherence over the entire range up to $\gamma^2 = 0.5$; this is due to the nature of the boundary layer being measured. A wall jet contains a large mixing layer with larger, slow-moving eddies above the inner boundary layer, and therefore it is expected that more low-frequency content will be present in the spectrum, and higher low-frequency correlation. The low-frequency cutoff for interpretation of streamwise coherence with the Knowles microphone as defined in Section 2.3.3 was found to be 48 Hz for $U_j = 15$ m/s, 248 Hz for $U_j = 40$ m/s, and 1296 Hz for $U_j = 70$ m/s. The limits determined in Section 2.3.3 for spanwise coherence at these jet velocities (24 Hz, 96 Hz, 800 Hz) are somewhat lower than those found here for streamwise coherence. Nonetheless, this figure is still promising, as it once again shows good agreement between the B&K and Knowles data at frequencies (>1 kHz) and speeds at which trailing edge noise is expected to be observable.

3.1.2 Streamwise coherence length scale

From the coherence curves shown above, a streamwise coherence length scale can be calculated for the flow. The coherence length scale represents an exponential curve fit that describes the coherent power decay rate [60]; this decay rate is a curve fit of the constant-frequency coherence data at different separation distances, and is given by Leclercq and Bohineust [59] to be:

$$\gamma^2 = e^{-\frac{2|\Delta x_1|}{\mathcal{L}_\gamma(f)}} \tag{3.2}$$

The coherence length scale is defined as a frequency-dependent value that is determined by a curve fit of $\gamma^2(\Delta x_1, f)$ vs. Δx_1, varying the frequency to determine the coherence length at each frequency. Thus, physically, it represents the characteristic decay scale in distance along the plate of the coherent structures of the flow for structures with a particular frequency. The coherence length is a similar measure to the correlation length scale, except it enables a separation of scale by frequency rather than producing a broadband measure of characteristic

length. Thus, in the particular case of a wall jet, a correlation length scale calculated from the peak in a cross-correlation measurement instead of the frequency-dependent coherence would be strongly influenced by the large, low-frequency structures in the mixing layer [60]. This would give an inaccurate representation of characteristic turbulence scales associated with the trailing edge noise produced at higher frequencies.

From the B&K-B&K coherence data in Figure 3.2, considered to be of high accuracy, this expected length scale was computed for each jet speed. The results are shown in Figure 3.3, and compared to the size of the serrations and the separation distance between the surface pressure microphones and the straight trailing edge.

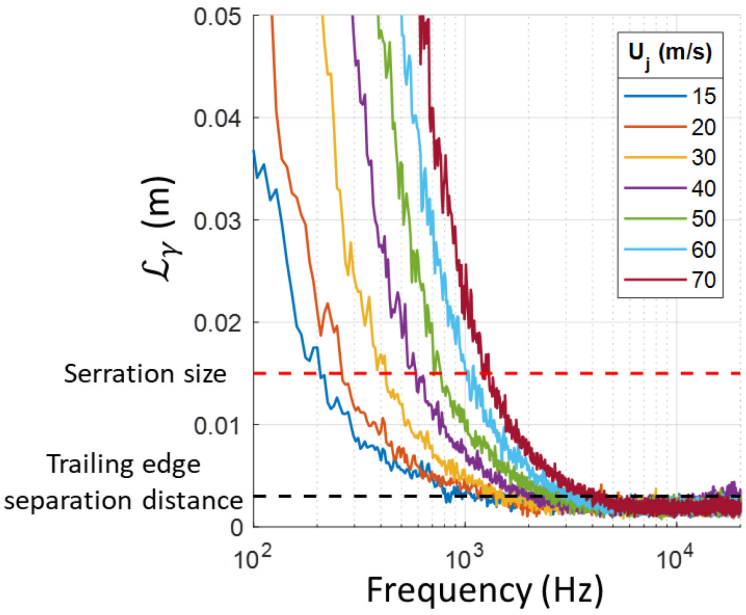

Figure 3.3, Streamwise coherence decay length.

The plot shows that below 1 kHz, the streamwise coherence decay length is greater than the planned separation distance between the microphones and the trailing edge at all flow speeds. This decay length increases with increasing flow speed at fixed frequency. Above 5 kHz, the decay length falls below the microphone and trailing edge separation distance at all flow speeds. The cutoff frequency below which the streamwise coherence length scale is the size

of the trailing edge serrations is 200 Hz for the lowest flow speed and 1300 Hz for the highest flow speed.

3.1.3 Convection velocity

The convection velocity is another important flow parameter that is important to know for a boundary layer flow; for the purposes of this work, it is used to evaluate the frequency range over which the flush-mounted pinhole microphones are spatially attenuated, and is a parameter in many of the wavenumber-frequency wall pressure spectrum models.

To measure the convection velocity, the cross spectra of the B&K surface pressure microphones separated by 6.15 mm was computed and the phase angle of the cross spectra was converted to a time delay. Dividing the separation between the two microphones by this time delay gives the convection velocity as a function of frequency ($\Delta t = \phi_{12}/2\pi f$). This method does require there to be significant coherence between the two microphones, and as such measuring the convection velocity above a certain frequency threshold is difficult. Using $\gamma_{12} \approx 0.1$ as a cutoff, the phase angle and convection velocity for selected jet velocities are shown in Figure 3.4 and Figure 3.5.

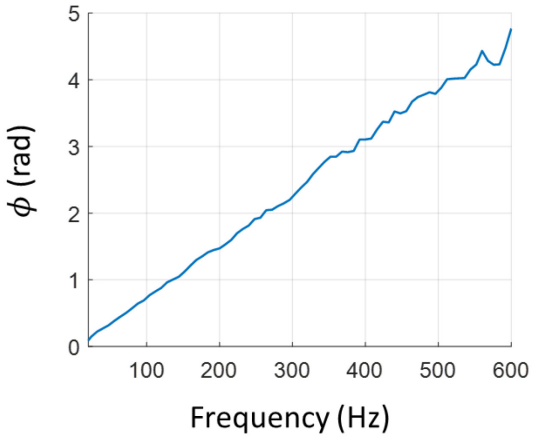

a) $U_j = 20$ m/s

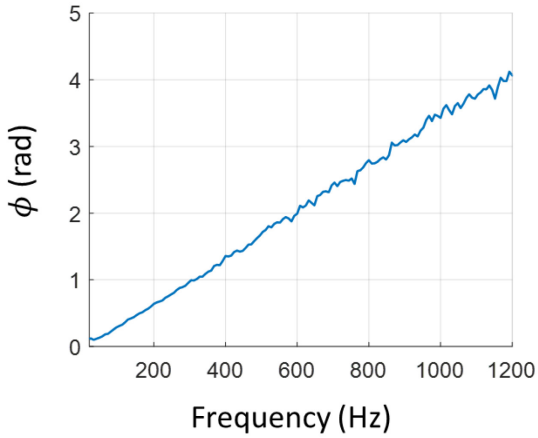

b) $U_j = 40$ m/s

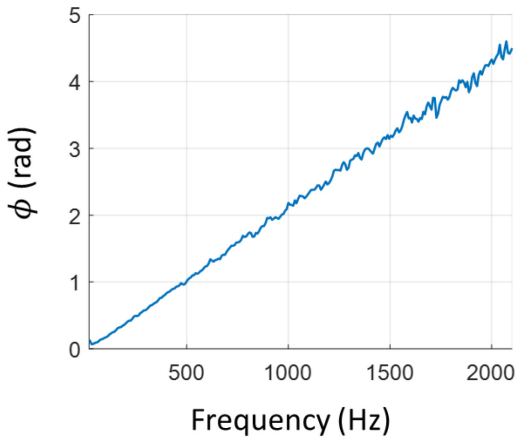

c) $U_j = 60$ m/s

Figure 3.4, Phase angle of cross spectrum between B&K 1/8" microphones mounted in flat plate.

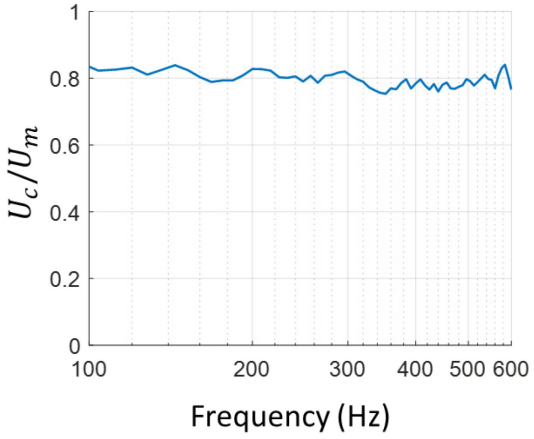

a) $U_j = 20$ m/s

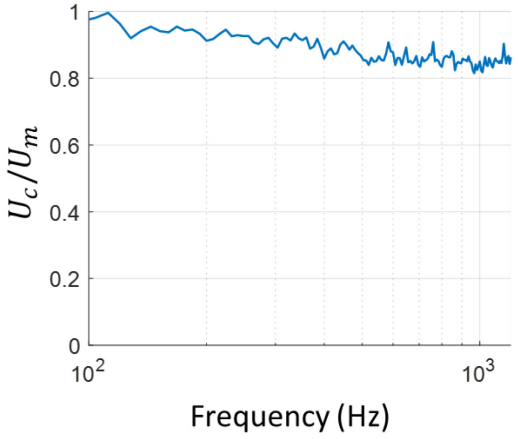

b) $U_j = 40$ m/s

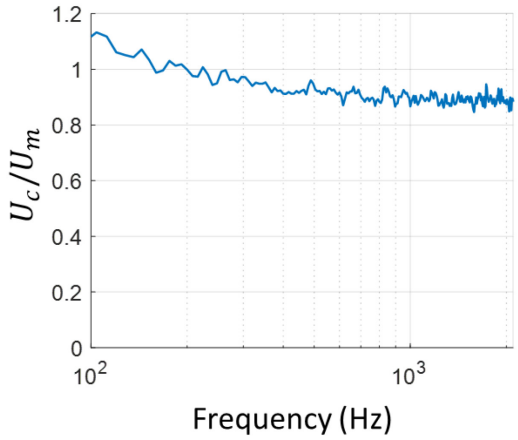

c) $U_j = 60$ m/s

Figure 3.5, Ratio of convection velocity to maximum velocity as a function of frequency.

Figure 3.4 shows the as-expected linear relationship between the phase difference and frequency. This trend exists from 0 Hz all the way up to the cutoff frequency, which is marked as the axis limits on each figure. The slope of each line decreases with increasing jet velocity, indicating that the phase difference for a given frequency decreases with velocity, as expected. Figure 3.5 shows that the ratio of the convection velocity to the maximum velocity tends to increase with jet velocity – from around 0.8 at 20 m/s to about 0.9 at 60 m/s. This trend is likely due to the decreasing thickness of the boundary layer, resulting in mid- to high-

frequency eddies being located closer to the edge of the boundary layer. Note that data below 100 Hz are removed from Figure 3.5; the data in this region show a significant decrease in convection velocity ratio. Pressure fluctuations in this range may be dominated by the very large scales in the outer portion of the boundary layer, which have a much slower convection velocity. As the scales reduce at higher frequency to a scale similar to the boundary layer thickness, corresponding to Figure 3.3, the convection velocity increases. Note that there may be additional contamination at low frequencies as well which produce the anomality in Figure 3.5c where the ratio rises above 1, an impossibility.

To estimate an average value of convection velocity for use in this work, the mean value of the convection velocity ratio in the region above 1200 Hz is computed. This value is chosen because it is the lowest frequency at which trailing edge noise is emitted (see Section 3.2); for velocities without coherence in this frequency range, the average of the flat region of their ratio plots is computed. For $U_j = 15$ and 20 m/s, the lower limit was 100 Hz, and the upper limits were 500 and 600 Hz, respectively; for $U_j = 30$ m/s, the limits were 450 Hz $< f <$ 900 Hz; for $U_j = 40$ m/s, the limits were 600 Hz $< f <$ 1200 Hz; and for $U_j = 50$, 60, and 70 m/s, the upper limits were 1600, 2000, and 2400 Hz, respectively. The computed convection velocities across the jet velocity range used in this study are tabulated in Table 3.1.

Table 3.1, Far field microphone positions for serrated trailing edge experiments.

U_j (m/s)	U_c/U_m
15	0.796
20	0.796
30	0.819
40	0.853
50	0.875
60	0.890
70	0.896

These results do not agree with the results of Devenport *et al.* [48], who found that the convection velocities at $U_j = 40$ m/s and 60 m/s were $0.44U_m$ and $0.41U_m$, respectively.

Some differences do exist between the measurements made in this work and those made by Devenport *et al.*, primarily the frequency range being examined – Devenport *et al.*'s result is found by examining the far field noise produced by a hydrodynamically smooth surface. The designed surface produced noise which corresponds to the scattering of a "cut" through the wavenumber-frequency wall pressure spectrum at a wavenumber $k_1 = 5000$ rad/m. They located the approximate peak of the convective ridge of the wall pressure by examining the peak of the radiated sound field compared to a line with slope ω^2. A convection velocity could then be calculated using the peak frequency of the convective ridge with the associated wavenumber cut, $U_c = \omega_{peak}/k_1$. This process assumes that the measured peak is due to the convective ridge and the form of the wavenumber-frequency wall pressure spectrum is the same for wall jets as it is for conventional turbulent boundary layers. Both methods are theoretically viable ways of measuring the convection velocity, though the one in this work is a direct measurement of the flow field. Therefore, this result neither proves nor disproves the validity of the previous result; rather, it presents another measurement, and invites further investigation into the topic. In this work, where necessary, calculations involving convection velocity will be presented for both the measured result and the result of Devenport *et al.*

3.2 Trailing Edge Noise from Straight Trailing Edge

Now that the wall jet boundary layer is adequately characterized, the measured trailing edge noise can be analyzed. To do so, the trailing edge noise must be separated from the background noise of the facility. To this end, the facility was run without the trailing edge installed, then run with the straight trailing edge. The four far field microphones shown in Figure 2.22 were used to measure the far field noise in both the empty tunnel configuration and trailing edge configuration, and noise spectra were compared to determine which regions of the frequency range experienced increased noise due to the presence of the trailing edge. In the following sections, all far field measurements are distance-corrected using the inverse square relation to a radius of $|\vec{r}| = 1$ m.

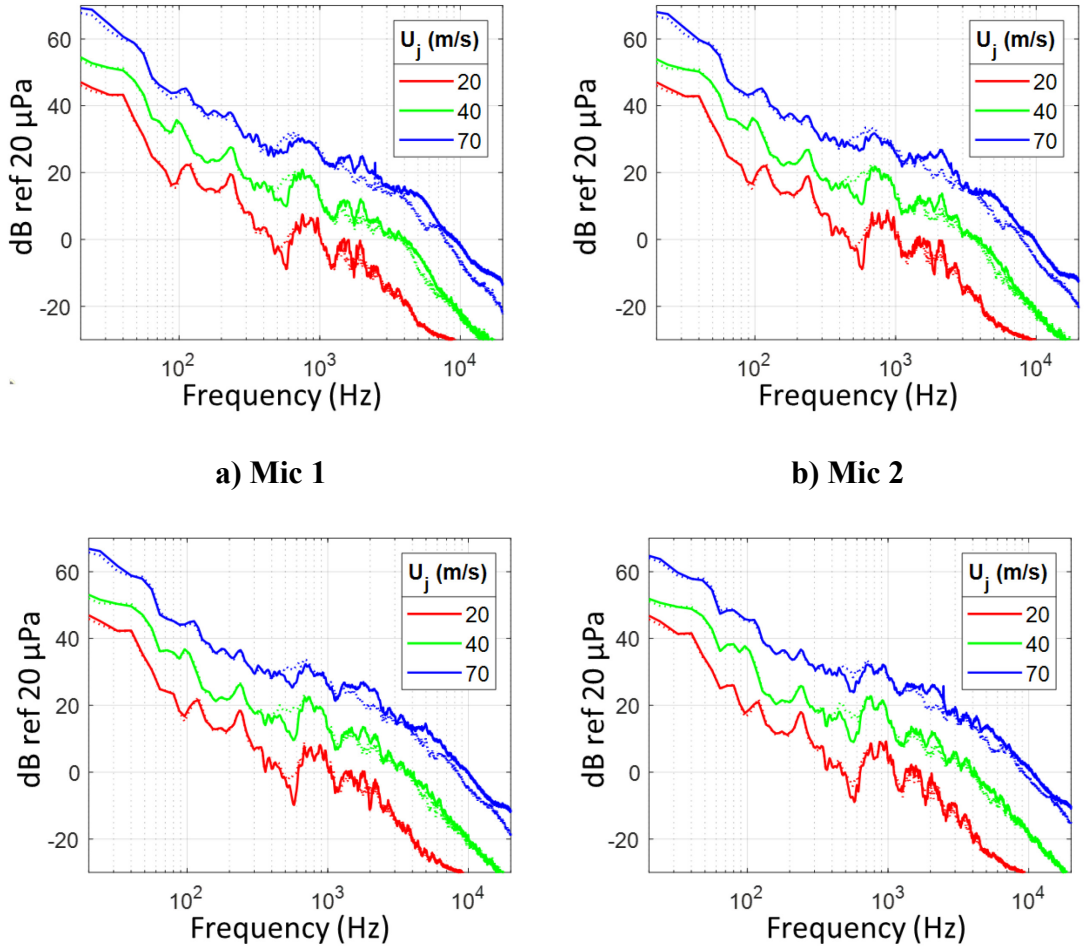

a) Mic 1 **b) Mic 2**

c) Mic 3 **d) Mic 4**

Figure 3.6, Straight trailing edge signal-to-noise, distance-corrected. Dotted lines are background measurements, solid lines are with trailing edge installed.

All four microphones show very little discernible trailing edge noise at low and medium speeds, but the range of trailing edge noise produced is relatively consistent throughout the full range of speeds tested; generally, trailing edge noise is produced at all frequencies above ~1200 Hz. At Mic 1, the maximum noise increase is around 7 dB at 2000 Hz and $U_j = 70$ m/s; for Mic 2, 6.7 dB at 1850 Hz; for Mic 3, 7.5 dB at 1800 Hz; and for Mic 4, 7.5 dB at 2200 Hz. Overall, noise levels appear to be relatively consistent between all four microphones. Using the $\sin^2(\theta/2)$ directivity predicted by Ffowcs Williams *et al.* and Amiet,

the difference between the overhead and upstream microphone trailing edge noise should be 1.69 dB. This should be hardly noticeable on a plot scaled as in Figure 3.6, and is only just outside the uncertainty of the far field measurements. The level of background noise is also observed to increase with further downstream measurement locations, owing to the fact that the horizontal baffle provides better acoustic shielding for the upstream microphones. Mic 1 in particular has a noise reduction of about 1 dB above 1.2 kHz relative to the other microphones.

Now that the observed frequency range of trailing edge noise is established through comparison with background noise spectra, the background noise can be subtracted from the noise measured in the full tunnel setup to isolate the trailing edge noise. In Figure 3.7, this background-subtracted noise is shown at all speeds for frequencies at which the difference between the background and trailing edge setup noise is at least 1 dB. Data below 1 kHz, where increased noise was not observed, has been excluded.

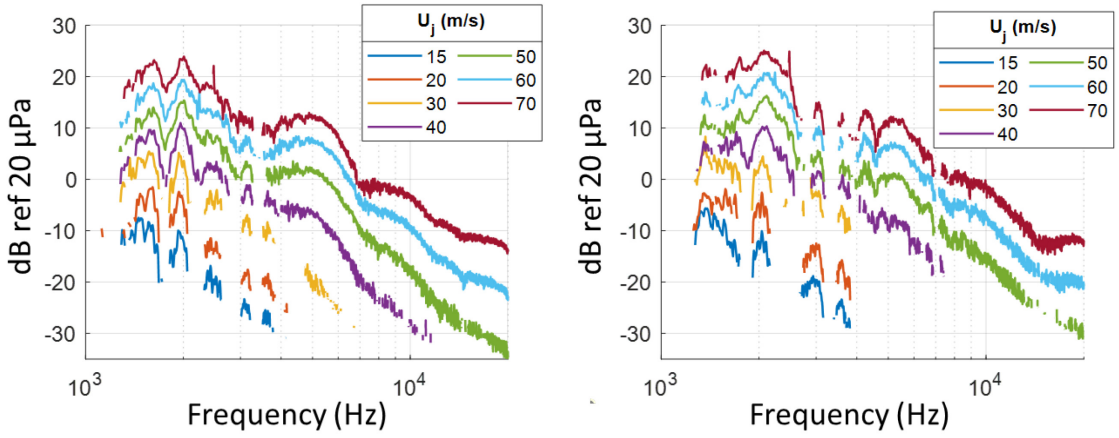

a) Mic 1 **b) Mic 4**

Figure 3.7, Background-subtracted trailing edge noise from straight trailing edge.

The noise from each jet velocity appears to peak at around the same frequency, 2000 Hz for Mic 1 and 2100 Hz for Mic 4, reaching a maximum of 23.9 dB at Mic 1 and 24.9 dB at Mic 4. A good indicator that this measured noise is actually trailing edge noise would be if it follows theoretical scaling relationships, such as the U_m^5 scaling implied by Equation (1.12).

To this end, the full spectra shown in Figure 3.7 were integrated between 1 kHz and 20 kHz to obtain a better representation of the noise produced at each speed, and a line representing a scaling of U_m^5 fitted to the integrated values was plotted over these points. The result is shown in Figure 3.8 on logarithmic axes to show the power fit as a straight line.

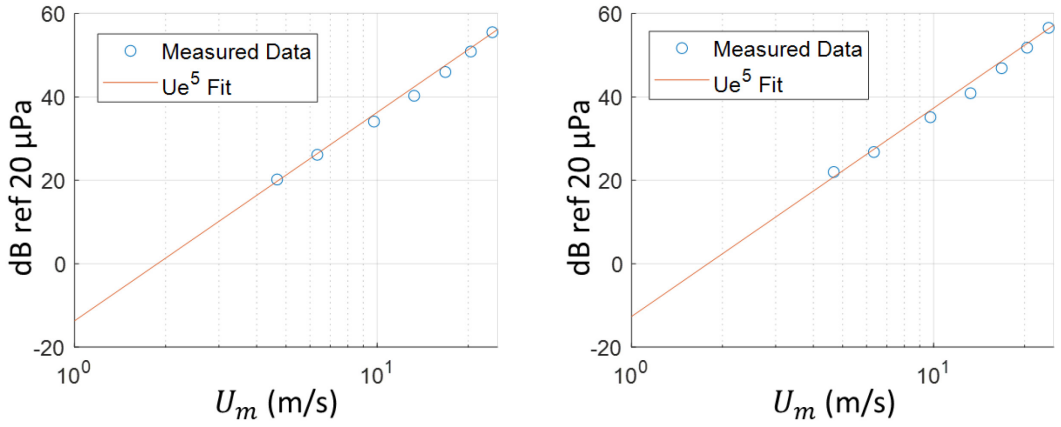

a) Mic 1 **b) Mic 4**

Figure 3.8, U_m^5 curve fit to integrated background-subtracted spectra.

The maximum difference between the curve fit and the integrated spectra is 1.4 dB for Mic 1 and 2.5 dB for Mic 4. This is outside the range of measurement uncertainty, but nonetheless, the U_m^5 scaling seems to match the data, an indicator that what is being measured here is trailing edge noise or at least scales similarly. The slope of the integrated spectra on the logarithmic axes appears to increase as the flow speed increases as well; the data from lower speed is more uncertain due to the limited observed frequency range of data, and thus the higher slope at high speed indicates that the power in the random relationship is likely somewhat higher than 5.

Three distinct humps in the spectrum begin to emerge at higher speeds, becoming more clearly defined as speeds increase, and more clearly defined upstream, where jet noise is better attenuated. Notably, these humps all occur in the same frequency ranges; for Mic 1, they appear to range from 1200 Hz to 3400 Hz, 3600 Hz to 7000 Hz, and 7000 Hz to 12000 Hz. At Mic 4, the frequency ranges are roughly the same, but the humps are much less well-

defined. The general shape of each curve remains self-similar for each microphone position, noting the double peaks at 1750 Hz and 2000 Hz, the double peaks at 4400 Hz and 5200 Hz, and the trough between 2750 Hz and 4100 Hz. The fact that the curves at each microphone are so self-similar suggests that these humps are produced by the geometry of the edge rather than flow phenomena – for example, vortex shedding would occur at a constant Strouhal number, which would mean the frequency of the humps would increase with speed.

What remains to be determined is whether or not these plots are actually displaying noise produced by the trailing edge or the source of the spectral humps.

3.2.1 Beamforming to Identify Noise Sources

The delay and sum beamforming method described in Section 2.6 was used to investigate the location of the noise source at different frequencies. The streamwise array was used to determine the approximate streamwise location of the noise sources, and likewise for the spanwise array. Select frequencies have been chosen for reporting in Figure 3.9. Note that each figure will be symmetric about the array location due to the array being linear – this causes contributions at both positive and negative angles relative to the array to be equal.

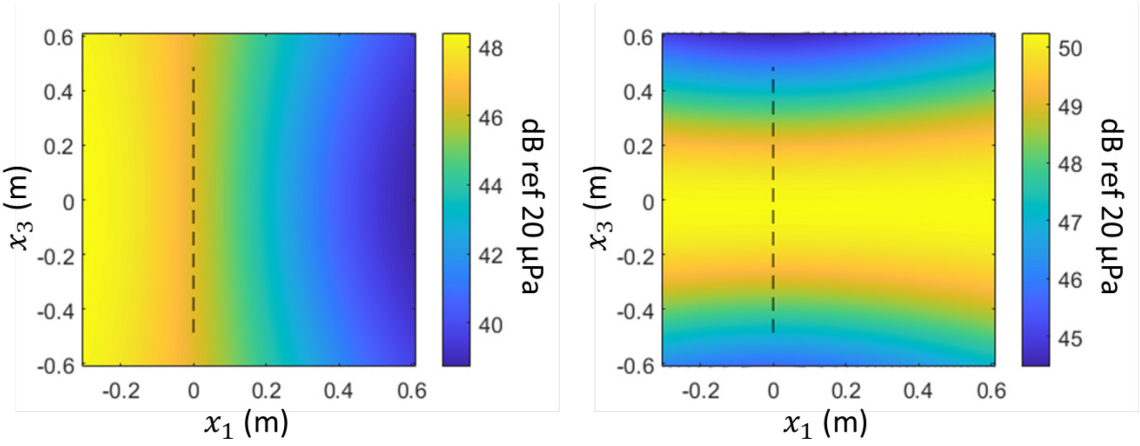

a) 704 Hz

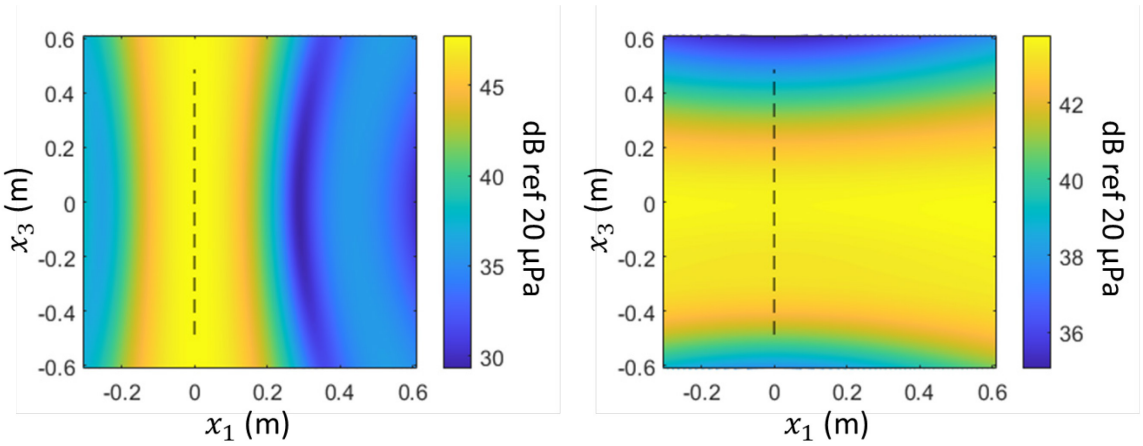

b) 2000 Hz

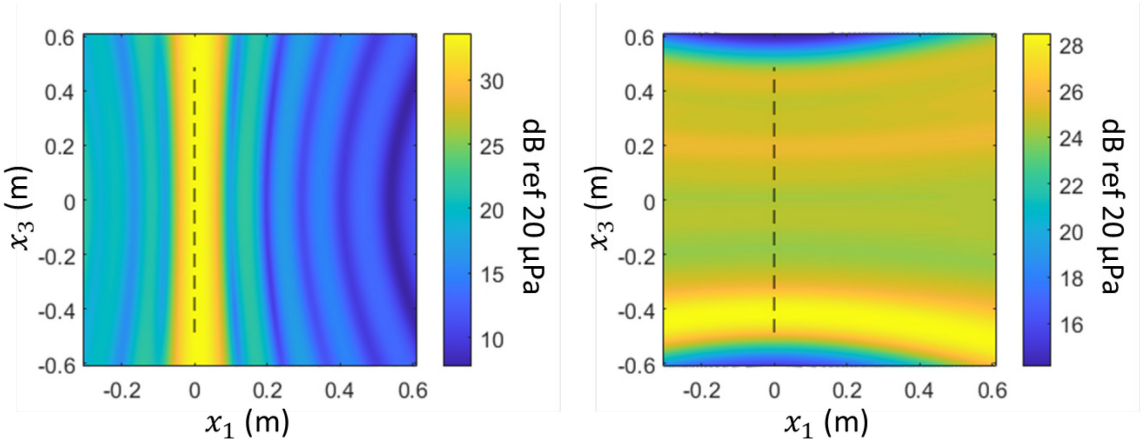

c) 6000 Hz

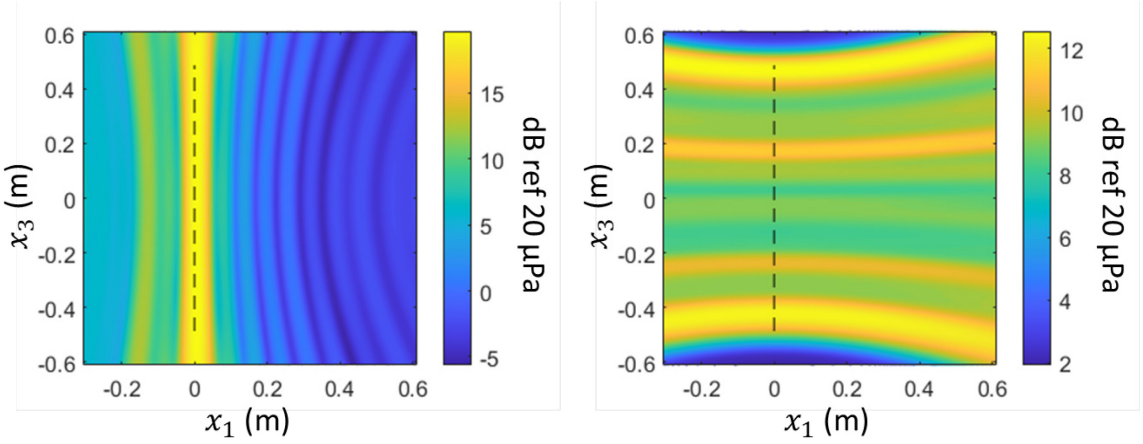

d) 10000 Hz

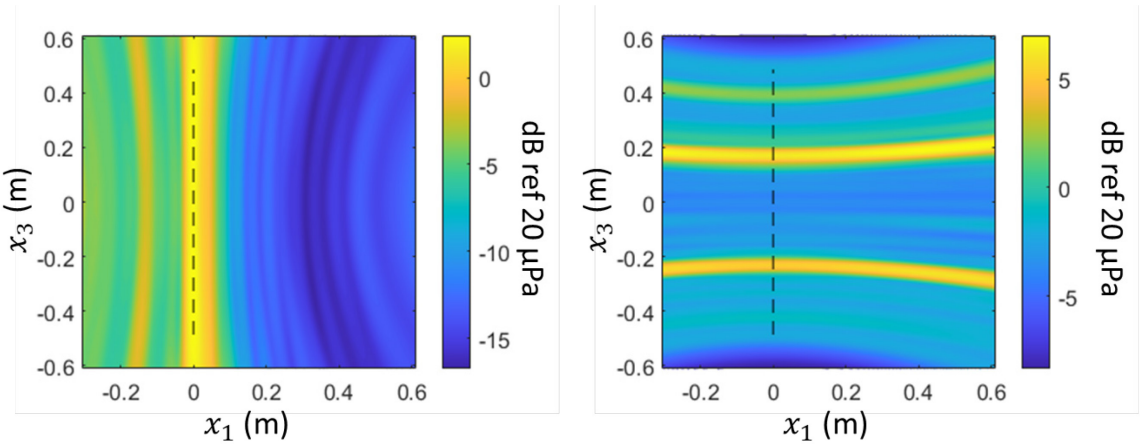

e) 15000 Hz

Figure 3.9, Beamforming experiment results, streamwise array (left side) and spanwise array (right side) at $U_j = 70$ m/s. The black dashed line represents the location of the trailing edge.

From the streamwise results, it is clear that at each frequency above 2000 Hz, the dominant noise source is the trailing edge. The spanwise results confirm that this noise is coming from the trailing edge. The contributions at 6 kHz and 10 kHz tend to come from the unrounded sides of the trailing edge piece. This was a major factor in the decision to add the side-rounding pieces shown in Figure 2.20. Along the black dotted line, the variation in dB of the noise sources along the central region of the trailing edge, x_3 = -0.3 to 0.3 m, is 1.97 for 704 Hz, 2.34 for 2000 Hz, 1.59 for 6000 Hz, 3.14 for 10 kHz, and 10.38 for 15 kHz. At 704 Hz, the dominant source of noise is upstream of the trailing edge region, indicating that this source is jet noise from the nozzle. Each presented frequency was chosen because it represents a neighborhood of the frequency domain over which noise was measured; thus, it is concluded that the sound being measured above 1200 Hz is indeed produced by the trailing edge, although above 10 kHz the spanwise distribution of the noise can no longer be considered uniform with a spanwise variation over the central 0.6 m greater than 2.5 dB.

3.2.2 Cavity Resonance

The humps in Figure 3.7 appear at constant frequencies with increasing flow velocity, peaking roughly at 2000 Hz, 5500 Hz, and 10 kHz. The lack of variation with flow speed indicates that the source of the humps is based on the geometry of the vicinity of the trailing edge. Since the humps occur at the same frequencies across the entire velocity range, the velocity clearly does not affect the frequency at which the hump occurs, meaning that some other constant factor between runs must be responsible (i.e. the geometry).

The humps appear to correspond to modes of an acoustic resonance, which for an open-ended cylinder with one side closed occur at frequencies $f = nc_0/4L$, where n is an odd whole number and L is the length of the cylinder. The quarter-wavelength factor places the theoretical acoustic node at the cavity entrance and the antinode at the closed wall on the other end of the cylinder, and the odd mode numbers are necessary to preserve this relationship. While the open cavity in this experiment is not a cylinder, this formula still approximates the frequencies at which the resonance occurs quite well, assuming the two-dimensional resonance based on cavity depth and ignoring the spanwise modes. Spanwise modes would coincide with much lower frequencies based on the spanwise length of the edge.

The formula above predicts the first three resonant modes to occur at $f = 2259$ Hz, 6777 Hz, and 11295 Hz. These appear to be slightly higher than the frequencies at which the suspected resonance actually occurs, and this is accounted for by an end correction that considers that the node may form slightly outside the opening. This correction factor usually takes the form of adding a fraction of the cavity diameter d to the cavity length; each open end of the cylinder adds $0.3d$ to the effective length of the cavity [61]. Treating the cavity as a single open-ended cylinder places resonant modes at 2054 Hz, 6161 Hz, and 10269 Hz. However, at higher frequency humps this over-predicts the frequency; increasing the end correction to $0.6d$ better approximates the resonance at higher frequency nodes, at 1883 Hz, 5648 Hz, and 9413 Hz. These frequencies are overlaid atop the background-subtracted trailing edge noise from Figure 3.7 in Figure 3.10.

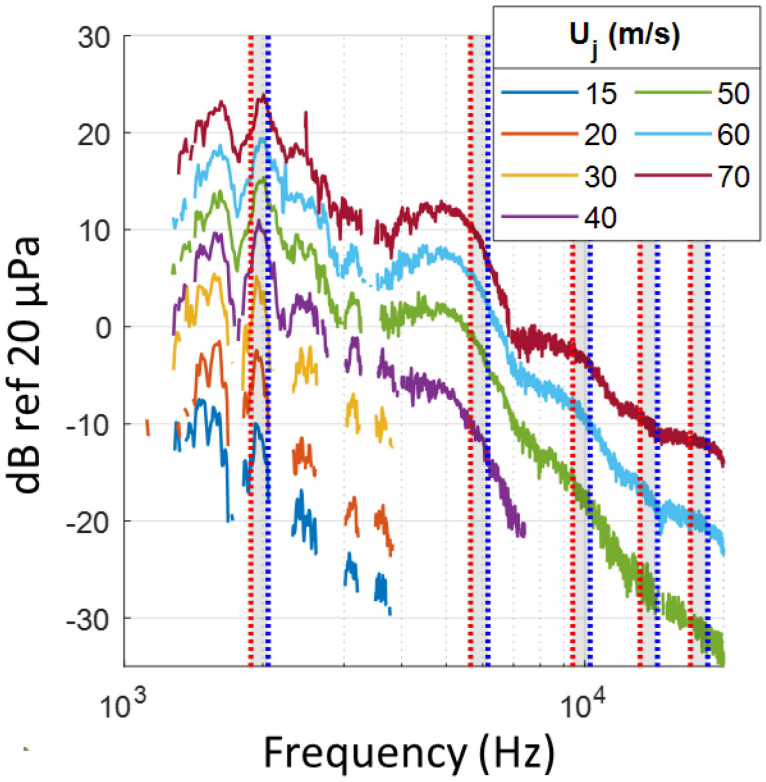

Figure 3.10, Background-subtracted trailing edge noise with predicted resonant frequencies overlaid. Blue dashes are frequencies with correction of 0.3d and red dashes are frequencies with correction of 0.6d.

It can be seen that while the 30% end correction fits the lowest resonant node quite well, neither of the high frequency end corrections are perfect fits to the data. There are two factors that account for this discrepancy: the cavity is not a cylinder, and thus the cylinder model is only useful as an approximation; and the fact that the resonating cavity is flared at the end means that resonances can occur slightly outside of the normal resonant mode frequencies [61]. In all, it is important to note that the humps do appear to multiples of one another and are approximately related to the resonant frequency of a simple quarter-wavelength resonator.

3.2.3 The Image in the Wall

Another potential trailing edge geometry effect is the proximity of the trailing edge to the wall. The sound produced by the unsteady pressure difference across a flat plate radiates as

a dipole, and the wall effectively adds an "image" trailing edge with opposite orientation on the opposite side of the wall, as illustrated in Figure 3.11 simplified to a single 2D dipole. This is a simplification which ignores the true directivity of trailing edge noise, which was expressed in Equation (1.12). The ideal directory is a cardioid which is a result of the loading response of the plate to turbulence scales which are much smaller than the plate's chord. Instead, the simplification in Figure 3.11 ignores the trailing edge plate geometry completely and the ideal acoustic dipole source is located in free space 12.7 mm above the flat wall. This geometric simplification is necessary and sufficient to determine the general impact of the nearby wall on the radiated sound.

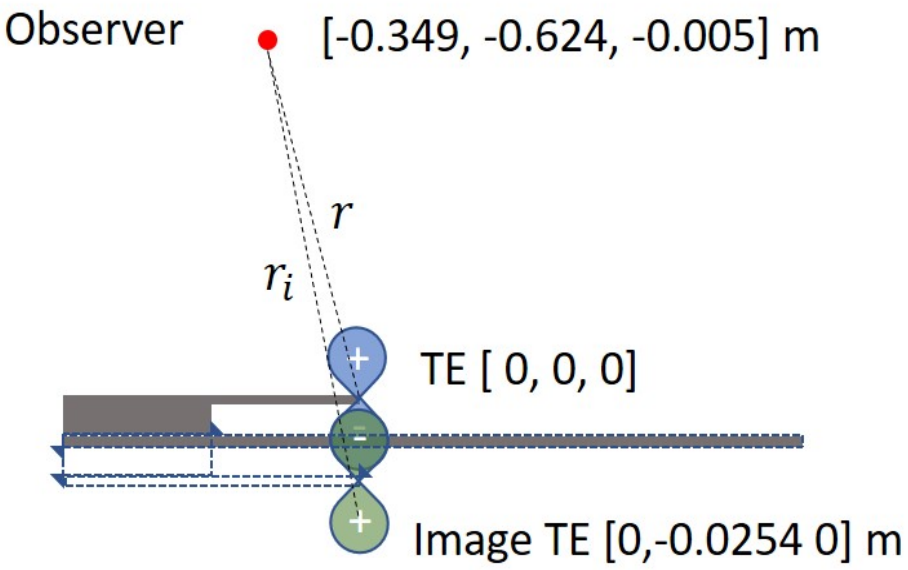

Figure 3.11, Image of the undercut trailing edge in the wall as seen by Microphone 1.

Ideal acoustic sources can be superimposed, and thus the far field noise at the observer is the summation of the sound from the two individual dipole sources:

$$\hat{p}(\vec{x},\omega) = \hat{A}\left(\frac{x_2}{r}\right)\frac{i\omega e^{ikr}}{4\pi r} - \hat{A}\left(\frac{x_2}{r_i}\right)\frac{i\omega e^{ikr_i}}{4\pi r_i} \tag{3.3}$$

In the above equation, $\hat{A}$ is the arbitrary complex amplitude of the dipole. For some frequencies, the image dipole may provide constructive interference at the observer, and for others, it may provide deconstructive interference. Therefore, it is useful to plot the ratio of the signal from the dipole-image combination to the single dipole by plotting the relationship:

$$\Delta dB = 10 \log\left(\frac{\left|\hat{p}_{w/image}\right|^2}{\left|\hat{p}_{single}\right|^2}\right) \tag{3.4}$$

where $\hat{p}_{single}$ is computed from the first term in Equation (3.3). This relation is plotted across the trailing edge noise frequency range in Figure 3.12 for the upstream and downstream ends of the microphone arc.

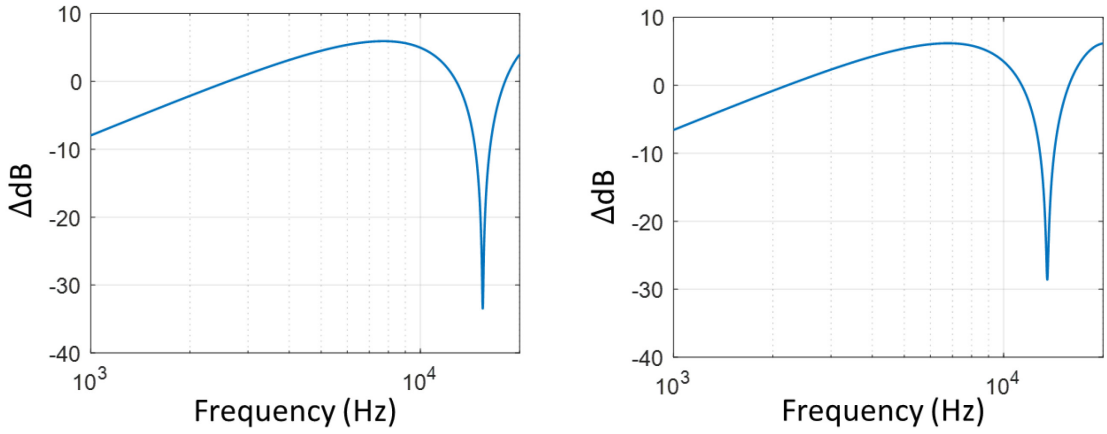

a) Mic 1 **b) Mic 4**

Figure 3.12, Change in far field sound pressure level due to image in wall effects.

From Figure 3.12, it can be seen that the upstream microphone will see full cancelation at 15460 Hz and the overhead microphone at 13560 Hz; conversely, the upstream microphone predicts a peak of +5.92 dB at 7720 Hz, and the overhead microphone's peak occurs with +6.2 dB at 6770 Hz. It can also be seen that less attenuation is expected at the lower frequency end of the trailing edge noise range for the overhead microphone, which may also contribute to the relative lack of directivity effects observed in the far field data.

Comparing the curve in Figure 3.12 to the signal-to-noise plot in Figure 3.6, it becomes clear that there is a region near 14.3 kHz at which the signal-to-noise ratio becomes essentially zero. However, the location of this trough shifts to lower frequency, about 12 kHz, for the upstream microphone, as opposed to the expected increase to 15460 Hz. Nonetheless, this is likely the "fingerprint" of the predicted attenuation effects of the image in the wall. Notably, the attenuation seems to be much stronger for the downstream microphones, and hardly noticeable upstream. This is because the image in the wall analysis presented above does not account for the Green's function of the trailing edge geometry. Therefore, the undercut trailing edge may be "shielding" the upstream microphones from being affected by the acoustic image, by virtue of blocking the acoustic line of sight.

As can be seen from Figure 3.10, the resonance effects are dominant in modifying the shape of the trailing edge noise spectrum in the form of spectral humps. The wall image effects decrease the observed noise below 2500 Hz at Mic 1 and 2200 Hz at Mic 4 and increase it above those frequencies up to 13 kHz at Mic 1 and 11.3 kHz at Mic 4. Its effect is expected to be most noticeable at 15000 Hz where deconstructive interference may be an issue. It is now concluded that the measured noise shown in Figure 3.7 is indeed produced by the trailing edge, although the spectral shape has been modified by the experimental arrangement.

3.3 Surface Pressure and Predictions of Trailing Edge Noise for Straight Trailing Edge

Now that the flow has been characterized and the trailing edge noise from the straight trailing edge has been identified, the wavenumber filter can be applied to the measured surface pressure spectrum and the noise from the mock trailing edge can be compared to predictions derived from experimental and theoretical analyses of noise from flat-plate and airfoil geometries.

3.3.1 Wavenumber Filtered Spectrum

As detailed in Section 2.7, the arrangement of surface pressure microphones on the straight trailing edge approximates a wavenumber filter for $k_3 \approx 0$. The spurious response spikes of

the array can be seen in Figure 2.35. The important takeaway from this figure is that while the majority of the content captured by the wavenumber filter is at $k_3 = 0$, enough energy is present at other wavenumbers that this approximation is far from perfect.

As stated, the time series data of each surface pressure microphone is added up and divided by the total number of microphones to produce a single summed time signal. The original voltage signal is calibrated to a pressure value by using the flat response sensitivity shown in Figure 2.14, which can introduce error at higher frequencies in the filtered spectrum. The Fourier transform of this time signal roughly approximates the $k_3 = 0$ frequency spectrum. The result of performing this computation on the time data is displayed in Figure 3.13. Also shown are the single-point spectra of each of the individual surface pressure microphones for level comparison.

It can be seen that in general, the single-point spectra of the surface pressure microphones are around 25 dB higher than the filtered signal. This is to be expected, as the single-point spectra represent the wavenumber-frequency wall pressure spectrum integrated over all k_1 and k_3, and the filtered signal approximates a single slice of that spectrum, at $k_3 = 0$. The magnitude of the filtered spectrum is closer to the single point spectra at frequencies below 100 Hz, around 20 dB, which speaks to the general effectiveness of the wavenumber filter at rejecting high wavenumber content.

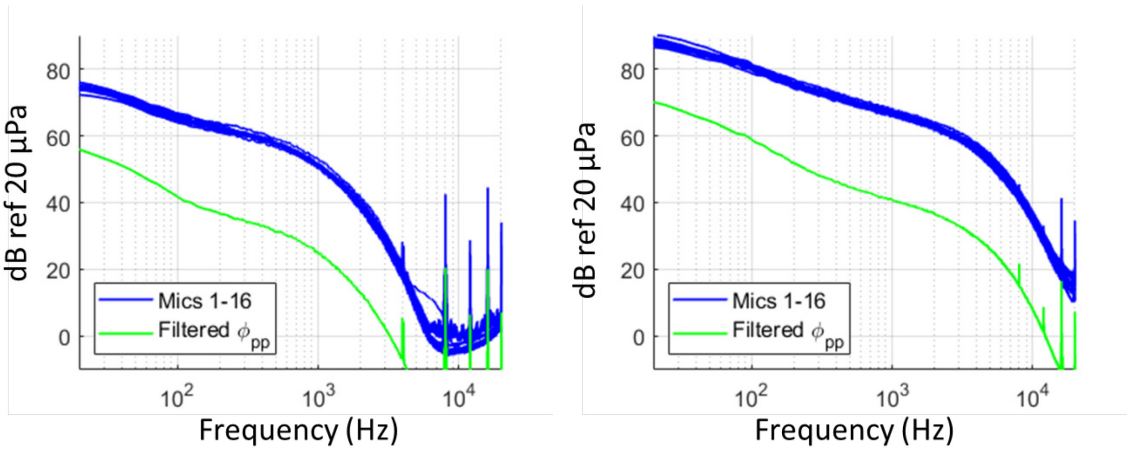

a) $U_j = 20$ m/s **b) $U_j = 40$ m/s**

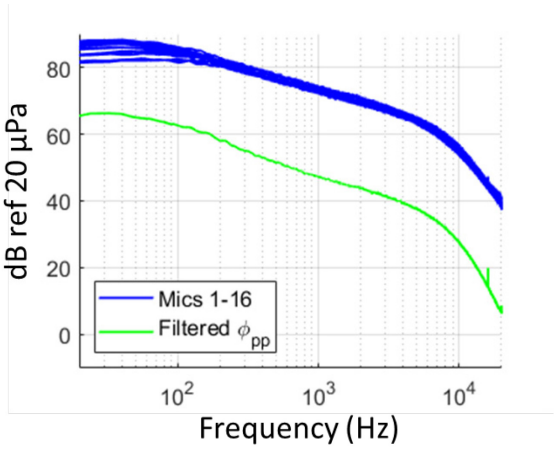

c) $U_j = 60$ m/s

Figure 3.13, Filtered surface pressure spectrum compared to single-point spectra of microphones.

3.3.2 Potential Unsteady Loading

In order to use the single boundary layer form of Amiet's equation with our measured surface pressure spectrum, it must be proven that what is being measured atop the surface is the only significant contributing pressure fluctuation field; in other words, that any pressures fluctuating between the trailing edge and the wall are insignificant relative to the top surface loading. To this end, a single Knowles microphone was placed directly beneath the trailing edge in the plate, 12.7 mm below the edge; this arrangement is pictured in Figure 3.14. The

resulting pressure field measured is shown in Figure 3.15 and shown alongside the surface pressure spectrum on the top surface upstream of the trailing edge for comparison.

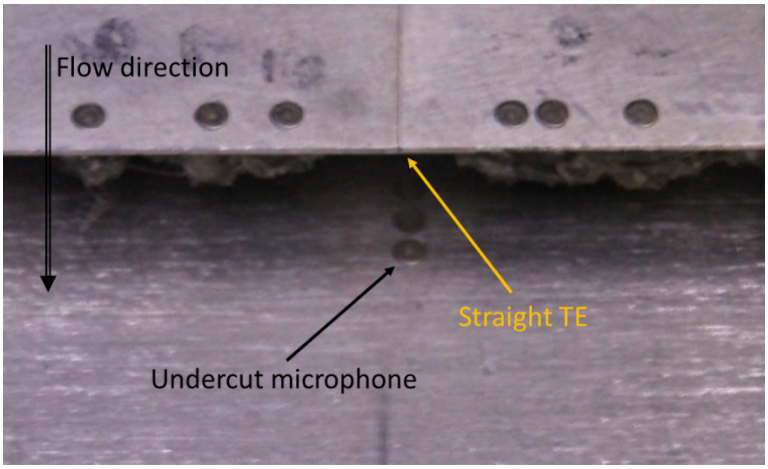

Figure 3.14, Undercut microphone mounted in wall jet.

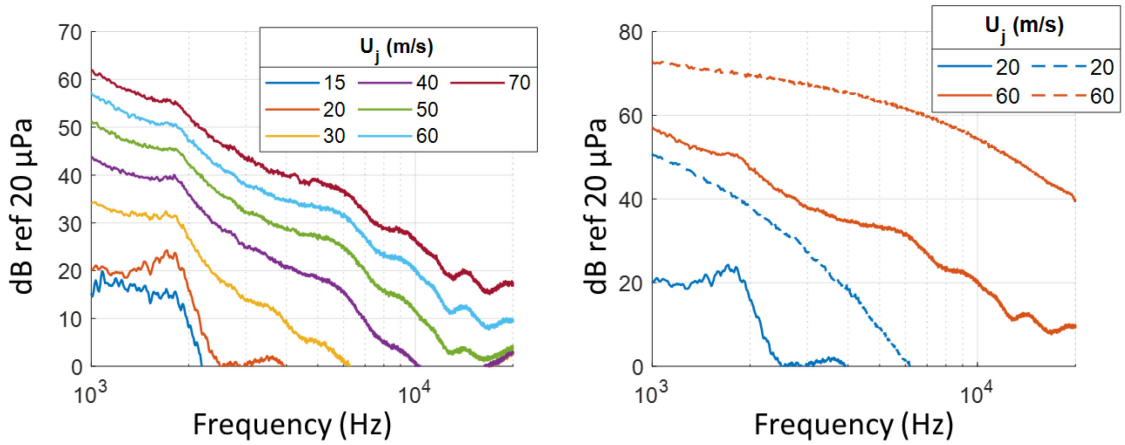

Figure 3.15, Pressure spectrum beneath trailing edge as measured by microphone embedded underneath. Dashed lines are surface pressure data from Mic 8 on the top side (flow side) of the trailing edge.

It is clear that the pressure field beneath the trailing edge is several orders of magnitude smaller than that of the pressure field upstream of the edge, and therefore it is concluded that there are no significant unsteady loading effects from pressure fluctuations on the underside of the trailing edge that must be accounted for when Amiet' prediction method assuming a

single-sided flow. Also notable are the resonant peaks that were seen earlier, though these appear at slightly lower frequencies than those which appeared in the far field spectra; here, the peaks appear at 1800 Hz, 6000 Hz, 9 kHz, 14 kHz, and 19 kHz. These are visible here because the pressure fluctuations at the resonant frequencies are weak enough underneath the edge to not drown out the resonant acoustic pressure fluctuations, as opposed to on top of the plate, further supporting the conclusion that the boundary layer at the edge can be considered single-sided.

3.3.3 Single-Point Models of Surface Pressure Spectra

With the measured flow parameters as reported in Section 3.1, the prediction models of Chase, Goody, and Graham can be computed. The single-point spectra given by these models are shown in Figure 3.16, using the measured values of U_c. In the case of the Chase spectrum, the model is integrated in k_1 and k_3.

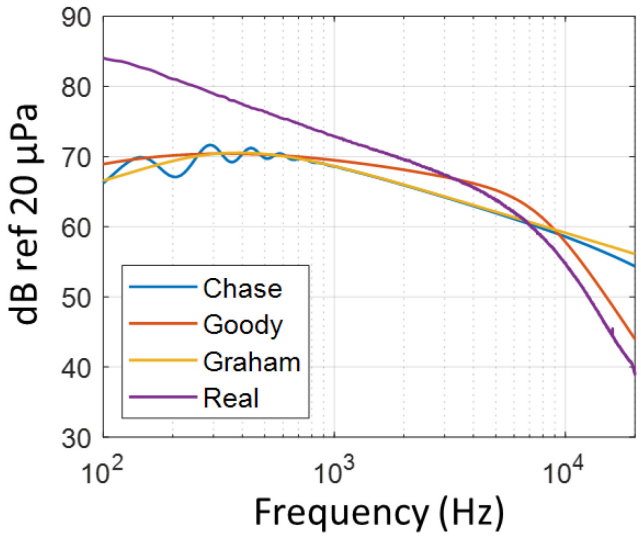

Figure 3.16, Single-sided surface pressure frequency spectra model comparison. The full Chase wavenumber-frequency wall pressure spectrum model is numerically integrated in k_1 and k_3, and Real is the averaged measured surface pressure spectrum.

It is immediately obvious that the surface pressure spectrum models are inadequate for predicting the measured spectrum of the wall jet boundary layer below 1 kHz. The difference between the modeled spectra and the real spectrum becomes larger as the frequency is lowered; a difference of around 3 dB is present between the real and predicted spectra at 1000 Hz, and it gradually increases to a difference of around 15 dB at 30 Hz. The large difference at these frequencies exists because the models are designed for a conventional zero-pressure-gradient turbulent boundary layer. A wall jet boundary layer includes a large mixing layer, which provides more low-frequency fluctuations than a conventional turbulent boundary layer. Above 1 kHz, the slope of the Chase and Graham single point spectra matches that of the measured spectrum, but the curves are 4 dB lower. This trend continues up to 3 kHz, when the high-frequency drop off region of the turbulent boundary layer spectrum is reached for the measured spectrum, and at 7 kHz the measured spectrum drops below the Chase model as the Chase spectrum reaches its known region of overprediction [20]. The Goody spectrum separates from the Chase spectrum at about 700 Hz, and slowly approaches the measured spectrum before crossing over at 3300 Hz and overpredicting the spectrum by about 6 dB at higher frequencies. Goody's model explicitly corrected the high-frequency region to decay as ω^{-5} [20], but still tends to overpredict the high frequency noise in this case. This could be due to the total turbulent energy being more contained in the larger eddies of the mixing layer. Nonetheless, the models will still be useful as inputs to Amiet's equation to predict the behavior of a single-sided flat plate conventional boundary layer.

The single point spectra must be converted into full wavenumber-frequency wall pressure spectra for use in Amiet's calculation. This is done by assuming the form of the Chase model is correct but adjusting the spectral levels according to the magnitude of the single point spectra. This is done by normalizing the Chase wavenumber-frequency model on the single point spectrum, essentially using the normalized spectrum as a transfer function between the single point spectrum and the full wavenumber-frequency spectrum. The Graham single point spectrum was used as the single point spectrum to normalize the Chase model.

$$\phi_{pp,i}(k_1, k_3, \omega) = \frac{\phi_{pp,Chase}(k_1, k_3, \omega)}{\phi_{pp,Graham}(\omega)} \phi_{pp,i}(\omega) \tag{3.5}$$

Here, $\phi_{pp,i}$ is the wavenumber-frequency spectrum for one of the various single-point measurements. The Chase-form wavenumber-frequency wall pressure spectrum model adjusted to the levels implied by the Goody spectrum is used throughout this section when referring to the Goody spectrum.

3.3.4 Predictions of Trailing Edge Noise Using Amiet's Method

To use Amiet's method, the various wavenumber-frequency surface pressure spectra were integrated over all k_1 and evaluated at $k_3 = 0$ to produce the $\phi_{pp}(0, \omega)$ input to Amiet's method. Using $\phi_{pp}(0, \omega), b, c, c_\infty, U_m, U_c, u_\tau, \beta, \delta, \rho_0$ and ν, the Amiet far field spectra were computed.

A prediction of the wavenumber filter output can be done using Equation (2.14). Applying the computed wavenumber filter response to a model of the surface pressure spectrum produces a prediction of the wavenumber filter's response to a surface pressure field. Equation (2.14) is repeated here for convenience:

$$\phi_m(\omega) = \iint |S(k_1, k_3, \omega)|^2 \phi(k_1, k_3, \omega) dk_1 dk_3 \tag{2.14}$$

The real filtered spectrum, which is computed by summing the time series data and dividing by the number of microphones, is in units of dB per angular frequency. A slice through the wavenumber-frequency spectrum at $k_3 = 0$ is essentially replacing S with a delta function at $k_3 = 0$ and has units of dB per angular frequency per wavenumber. Therefore, in order to compare the filter response to a slice through the wavenumber-frequency spectrum at $k_3 = 0$, the filtered response of the measured data and the Chase and Goody spectra must be divided by the width of the main response lobe of $|A(k_3)|^2$ to add units of per wavenumber to ϕ_m.

Figure 3.17 shows the Chase and Goody spectra with the filter function computed using Equation (2.14) and the real filtered spectrum compared to the Goody spectrum integrated in k_1 and evaluated at $k_3 = 0$.

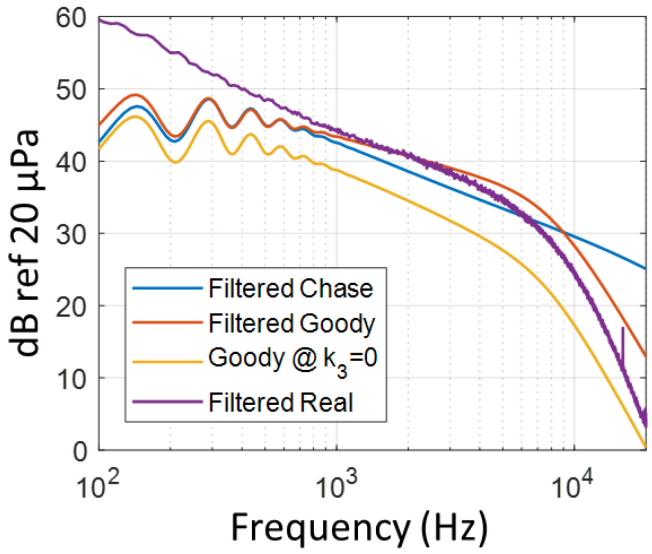

Figure 3.17, Comparison of $\phi_m(\omega)$ implied by Goody and Chase models and real signal with wavenumber filter applied. $\phi_m(\omega)$ is double-sided in this figure.

Comparing the wavenumber filtered Goody spectrum to the Goody spectrum evaluated at $k_3 = 0$ directly, it can be seen that the wavenumber filtered spectrum is greater than the $k_3 = 0$ by about 6 dB at 100 Hz. This difference gradually increases to about 14 dB at 10 kHz. At 100 Hz, the filtered Goody and Chase models underrepresent the wavenumber-filtered spectrum by about 15 dB. The difference slowly decreases until around 800 Hz, when the filtered models overestimate the filtered spectrum by about 2 dB. The level of the filtered Chase spectrum is within 2 dB of the real filtered spectrum up to 8 kHz, after which it begins to increasingly differ from the real spectrum. After a gradual crossover occurs between the filtered Goody spectrum and the filtered real spectrum at about 1.8 kHz, the difference between the filtered Goody spectrum and the filtered real spectrum gradually increases from about 2 dB at 6 kHz to about 10 dB at 20 kHz. The high frequency drop-off in the filtered

spectrum occurs at a somewhat lower frequency in the measured data than that of the Goody model. The Goody spectrum evaluated at $k_3 = 0$ underrepresents the filtered measured spectrum by about 6 dB at 1 kHz, and this difference increases to about 7 dB at 3 kHz before decreasing as higher frequencies are approached. Though the filter is not perfect, the similar values for high-frequency drop-offs between the filtered Goody, $k_3 = 0$ Goody, and real filtered spectra is an encouraging sign. It should also be noted that the single point Goody spectrum in Figure 3.16 crosses the real single point spectrum at $f = 1.8$ kHz, while in Figure 3.17 the filtered Goody spectrum crosses the real filtered spectrum at $f = 500$ Hz. This suggests that the spanwise form of the Chase model may not be a very accurate representation of a wall jet boundary layer. The relatively increased levels of the Chase model after applying the filter implies that the width of the k_3 convective ridge modeled by Chase is too broad to accurately represent the spectrum of a wall jet boundary layer.

Figure 3.18 shows the result of using Amiet's method to predict the trailing edge noise using the Chase wavenumber-frequency spectrum, the Goody wavenumber-frequency spectrum using the form of Chase, the measured single-point spectrum using the form of Chase, the wavenumber-filtered spectrum shown in Figure 3.17, the measured background-subtracted far field noise, and the measured single-point spectrum using the form of Chase computed with the U_c estimated by Devenport *et al.* [48]. Each of the inputs assuming the Chase form is integrated in k_1 and evaluated at $k_3 = 0$.

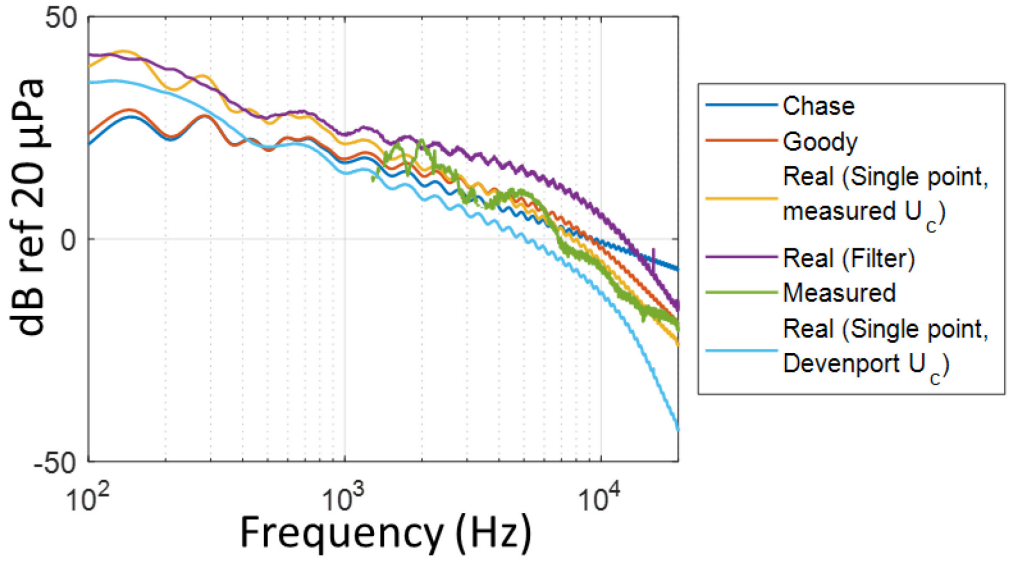

Figure 3.18, Amiet's method predictions of trailing edge noise at Mic 1, $U_j = 60$ m/s.

Figure 3.18 shows that the measured single-point spectrum applied to the Chase model oscillates around the value of the wavenumber-filtered real spectrum when used to predict trailing edge noise using Amiet's method up to about 1000 Hz. These values are around 15 dB higher than the Chase and Goody spectra at 100 Hz; this is because the wall jet boundary layer has much more low frequency content than a traditional boundary layer. At 1000 Hz, the wavenumber-filtered spectrum prediction begins to overpredict the rest of the far field spectra, as well as the measured spectra, by up to 10 dB. This shows the wavenumber filter's inability to adequately reject higher k_3 wavenumber content. Above 1000 Hz, the Goody spectrum prediction stays within 3 dB of the measured single point spectrum prediction, owing to the greater ability of Goody's model to accurately predict the form of the wall pressure spectrum; the Chase model once again fails to taper off at high frequency. The measured single-point prediction using the measured U_c stays within 4 dB of the measured background-subtracted noise over the full region where the background-subtracted noise is measurable; the Devenport *et al.* U_c real single-point curve underpredicts the noise by between 3 and 10 dB up until 12 kHz, at which point it begins to severely underpredict the noise; and the Goody spectrum stays within 6 dB throughout the full frequency range.

Though the Goody spectrum tends to overpredict the high-frequency noise (above 6 kHz), in the region of the first two resonant humps, the Goody and real (measured-U_c) single point predictions tend to predict the background-subtracted noise equally well, to within about 4 dB. Additionally, the measured-U_c real single point spectrum appears to be a better prediction input than the Devenport *et al.* U_c real single point spectrum. This is a promising result, as it shows the potential for the Goody model and measured-U_c single-point spectrum applied to the form of the Chase model to be used for trailing edge noise predictions. Nonetheless, as shown in Figure 3.16 and Figure 3.17, it is likely that there are differences between the wall jet's surface pressure spectrum and the assumed form of the Chase wavenumber-frequency wall pressure spectrum. Additionally, an improved design of the microphone wavenumber filter may improve the results of the prediction using the measured surface pressure spectrum as well.

An examination of the image in the wall effects computed in Section 3.2.3 was also performed. The curve in Figure 3.12 was added to the Amiet prediction of the Goody spectrum, and the result is shown in Figure 3.19.

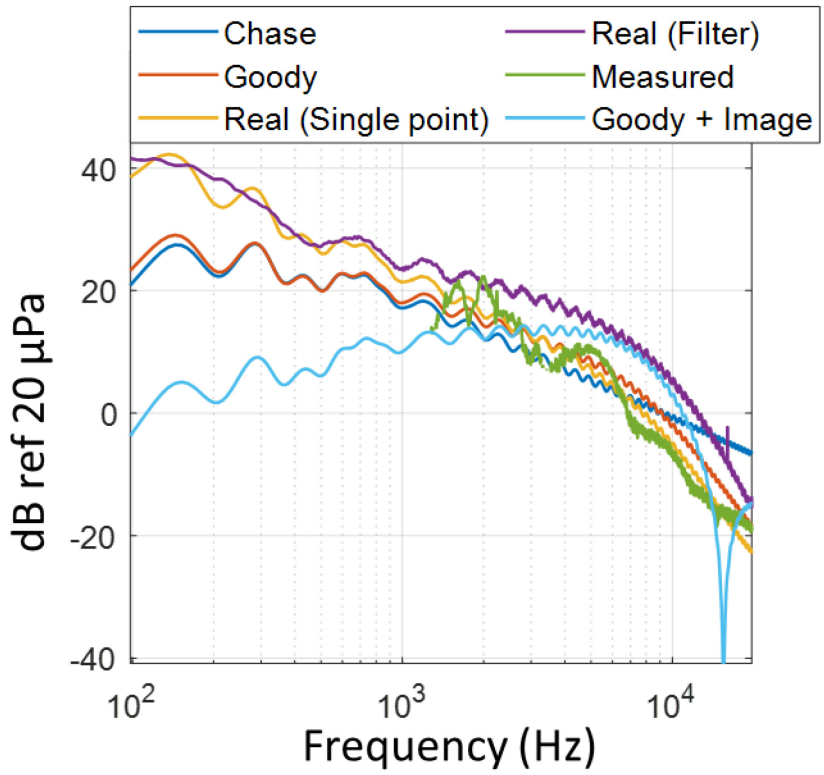

Figure 3.19, Amiet predictions of trailing edge noise at Mic 1 for $U_j = 60$ m/s including image in wall effects.

Figure 3.19 shows that the idealized image in the wall prediction does not provide a good prediction of the characteristics of the actual measured trailing edge noise. This is due to the image in the wall analysis being performed for a dipole in free space, which does not account for the geometry of the edge. The point at which the image in the wall does not affect the prediction, 2700 Hz, also seems to be a point at which the Goody, measured single point, image in the wall, and measured background-subtracted noise all agree, though this is likely to be no more than a coincidence, as there is nothing notable about this frequency in terms of scales.

3.3.5 Brooks-Pope-Marcolini Predictions

In Section 1.3, the Brooks-Pope-Marcolini method of predicting trailing edge noise was discussed. These take the form of Equation (1.15), which sums the contributions from the

pressure- and suction-side boundary layer properties and any additional contribution due to the angle of attack. Since this is a single-sided, zero angle of attack boundary layer flow, only the pressure side contributions need be considered. These are computed using Equation (1.16), which is repeated here for convenience:

$$SPL_p = 10\log\left(\frac{\delta_p^* M^5 L \bar{D}_h}{r_e^2}\right) + A(a_p) + (K_1 - 3) + \Delta K_1 \tag{1.16}$$

δ_p^* and M^5 are known parameters of the flow, L is the span of the edge, and r_e is the position of Mic 1. No shear layer refraction effects need be considered. What remains is to calculate the shape function A and amplitude function K_1. For an airfoil at zero angle of attack, ΔK_1 is zero.

The amplitude function is designed to be symmetric about the point $a_i = 0$, where $a_i = |\log(St_i/St_1)|$, the ratio between the Strouhal number $St_i = f\delta_i^*/U_e$ and the peak Strouhal number $St_1 = 0.02M^{-0.6}$, which comes from a curve fit through BPM's data. A then describes a curve that is interpolated between an upper and lower curve, A_{max} and A_{min}. These curves are described by the following equations:

$$A_{min}(a) = \begin{cases} \sqrt{67.552 - 886.788a^2} - 8.219 & a < 0.204 \\ -32.655a + 3.981 & 0.204 \le a \le 0.244 \\ -142.795a^3 + 103.656a^2 - 57.757a + 6.006 & 0.244 < a \end{cases} \tag{3.6}$$

$$A_{max}(a) = \begin{cases} \sqrt{67.552 - 886.788a^2} - 8.219 & a < 0.13 \\ -15.901a + 1.098 & 0.13 \le a \le 0.321 \\ -4.669a^3 + 3.491a^2 - 16.699a + 1.149 & 0.321 < a \end{cases} \tag{3.7}$$

From these curves, a simple linear interpolation is performed.

$$A(a) = A_{min}(a) + A_R(a_0)\big(A_{max}(a) - A_{min}(a)\big) \tag{3.8}$$

A_R is the interpolation factor, and is computed by:

$$A_R(a_0) = \frac{\left(-20 - A_{min}(a_0)\right)}{A_{max}(a_0) - A_{min}(a_0)} \tag{3.9}$$

where a_0 is dependent on Re_c, the chord-based Reynolds number. In the $U_j = 60$ m/s case, $Re_c = 1.3166\text{x}10^6$, which corresponds to $a_0 = 1.13$.

The amplitude function K_1 is added to the shape function A and is meant to set the level of the overall curve. It is also dependent on Re_c, and in this case takes the value of 128.5. The subtraction of 3 from K_1 separates the pressure-side contribution from the suction-side contribution.

Finally, the directivity factor $\overline{D_h}$ is given by:

$$\overline{D_h}(\theta_e, \phi_e) = \frac{2\sin^2\left(\frac{\theta_e}{2}\right)\sin^2(\phi_e)}{(1 + M\cos\theta_e)[1 + (M - M_c)\cos(\theta_e)]^2} \tag{3.10}$$

The bar over $\overline{D_h}$ indicates that the value is normalized on the noise radiated in the $\phi_e = 90°$, $\theta_e = 90°$ direction. Since there are no shear layer refraction effects, ϕ_e and θ_e are given by the microphone position alone ($\phi = \text{atan}(x_2/x_3)$, $\theta = \text{acos}(x_1/r_e)$). M_c is the convective Mach number, $M_c = U_c/c_0$.

Putting all of these equations together, a curve fit for the predicted 1/3 octave band trailing edge noise spectrum was produced. The BPM prediction for the $U_j = 60$ m/s case is shown in Figure 3.20 as compared to the predictions in Figure 3.18 computed as 1/3 octave band spectra.

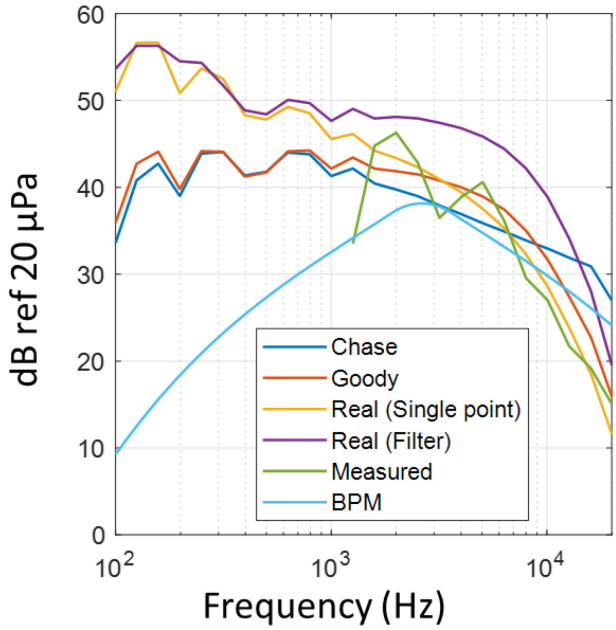

Figure 3.20, 1/3 octave band predicted and measured trailing edge noise at Mic 1, $U_j = 60$ m/s.

In the primary regions of trailing edge noise, above 1200 Hz, the BPM prediction tends to under-predict the measured trailing edge noise by up to 10 dB. However, there are frequency bins, especially between the resonant peaks, where the BPM prediction is quite close to the measured noise, within 1-2 dB. At around 7.2 kHz, the BPM prediction begins to overpredict the noise. Notably, the BPM prediction also predicts far less noise than the theory-based methods at low frequencies, between $f = 100$ Hz and $f = 2500$ Hz. This is because the Brooks-Pope-Marcolini model is derived from measurements on airfoils, not zero-pressure-gradient turbulent boundary layers, and the data that are curve fit by the symmetrical function A exist at higher frequencies; the long decrease at low frequency is thus the result of extrapolating the shape function to a region where it may no longer be valid.

Overall, for the case of $U_j = 60$ m/s, the prediction method that seems to have the best accuracy for the mock trailing edge uses the Goody single point spectrum applied to the normalized Chase wavenumber-frequency spectrum. This wall pressure model is then used

in Amiet's noise prediction method. However, it must be noted that all of these methods are designed for traditional boundary layers and without any resonance or image in the wall effects.

3.4 Straight Trailing Edge Spanwise Coherence

An important measure of the flow over the straight trailing edge that will serve as a comparison point for the serrated trailing edge flow is the coherence along the span, $\gamma(\Delta x_3)$. As the surface pressure field is homogeneous, this can be described solely in terms of the separation distance between any two pairs of microphones. The spanwise coherence for all separation distances on the order of the serration width is shown in Figure 3.21. Gray boxes in the coherence figures indicate the low-frequency region in which the coherence measurement may not be accurate due to the dynamic range limitations of the Knowles microphones, as detailed in Section 2.3.3. The dashed magenta lines representing coherence measured between two B&K microphones are excluded from this limitation.

It can be seen from Figure 3.21 that, as expected, the spanwise coherence at low frequencies is much higher than that at high frequencies, and as the flow speed increases the peak coherence shifts to higher frequency. Additionally, the trend of coherence decreasing with increasing separation distance is clear and matches expectations. Note that the decreased coherence at frequencies below 96 Hz for b) and below 560 Hz for c) is not real, as shown by the B&K data in Figure 2.17.

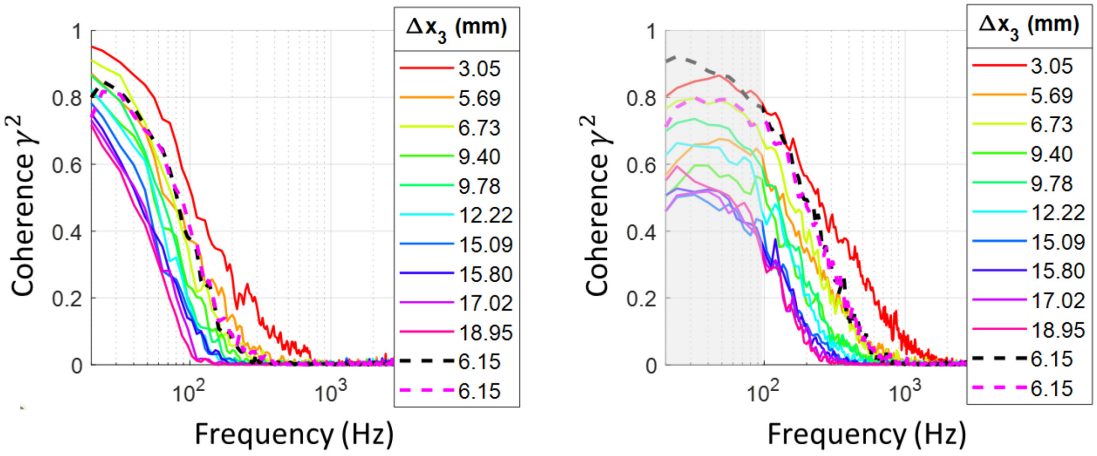

a) $U_j = 20$ m/s **b) $U_j = 40$ m/s**

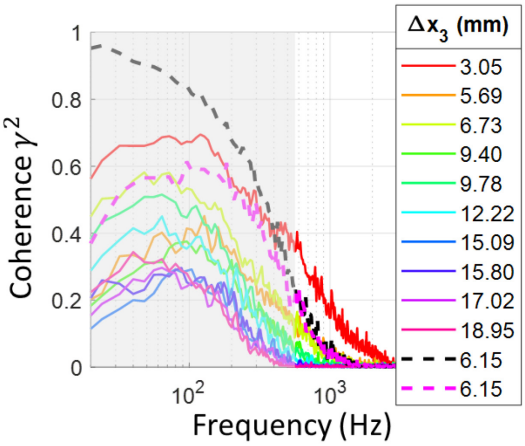

c) $U_j = 60$ m/s

Figure 3.21, Spanwise coherence between surface pressure microphones on straight trailing edge. Dashed lines are data from flat plate measurements, with black representing the B&K-B&K pair and magenta representing the B&K-Knowles pair.

The spanwise coherence length scale is calculated similarly to the streamwise coherence length scale, using spanwise microphone pairs instead of streamwise. Using the B&K-B&K data from Figure 2.17, the spanwise coherence length scale was computed, and is shown in Figure 3.22. As before, the coherence length is compared to the serration length; additionally, the smallest spanwise separation distance between microphone pairs on the straight trailing edge, 3.05 mm, is marked for comparison.

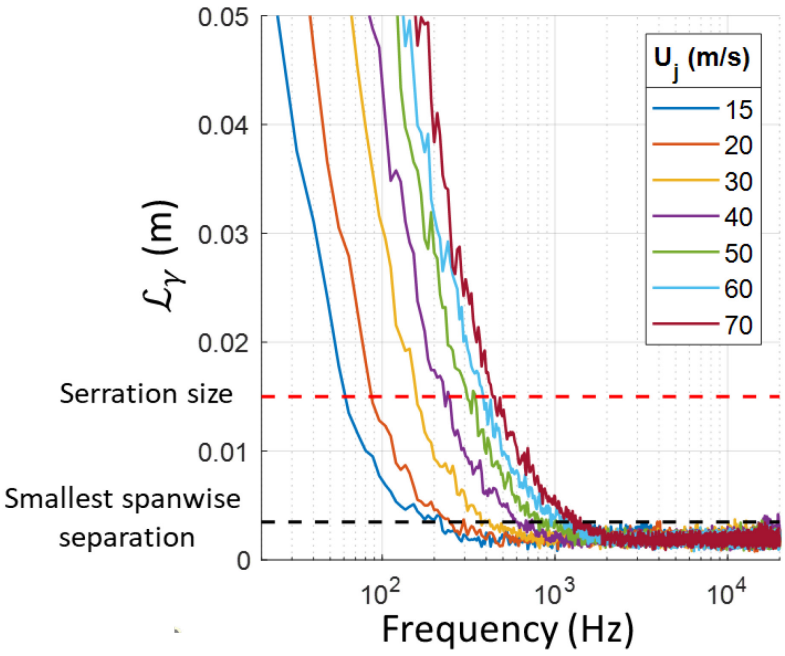

Figure 3.22, Spanwise coherence decay length.

Figure 3.22 shows that the spanwise coherence decay length is much smaller than the streamwise decay length, as expected. The cutoff frequency below which the spanwise coherence length scale is the size of the trailing edge serrations is 60 Hz at the lowest flow speed and 440 Hz at the highest flow speed. Additionally, the spanwise coherence decay length is less than the smallest separation distance at all speeds above 1400 Hz.

3.5 Far Field Noise from Serrated Trailing Edge

The background-subtracted far field noise produced by the serrated edge is examined here. These data were computed in the same way as those for the straight trailing edge in Section 3.2. Figure 3.23 shows the background-subtracted trailing edge noise from the serrated trailing edge corrected to a distance of $|\vec{r}| = 1$ m using the inverse-square law.

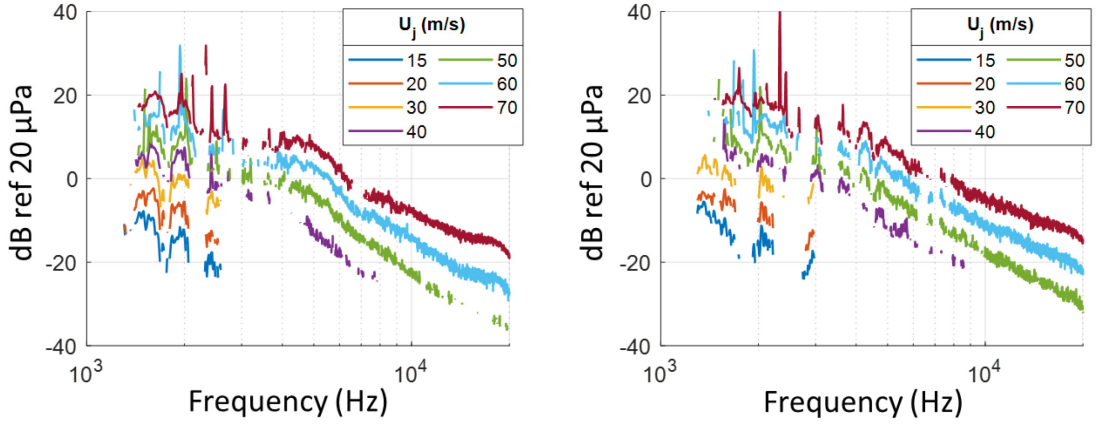

a) Mic 1 **b) Mic 4**

Figure 3.23, Background-subtracted trailing edge noise from serrated trailing edge.

No significant noise was measured below 1 kHz at any nozzle exit velocity. The noise increases with speed and the measurable noise at 70 m/s and a frequency of 1600 Hz is 20 dB. This is a significant reduction from the value for the straight trailing edge, 23 dB. Additionally, the constant-frequency humps still appear upstream at Mic 1, and at the same frequency ranges as those observed in the straight trailing edge spectra. However, they are of greatly reduced magnitude. This suggests that the irregular shape of the serrations reduces some of the resonance effects. To further examine this effect, the serrated trailing edge's noise is compared directly to the straight edge's noise for $U_j = 50$ m/s and 70 m/s in Figure 3.24.

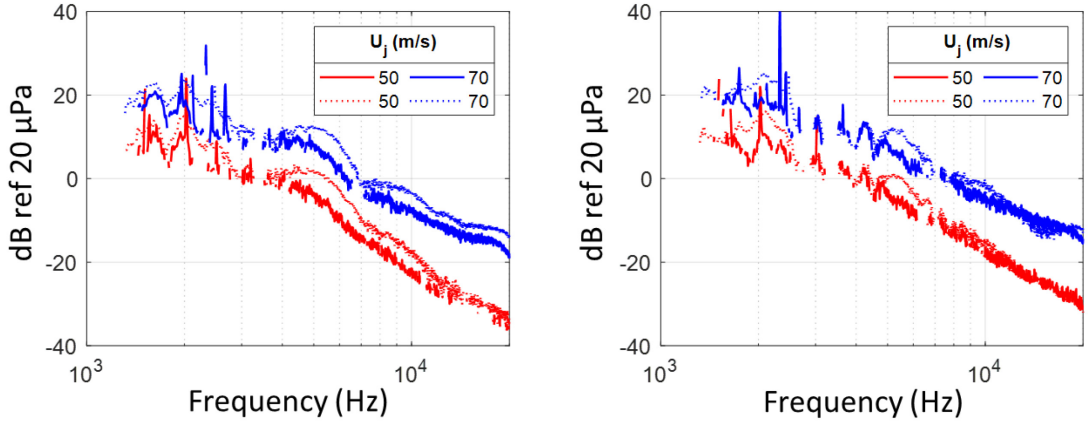

a) Mic 1 **b) Mic 4**

Figure 3.24, Comparison between distance-corrected background-subtracted trailing edge noise from serrated trailing edge and straight trailing edge. Solid lines are serrated edge, dotted lines are straight edge.

The serrated edge is much more effective at reducing far field noise radiated upstream, by about 6 dB in the ~2 kHz hump, 7 dB in the ~6 kHz hump, and 5 dB up to 10000 Hz. In the regions without resonance effects, the noise reduction is reduced to about 3-3.5 dB. For the overhead microphone, the reduction is similar in the region of the resonant humps, but the humps are narrower and the frequency range over which significant reduction is attained is much smaller. In the region outside the spectral humps, the reduction averages approximately 2 dB. Previous experiments have shown that the noise reduction from a serrated trailing edge is often on the order of 2-4 dB [5,34,36]. It is interesting to note that despite the relative thickness of the serrations used in this experiment, 2.38 mm, and the one-sided flow, as opposed to two-sided flow used in previous experiments, the noise reduction is still on the order of previous experimental results using thinner serrations.

3.6 Measurements of Surface Pressure Autospectra on Serrations

In this section, the differences between the measured surface pressure autospectra on the serrated trailing edge and that on the straight trailing edge will be presented and discussed.

3.6.1 Positional Comparisons

The local coordinates of each microphone are tabulated in Table 2.7. These positions are used to locate microphones that are in similar positions relative to the serration they are embedded in. The local positions of each microphone are shown in Figure 3.25.

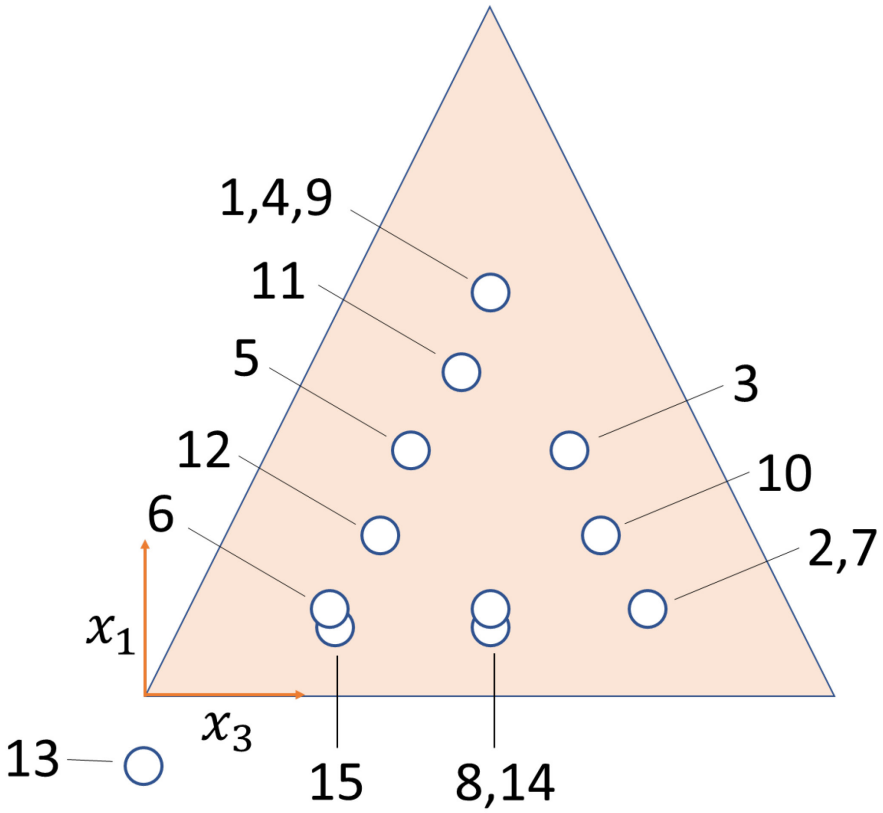

Figure 3.25, Local positions of surface pressure microphones visualized on a single serration.

The sizes of the holes in Figure 3.25 represent the size of the microphone pinholes. Microphones 14 and 15 are slightly upstream of microphones 8 and 6, about 0.4 mm, but are included in the x_1 category of 6, 2, and 7 for comparison. There are thus five x_1 positions with multiple microphone measurements each. The autospectra of the microphones at each of the x_1 positions will be compared to establish whether or not the flow is uniform across the serration. These microphone sets are 1-4-9, 3-5, 10-12, 2-6-7-8, and 14-15.

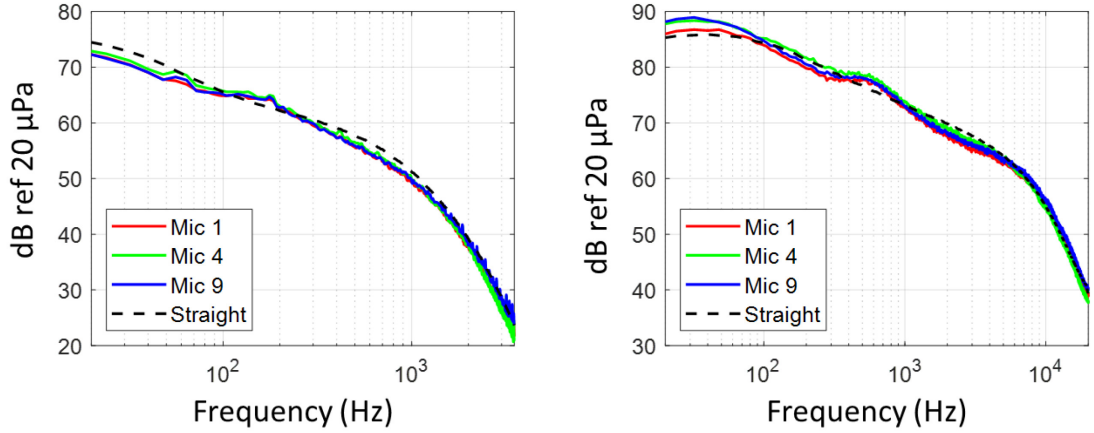
dB ref 20 µPa
Frequency (Hz)
Mic 1
Mic 4
Mic 9
Straight

a)

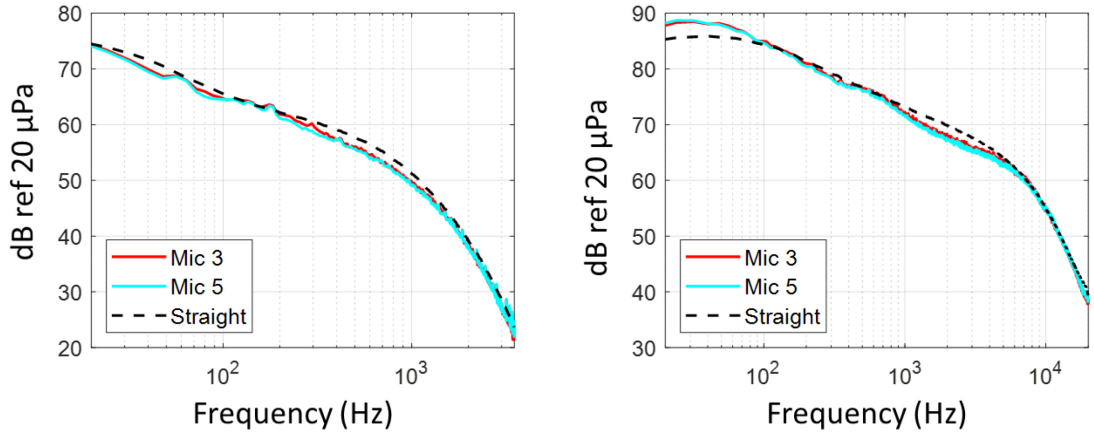
dB ref 20 µPa
Frequency (Hz)
Mic 3
Mic 5
Straight

b)

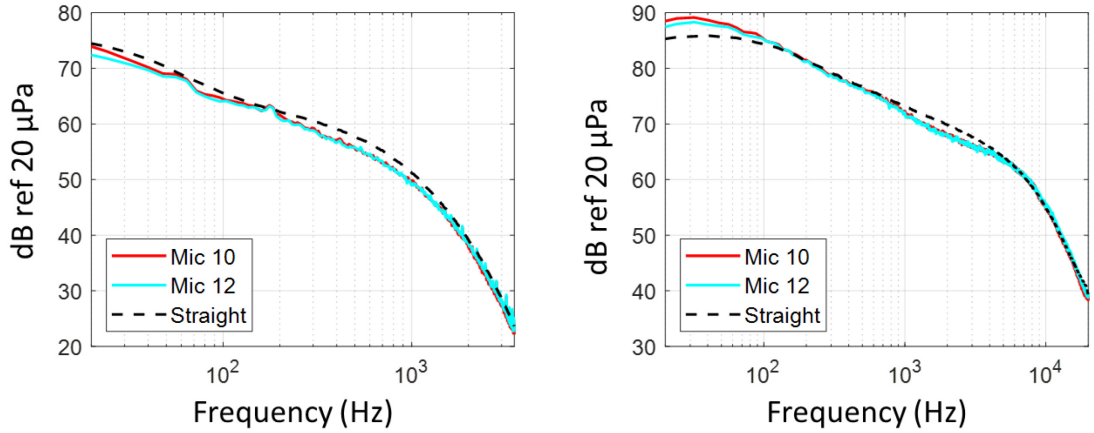
dB ref 20 µPa
Frequency (Hz)
Mic 10
Mic 12
Straight

c)

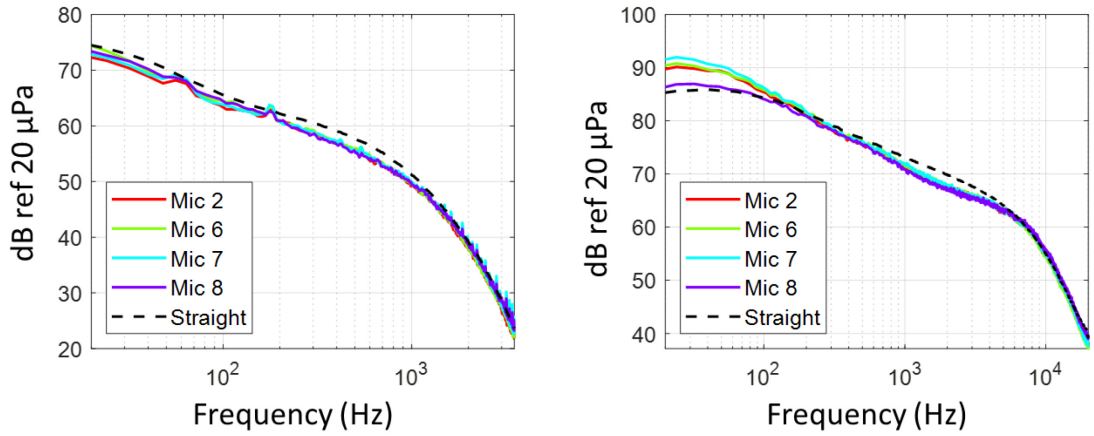

d)

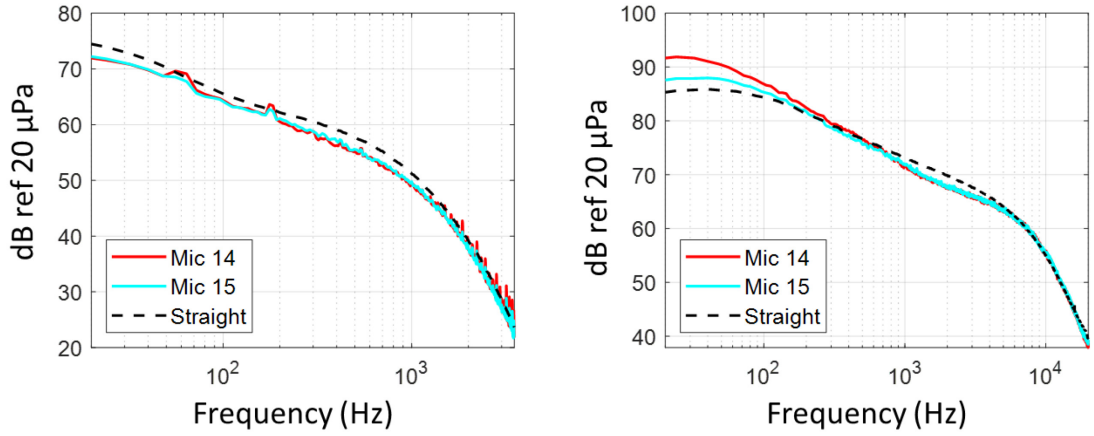

e)

Figure 3.26, Streamwise microphone similarity comparisons with averaged straight trailing edge autospectrum. Left column is measurements with $U_j = 20$ m/s, right column is $U_j = 60$ m/s.

The results of comparing the autospectra of microphone pairs at similar x_1 positions are shown in Figure 3.26, and comparisons are also made to the averaged autospectrum of the straight trailing edge surface pressure microphones. Each plot shows good agreement between the microphone pairs through the full valid range of the Knowles microphones ($f \leq$ 5500 Hz for 20 m/s due to spatial resolution, $f \geq 176$ Hz for 60 m/s due to clipping), with any discrepancy within the uncertainty of the microphones. Of note are the low-frequency

spikes in the Knowles data that appear at $f = 60$ Hz and 180 Hz in the 20 m/s spectra. These appear to be electrical noise, as they do not correspond to any hydrodynamic or acoustic length scale on the order of the serration geometry. Another notable feature is the broadband hump that appears in Figure 3.26a at 60 m/s, the microphones position closest to the tip, between $f = 300$ Hz and $f = 1500$ Hz. This peak is 4 dB above the theoretical straight, collinear line expected to connect the region below 300 Hz and the region above 1500 Hz similarly to the flat plate wall pressure spectrum and straight edge wall pressure spectrum shown in Figure 3.26 for comparison.

3.6.2 Contour Plots of Surface Pressure on Serrations

Ragni *et al.* [62] used overhead PIV imagery to examine the pressure field very near a serrated trailing edge. One result they produced was a contour plot of the evolution of the surface pressure autospectrum along the serrated edge, which showed a clear and significant reduction in the strength of fluctuations along the serration and near the edge. Using the results in Section 3.6.1, the surface pressure field can be assumed to be symmetric about the centerline of the serration, another result obtained by Ragni *et al.* Using this justification, the pressure spectrum at each x_1 location shared by two or more microphones was averaged, and for x_1 locations with a single microphone, the spectrum was duplicated on the opposite side of the centerline. This results in an area of observation in the center of the serration that, while smaller than that of Ragni *et al.*, should give a good understanding of the evolution of the surface pressure field within this region.

Since the direct surface pressure measurements were only available around the perimeter of the triangle, the surface pressure field within the triangle was estimated using 2-D linear interpolation. The surface pressure field at frequencies corresponding to characteristic scales of $2h$, $3h$, $4h$, and $6h$ (1.5, 2.25, 3, 4.5 cm) are shown at $U_j = 20$ m/s and 60 m/s in Figure 3.27; these scales were computed using the measured convection velocities ($f = U_c/L$). The frequencies corresponding to each length scale are given in Table 3.2.

Table 3.2, Frequency bins corresponding to contour plot length scales.

Scale	$f(U_j = 20$ m/s)	$f(U_j = 60$ m/s)	$k_1 h$
$2h$	336 Hz	1210 Hz	3.14
$3h$	224 Hz	807 Hz	2.09
$4h$	168 Hz	605 Hz	1.57
$6h$	112 Hz	403 Hz	1.05

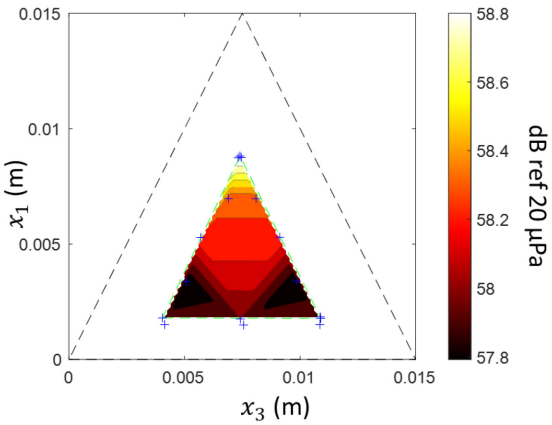

a) $L = 2h, U_j = 20$ m/s

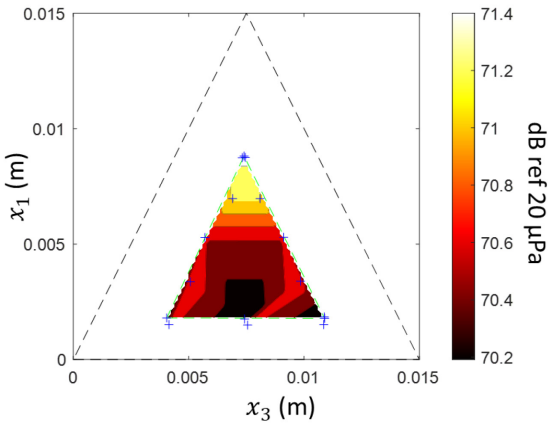

b) $L = 2h, U_j = 60$ m/s

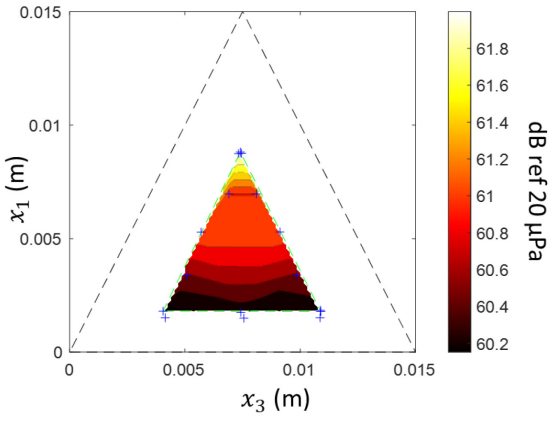

c) $L = 3h, U_j = 20$ m/s

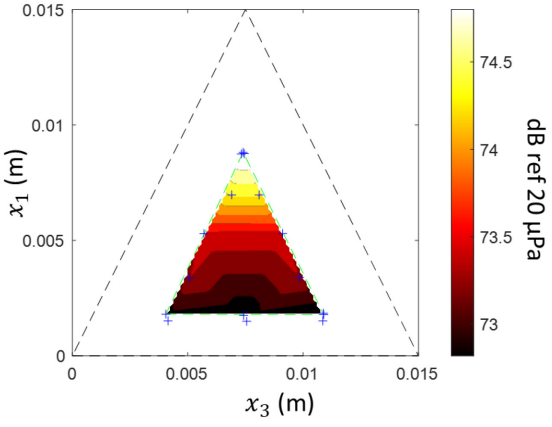

d) $L = 3h, U_j = 60$ m/s

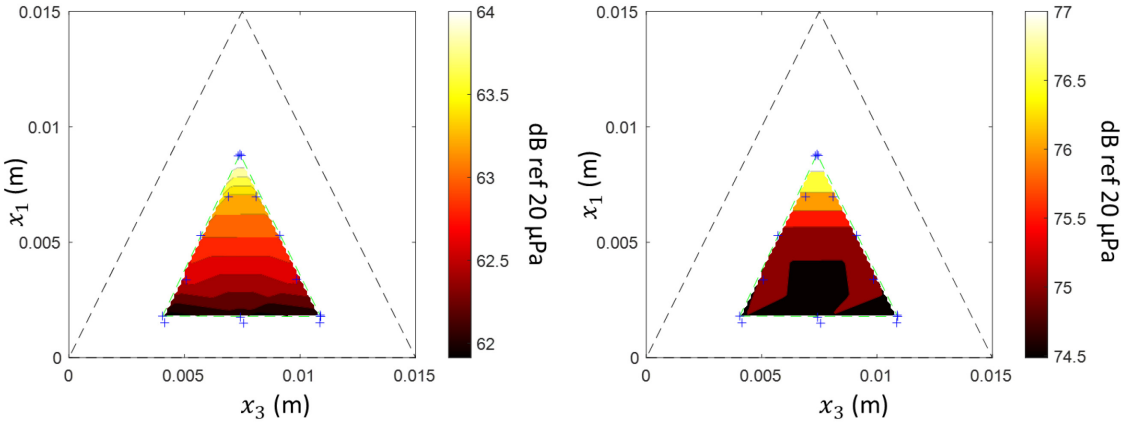

e) $L = 4h, U_j = 20$ m/s **f) $L = 4h, U_j = 60$ m/s**

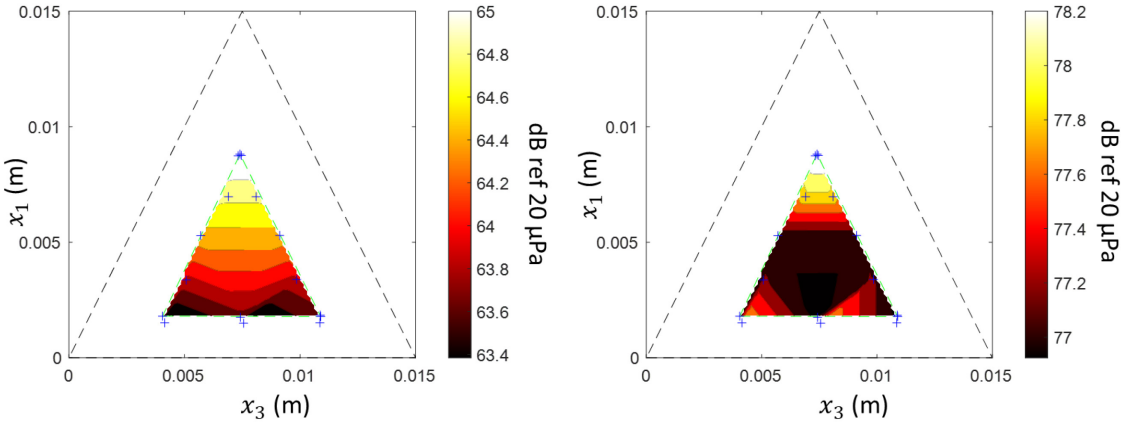

g) $L = 6h, U_j = 20$ m/s **h) $L = 6h, U_j = 60$ m/s**

Figure 3.27, Contour plots of surface pressure autospectra on serrations. Black triangle denotes the full serration size, green triangle denotes the interpolated region, and blue markers denote microphone locations.

Figure 3.27 shows that over this region of the frequency domain, the magnitude of the fluctuations increases by up to 2 dB at $L = 3h$ and $L = 4h$, and up to 1 dB at $L = 2h$, from the root to the tip of the interpolated region. The trend observed here agrees with the measurements of Gruber [34] and Chong and Vathylakis [63], who observed this trend on much larger serrations using remote microphone probes in a one-sided conventional boundary layer flow. However, it contrasts the results of Avallone *et al.* [64] and Ragni *et al.*

[62], who observed the pressure fluctuations decreasing in magnitude along the serration by about 3 dB. Avallone *et al.* performed their experiments on a NACA 0018 airfoil with two-sided flow, and used indirect methods to obtain the surface pressure, including Lattice-Boltzmann computational fluid dynamics and tomographic PIV, to obtain their surface pressure data. They postulated that the reason for the decreased surface pressure fluctuations near the tip was the result of the two-sided boundary layer gradually thinning and approaching equalized pressure towards the tip. These factors suggest that the difference between the single-sided results and the double-sided results may be simply the experiment geometry itself. There may be fundamental differences in serration behavior between the two configurations that account for the observed differences in spectral levels along the serration, and single-sided flat plate flows may not be sufficient to determine the performance and behavior of serrations on an airfoil. Finally, outside of the presented range of hydrodynamic scales, the fluctuations over the interpolated region do not vary more than the measurement uncertainty of the microphones. This is an unfortunate consequence of the limited region of possible measurement locations on the serrations due to the physical size of the instrumentation.

3.7 Measurements of Coherence on Serrations

The wide range of microphone locations over the serration allows for the computation of coherence across various regions of the serrated edge. Specifically, the coherences across the root, across the serration, and along the serrated edge were calculated and compared to the coherence of microphone pairs with similar separation distance along the straight trailing edge. In the following section, the line labels in figures denote the separation distance over which the coherence is computed, and grayed out regions indicate a frequency range over which the microphone response is clipped, as shown in Figure 2.18 and listed in Table 2.4 (spanwise coherence) and Section 3.1.1 (streamwise coherence).

3.7.1 Coherence Between Center and Side of Serration

Figure 3.28 shows the measured coherence between microphones 14 and 15, at the center of the serration and towards the edge at the same x_1 location and separated by $\Delta x_3 = 3.40$ mm,

at jet speeds of $U_j = 20$, 40, and 60 m/s. These are compared with the same measurements taken from the straight trailing edge for separation distances of $\Delta x_3 = 3.05$ mm and 5.69 mm. A diagram indicating the approximate position of the microphones on the serration is included with each figure; these diagrams are not to scale.

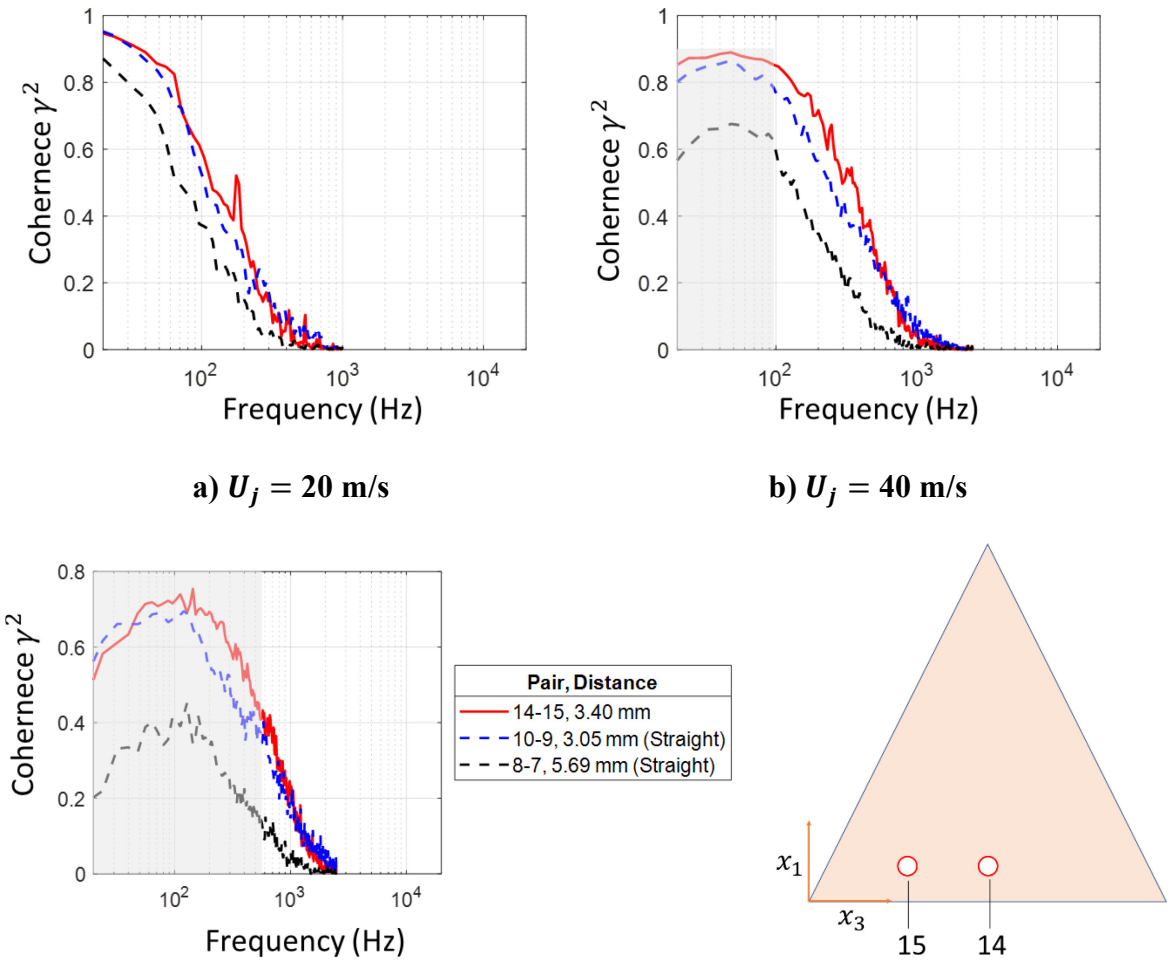

a) $U_j = 20$ m/s

b) $U_j = 40$ m/s

c) $U_j = 60$ m/s

Figure 3.28, Coherence between center and side of serrations.

Figure 3.28 shows that the coherence between the center and side of the serrations is slightly higher than that of the straight trailing edge for frequencies below a crossover frequency, at which the coherence becomes equal to that of the straight trailing edge. For $U_j = 20$, 40, and

60 m/s, this crossover frequency is approximately equal to 250 Hz, 550 Hz, and 900 Hz, respectively. There is very little increase at $U_j = 20$ m/s, but for $U_j = 40$ m/s and 60 m/s, the coherence is increased by 0.1 and 0.1-0.15 in this frequency range, respectively.

3.7.2 Coherence Across Serration Centerline

Next, we examine if the trend observed in Figure 3.28 is also present across the entire serration, using microphone pairs mirrored about the centerline. Microphone pairs 3-5, 10-12, and 2-6 are plotted in Figure 3.29, as well as the same straight trailing edge coherence data and the coherence between centerline and edge discussed in the previous section.

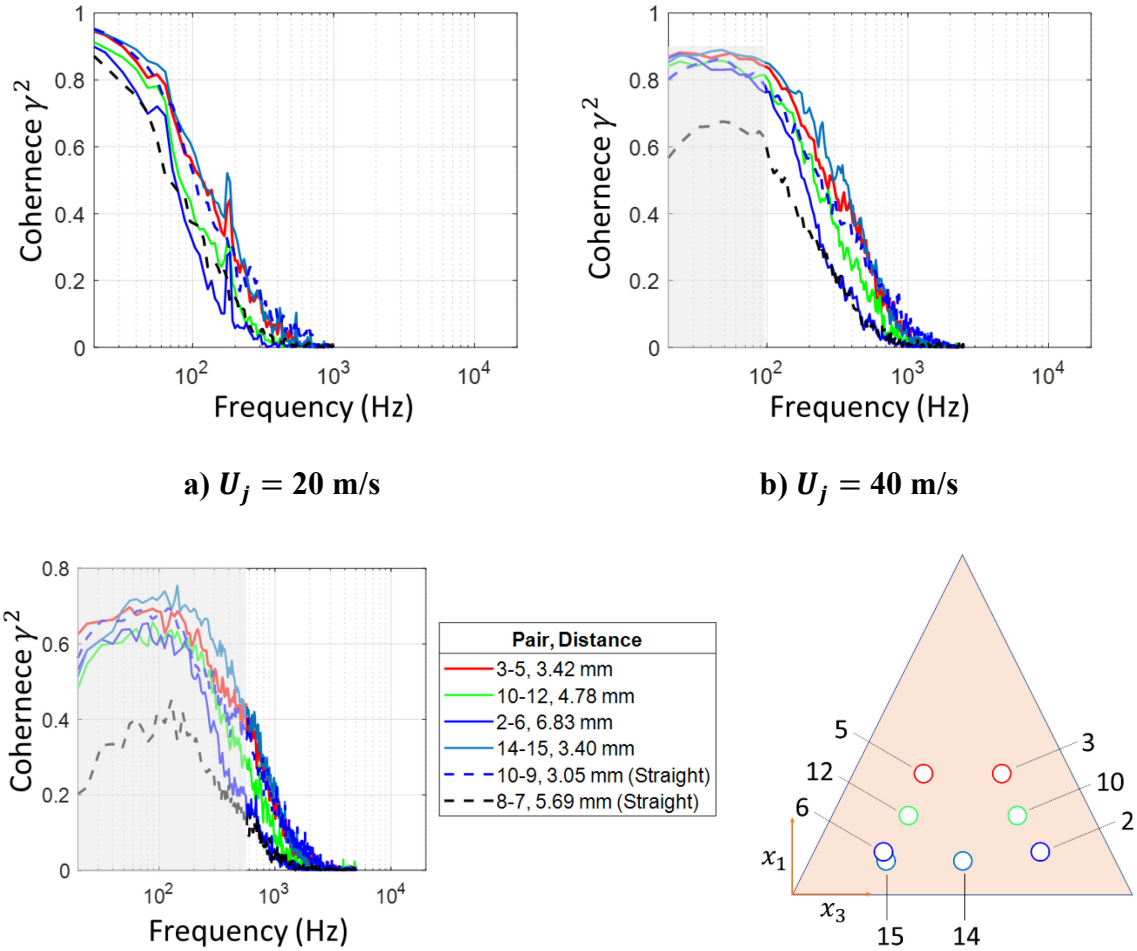

a) $U_j = 20$ m/s **b) $U_j = 40$ m/s**

c) $U_j = 60$ m/s

Figure 3.29, Coherence across centerline of serrations.

There is little discernible difference at $U_j = 20$ m/s between the straight and serrated coherence, owing to the lack of congruity between the microphone spacings. Above 80 Hz, the total spread of the coherence data is 0.3 up until coherence is lost at 1000 Hz. The coherence for the 3.42 mm spacing is roughly the same as the coherence for the 3.05 mm spacing on the straight trailing edge, indicating an increase in coherence for short separation distances at this location. At $U_j = 40$ m/s, the difference in measured coherence between the 3.42 mm separation and 4.78 mm separation begins to increase above 300 Hz; this trend does not continue in the valid frequency range at 60 m/s. There are a few regions where the 3.40 mm center-to-edge coherence (14-15) is greater than the 3.42 mm edge-to-edge coherence (3-5) by up to 0.1, but generally the center-to-edge coherence is only slightly higher than the edge-to-edge coherence. The 3.42 mm coherence stays within 0.1 of the 3.05 mm straight trailing edge coherence and is almost universally higher than the straight edge coherence.

It appears that the spanwise coherence across a single serration is increased compared to a straight trailing edge. That said, the coherence is not just a simple function of the spanwise separation distance but is also a function of the measurement locations themselves, as shown in the comparison of similar separation distances between microphones at different serration relative locations. The spanwise coherence near the center of the serration may be slightly increased above that across the width of the serration closer to the tip.

3.7.3 Coherence Across the Root

Next, the effect of the serration roots on the spanwise coherence is considered. Microphone pairs 6-7 and 1-4, corresponding to cross-root distances of 8.16 mm and 15.05 mm (the serration length scale) compared to straight trailing edge separation distances of 9.40 mm and 15.09 mm in Figure 3.30. Microphones 1 and 4 are located at the serration tip of two adjacent serrations, while microphones 6 and 7 are located nearest the root of two adjacent serrations.

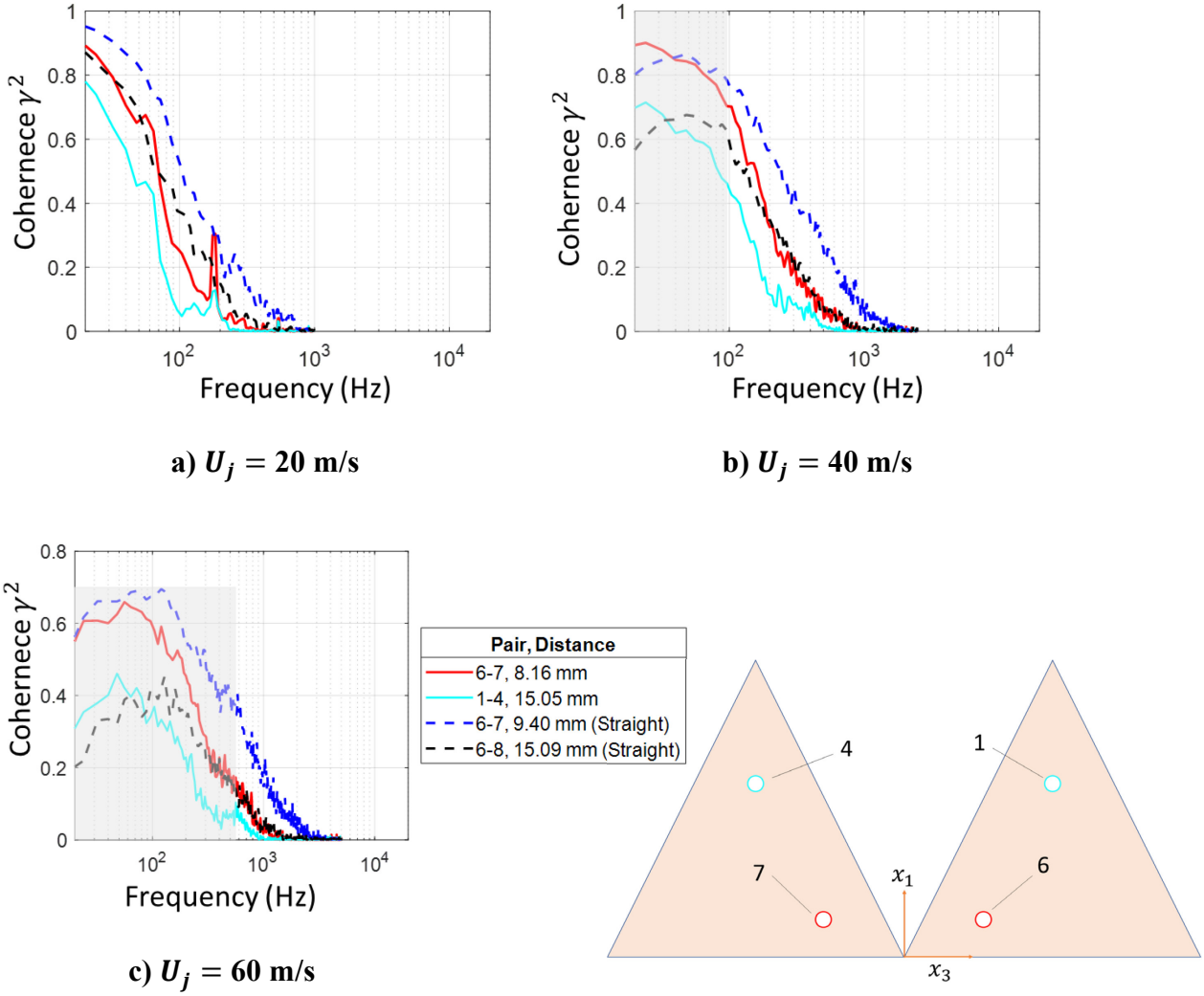

a) $U_j = 20$ m/s

b) $U_j = 40$ m/s

c) $U_j = 60$ m/s

Figure 3.30, Coherence across roots of serrated edge.

Right away it can be seen that the roots are quite effective at reducing coherence along the span. At $U_j = 20$ m/s, the coherence is decreased by up to 0.3 for the tip-to-tip spacing and by 0.2 for the smaller spacing; additionally, the point at which coherence is lost, below $\gamma^2 = 0.1$, is reduced by around 200 Hz for both spacings. At $U_j = 40$ m/s, there is a crossover frequency at which both the small and large spacings across the root have increased coherence, but this is within the invalid region reported in Section 2.3.3 and is unlikely to be a real feature of the flow. Again, the coherence is reduced by up to 0.2 across the full frequency range of coherence, a feature that is again seen for the narrow spacing in the 60

m/s case. However, in this case, the coherence reduction for the wide spacing is less, about 0.1.

These results clearly indicate that the roots significantly affect the flow field across the trailing edge. One possible mechanism of reducing coherence is that observed by the earlier experiments of Gruber *et al.* [33], of flow "channeling" through the roots. Turbulent eddies flowing through this region would be severely distorted compared to eddies that did not encounter a root. The evidence cited for this phenomenon in that experiment, an increase in high-frequency noise due to the small jets the cross-flow creates, does not appear to be present in the trailing edge noise spectrum measured in this experiment; this is because the experiment in which this phenomenon was observed was performed on a lifting airfoil with a two-sided boundary layer, creating a large pressure difference between the two sides of the airfoil and allowing these jets to form. However, even without the channeling of flow through the serration roots from the pressure side to the suction side of an airfoil, the roots clearly have an effect on the spanwise coherence from serration to serration. The discontinuity in the wall boundary condition, this gap between measurement locations, significantly disturbs the coherence. This effectively suppresses the spanwise coherence at high frequencies for scales smaller than the serration size.

3.7.4 Streamwise Coherence Along Serration

Microphone pair 8-9, with a separation distance of $\Delta x_1 = 7.00$ mm, was used to examine the streamwise coherence along the centerline of the serration. The results for $U_j = 20$, 40, and 60 m/s are shown in Figure 3.31, along with the streamwise coherence data from the flat plate shown in Section 3.1.1.

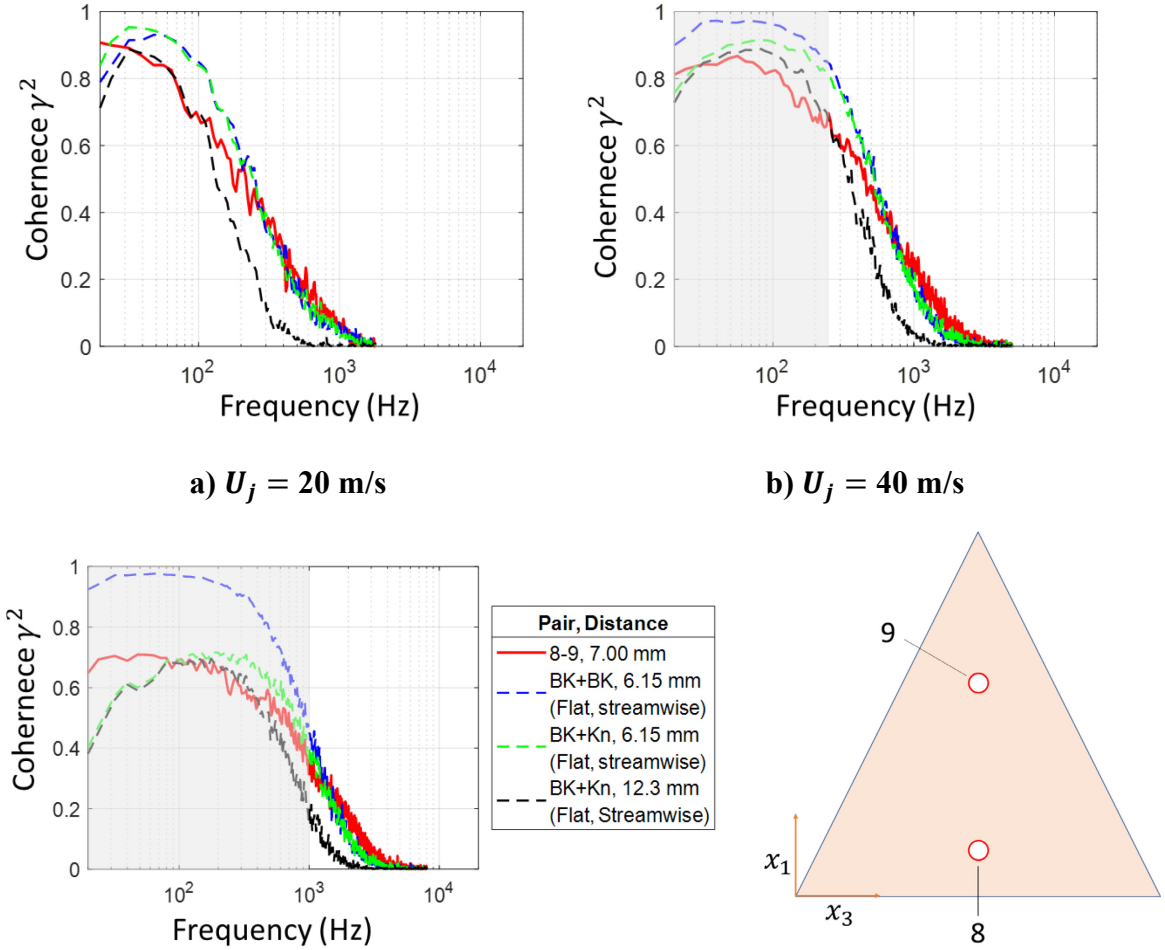

a) $U_j = 20$ m/s **b) $U_j = 40$ m/s**

c) $U_j = 60$ m/s

Figure 3.31, Streamwise coherence along centerline of serration. Blue line represents coherence between two B&K microphones, green line represents coherence between B&K and Knowles microphones.

It can be seen that at low frequencies, the coherence along the serration is reduced compared to the flat plate. This is particularly noticeable at lower speeds where the range of valid data extends to lower frequencies. This range of reduction extends up to 260 Hz at 20 m/s, 700 Hz at 40 m/s, and 1200 Hz at 60 m/s. As the trailing edge is not straight, it is possible that streamwise effects from the serration edges can be observed in measurements along the centerline of the serration, particularly at low frequencies where the associated spanwise

scales are larger. Moreover, this is another indication of an alteration to the flow field induced by the serrations.

3.7.5 Coherence Along the Serration Edge

Of central importance to the theories of Howe [30] and Lyu *et al.* [31] is the surface pressure wavenumber component that couples with the far field observer's location. For a straight trailing edge, this component is $k_3 = 0$; however, for a serrated trailing edge, this coupled wavenumber component is non-zero, and dependent on the angle between the serration edge and the flow. These wavenumbers are given by $k_3 = 2n\pi/\lambda$ [34], and they represent wavevector components normal to the edge. As shown by Equation (1.13), this wavevector component can also be described by the single point frequency spectrum and the coherence decay length l_γ. Reducing either of these components should result in a reduction in scattered sound. These are then used as inputs to a generalized form of Amiet's method; for a conventional boundary layer and assuming frozen turbulence past the serrated edge, a model of the wavenumber-frequency wall pressure spectrum can be evaluated at the wavevectors that correspond to this edge-normal condition. For a wall jet boundary layer, however, this component should be directly measured. A reduction of coherence length corresponds with an overall reduction in coherence, but because it is an integrated value, this does not necessarily mean that the coherence must be decreased over the entire frequency range.

This "spanwise" coherence was measured in this experiment and compared to the coherence along the straight trailing edge, which is simply the spanwise coherence reported earlier. Figure 3.32 shows the coherence along the edge compared to the coherence along the straight trailing edge. Microphone pairs 2-3 and 5-6 are near the root, microphone pairs 3-4 and 4-5 are nearer to the tip, and microphone pair 11-12 is located between the upstream and downstream pairings. Each separation distance listed in Figure 3.32 is the distance along the edge.

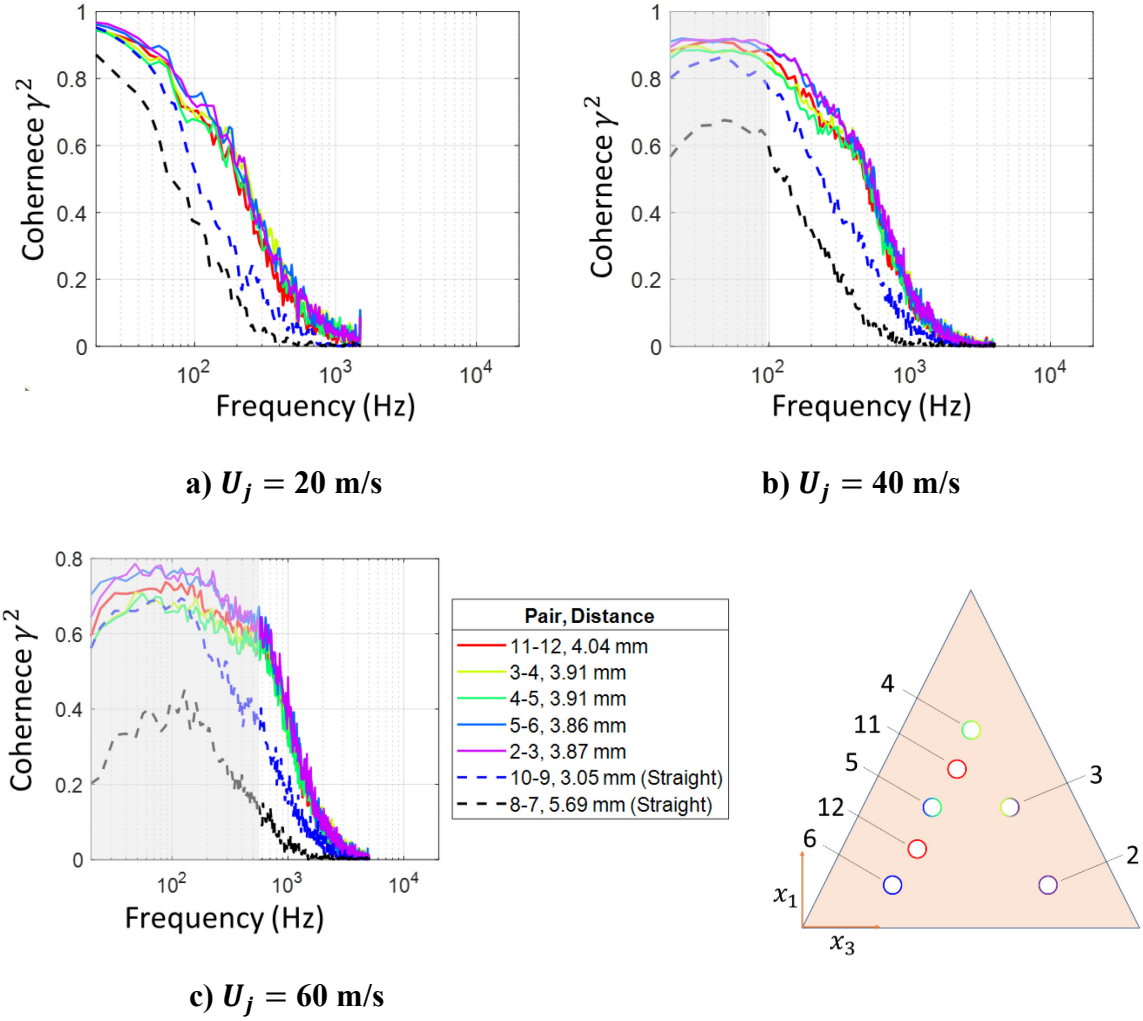

a) $U_j = 20$ m/s **b) $U_j = 40$ m/s**

c) $U_j = 60$ m/s

Figure 3.32, Coherence along the serrated edge compared to coherence along the straight trailing edge.

The coherence along the serrated edge is much greater than that along the straight edge; this is because the serrated edge introduces a streamwise component to the coherence measurement, and streamwise coherence is naturally greater than spanwise coherence given the direction of eddy convection. The downstream microphone pairs also have a higher amount of low-frequency coherence than the upstream pairs; at $U_j = 20$ m/s this effect is hardly discernible, but at $U_j = 40$ and 60 m/s, the coherence curves seem to collapse into a broadband hump. Below this hump, which is located at approximately 400 Hz for $U_j = 40$

m/s and at approximately 650 Hz for $U_j = 60$ m/s, the coherence for the microphone pairs closer to the tip is higher than those closer to the root by about 0.05 at $U_j = 40$ m/s and 0.1 at $U_j = 60$ m/s; however, at least for $U_j = 60$ m/s, this peak also occurs at the edge of the valid frequency range for coherence measurements. Therefore, the peak may not be a real phenomenon of the flow. This peak occurs in the same frequency range as the broadband hump in the surface pressure autospectrum reported in Figure 3.26a.

As there is a streamwise component to the coherence along the edge, this coherence was compared to the flat plate streamwise coherence data. This comparison is shown in Figure 3.33. The edge coherence curves happen to coincide with the flat plate streamwise coherence curves for frequencies above the hump frequencies mentioned above, and above 150 Hz for $U_j = 20$ m/s. The coherence at these shorter edge relative distances indeed seem to have increased coherence due to a streamwise component of separation. This would seem to make the edge potentially a more efficient scatterer of sound, but the relationship between the pressure across the edge and the far field sound is also a function of the trace speed of the disturbance along the edge. This would be akin to rotating the wavevector scattering component away from $k_3 = 0$ as expressed in Equation (1.10), thus reducing the overall efficiency of the scattering edge.

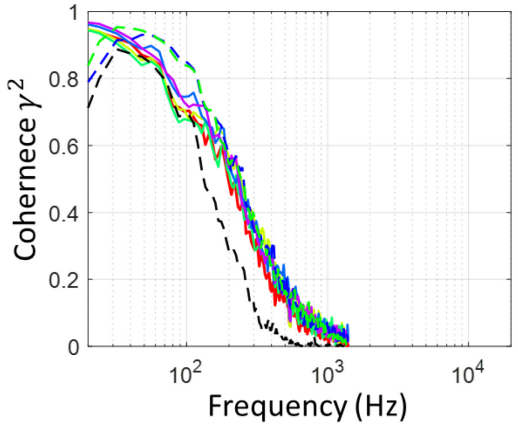

a) $U_j = 20$ m/s

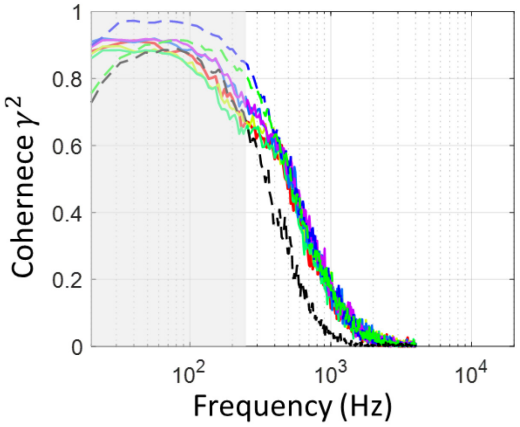

b) $U_j = 40$ m/s

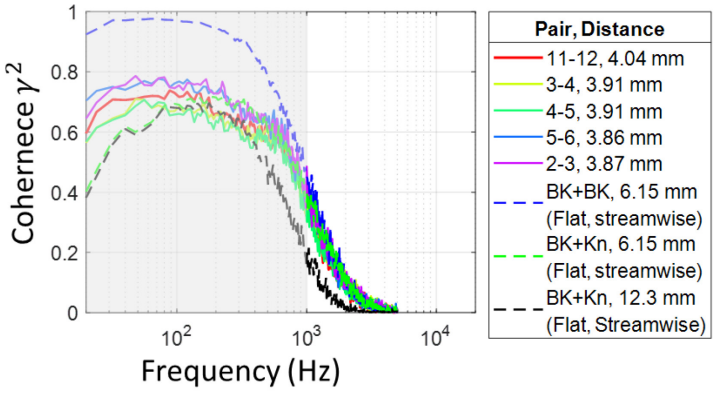

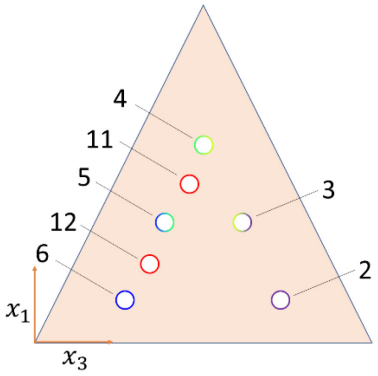

c) $U_j = 60$ m/s

Figure 3.33, Coherence along the serrated edge compared to streamwise coherence on the flat plate.

Chapter 4. Conclusions

In this work, the trailing edge noise radiated by two different trailing edge configurations in a wall jet wind tunnel and the surface pressure upstream of the trailing edge were examined. These configurations consisted of a straight trailing edge 12.7 mm above a solid surface and a serrated trailing edge with amplitude $2h$ = 1.5 cm and wavelength $\lambda = 1.5$ cm at the same streamwise location and distance above the solid surface. The far field noise was measured with an arc array of microphones and a linear beamforming array, which was used to determine the noise source. The surface pressure was measured by embedded microphones which were flush with the surface. In the straight trailing edge configuration, the microphones were distributed along a straight trailing edge to produce a linear array which was designed to extract low spanwise wavenumber components of the wavenumber-frequency wall pressure spectrum. The developed experimental configuration was shown to produce measurable trailing edge noise in the wall jet. Theoretical predictions of the noise were shown to agree with the measured far field noise from the straight trailing edge. The surface pressure results from the straight trailing edge indicate that the Chase wavenumber-frequency wall pressure spectrum's convective ridge may be slightly broader in the spanwise k_3 direction than needed to accurately represent the surface pressure spectrum of a wall jet. Additionally, a disagreement was found with previous experimental results regarding the convection velocity of a wall jet boundary layer, which warrants further examination.

From the far field noise measurements from the serrated trailing edge configuration, it was found that the serrations were effective in providing a baseline reduction of around 3-3.5 dB, and further reduction was observed in regions where the straight trailing edge experienced resonance with the plate below. Thus, the reduction of the far field noise may not be solely due to the serrations themselves, and there is at least a partial component of reduction of the resonance effects due to disruption of the resonant cavity.

Fifteen surface pressure microphones were distributed on and across multiple serrations to reveal the surface pressure evolution on a single serration as well as the coherence of surface pressure fluctuations across serrations. It was found that the surface pressure PSD rises

towards the tip in agreement with the findings of Gruber [34] and Chong and Vathylakis [63], and in contrast to the findings of Avallone *et al.* [64] and Ragni *et al.* [62]. This discrepancy is thought to be due to the difference in configuration between the experimental setups, with the work of Gruber, Chong and Vathylakis, and this work examining a single-sided flat plate boundary layer and the work of Avallone *et al.* and Ragni *et al.* examining a two-sided airfoil boundary layer. This suggests that there may be some fundamental differences between a single sided flat plate boundary layer and the flow over a real airfoil that need to be addressed for the purpose of examining the flow around trailing edge serrations. The spanwise coherence between two locations on the same serration was found to increase, while the spanwise coherence between two locations on different serrations was found to decrease. It was concluded that larger scales are incoherent when spanning two serrations because the coherence length decreases due to the disruptive presence of the root. The increase in coherence along the serration edge is due to the introduction of a streamwise component to the coherent measurement, and it is concluded that the relationship between the surface pressure and far field sound is also dependent on the trace speed of the disturbance along the edge, which counters the theoretical increase in far field noise from the increased coherence along the edge.

Future work should include a more comprehensive study of the evolution of surface pressure field on a single serration. While it may not be possible to comprehensively model the surface pressure field on a serration and therefore analytically predict the trailing edge noise, further exploration of the coupling between the coherence length change and the far field noise change should be done, in accordance with the conclusions of Lyu *et al.* [31]. This "model" should be expanded to include the effects of the serrations on the overall flow as seen in previous experiments and in these experiments. Our understanding of the mechanism of trailing edge noise reduction due to serrations remains incomplete, but it is becoming an ever more realizable goal.

References

[1] Glegg, S., and Devenport, W. J. *Aeroacoustics of Low Mach Number Flows: Fundamentals, Analysis, and Measurement*. Academic Press, 2017.

[2] Lighthill, M. J. "On Sound Generated Aerodynamically I. General Theory." *Proceedings of the Royal Society of London. Series A. Mathematical and Physical Sciences*, Vol. 211, No. 1107, 1952, pp. 564–587. doi:10.1098/rspa.1952.0060.

[3] Curle, N. "The Influence of Solid Boundaries upon Aerodynamic Sound." *Proceedings of the Royal Society of London. Series A. Mathematical and Physical Sciences*, Vol. 231, No. 1187, 1955, pp. 505–514. doi:10.1098/rspa.1955.0191.

[4] Brooks, T. F., Pope, D. S., and Marcolini, M. A. *Airfoil Self-Noise and Prediction*. 1989.

[5] Oerlemans, S., Fisher, M., Maeder, T., and Kögler, K. "Reduction of Wind Turbine Noise Using Optimized Airfoils and Trailing-Edge Serrations." *AIAA Journal*, Vol. 47, No. 6, 2009, pp. 1470–1481. doi:10.2514/1.38888.

[6] Roger, M., and Moreau, S. "Broadband Self-Noise from Loaded Fan Blades." *AIAA Journal*, Vol. 42, No. 3, 2004, pp. 536–544. doi:10.2514/1.9108.

[7] Sinayoko, S., Kingan, M., and Agarwal, A. "Trailing Edge Noise Theory for Rotating Blades in Uniform Flow." *Proceedings of the Royal Society A: Mathematical, Physical and Engineering Sciences*, Vol. 469, No. 2157, 2013. doi:10.1098/rspa.2013.0065.

[8] Amiet, R. K. "Noise Due to Turbulent Flow Past a Trailing Edge." *Journal of Sound and Vibration*, Vol. 47, No. 3, 1976, pp. 387–393. doi:10.1016/0022-460X(76)90948-2.

[9] Ffowcs Williams, J. E., and Hall, L. H. "Aerodynamic Sound Generation by Turbulent Flow in the Vicinity of a Scattering Half Plane." *Journal of Fluid Mechanics*, Vol. 40, No. 4, 1970, pp. 657–670. doi:10.1017/S0022112070000368.

[10] Chase, D. M. "Modeling the Wavevector-Frequency Spectrum of Turbulent Boundary Layer Wall Pressure." *Journal of Sound and Vibration*, Vol. 70, No. 1, 1980, pp. 29–67. doi:10.1016/0022-460X(80)90553-2.

[11] Schwarzschild, K. "Die Beugung Und Polarisation Des Lichts Durch Einen Spalt. I." *Mathematische Annalen*, Vol. 55, No. 2, 1901, pp. 177–247. doi:10.1007/BF01444971.

[12] Amiet, R. K. Effect of the Incident Surface Pressure Field on Noise Due to Turbulent

Flow Past a Trailing Edge. *Journal of Sound and Vibration*. 2. Volume 57, 305–306.

[13] Howe, M. S. "A Review of the Theory of Trailing Edge Noise." *Journal of Sound and Vibration*, Vol. 61, No. 3, 1978, pp. 437–465. doi:10.1016/0022-460X(78)90391-7.

[14] Brooks, T. F., and Hodgson, T. H. "Trailing Edge Noise Prediction from Measured Surface Pressures." *J. Sound & Vib.*, Vol. 78, No. 1, Sep.8, 1981, pp.69-117., 1981, pp. 69–117.

[15] Roger, M., and Moreau, S. "Trailing Edge Noise Measurements and Prediction for Subsonic Loaded Fan Blades." *8th AIAA/CEAS Aeroacoustics Conference and Exhibit*, 2002. doi:10.2514/6.2002-2460.

[16] Herrig, A., Kamruzzaman, M., Würz, W., and Wagner, S. "Broadband Airfoil Trailing-Edge Noise Prediction from Measured Surface Pressures and Spanwise Length Scales." *International Journal of Aeroacoustics*, Vol. 12, No. 1–2, 2013, pp. 53–82. doi:10.1260/1475-472X.12.1-2.53.

[17] Corcos, G. M. "The Structure of the Turbulent Pressure Field in Boundary-Layer Flows." *Journal of Fluid Mechanics*, Vol. 18, No. 3, 1964, pp. 353–378. doi:10.1017/S002211206400026X.

[18] Howe, M. S. *Acoustics of Fluid-Structure Interactions*. 1998.

[19] Chase, D. M. "The Character of the Turbulent Wall Pressure Spectrum at Subconvective Wavenumbers and a Suggested Comprehensive Model." *Journal of Sound and Vibration*, Vol. 112, No. 1, 1987, pp. 125–147. doi:10.1016/S0022-460X(87)80098-6.

[20] Goody, M. "Empirical Spectral Model of Surface Pressure Fluctuations." *AIAA Journal*, Vol. 42, No. 9, 2004, pp. 1788–1794. doi:10.2514/1.9433.

[21] Graham, W. R. "A Comparison of Models for the Wavenumber-Frequency Spectrum of Turbulent Boundary Layer Pressures." *Journal of Sound and Vibration*, Vol. 206, No. 4, 1997, pp. 541–565. doi:10.1006/jsvi.1997.1114.

[22] Graham, R. R. "The Silent Flight of Owls." *The Journal of the Royal Aeronautical Society*, Vol. 38, No. 286, 1934, pp. 837–843. doi:10.1017/s0368393100109915.

[23] Geyer, T., Sarradj, E., and Fritzsche, C. "Measurement of the Noise Generation at the Trailing Edge of Porous Airfoils." *Experiments in Fluids*, Vol. 48, No. 2, 2010, pp. 291–308. doi:10.1007/s00348-009-0739-x.

[24] Rubio Carpio, A., Merino Martínez, R., Avallone, F., Ragni, D., Snellen, M., and van der Zwaag, S. "Broadband Trailing Edge Noise Reduction Using Permeable Metal

Foams." *Inter-Noise 2017*, Vol. 2017, No. August, 2017.

[25] Rubio Carpio, A., Merino Martínez, R., Avallone, F., Ragni, D., Snellen, M., and van der Zwaag, S. "Experimental Characterization of the Turbulent Boundary Layer over a Porous Trailing Edge for Noise Abatement." *Journal of Sound and Vibration*, Vol. 443, 2019, pp. 537–558. doi:10.1016/j.jsv.2018.12.010.

[26] Clark, I. A., Devenport, W., Jaworski, J. W., Daly, C., Peake, N., and Glegg, S. "The Noise Generating and Suppressing Characteristics of Bio-Inspired Rough Surfaces." *20th AIAA/CEAS Aeroacoustics Conference*, 2014. doi:10.2514/6.2014-2911.

[27] Clark, I. A., Alexander, W. N., Devenport, W., Glegg, S., Jaworski, J. W., Daly, C., and Peake, N. "Bioinspired Trailing-Edge Noise Control." *AIAA Journal*, Vol. 55, No. 3, 2017, pp. 740–754. doi:10.2514/1.J055243.

[28] Bodling, A., and Sharma, A. "Numerical Investigation of Low-Noise Airfoils Inspired by the down Coat of Owls." *Bioinspiration and Biomimetics*, Vol. 14, No. 1, 2019. doi:10.1088/1748-3190/aaf19c.

[29] Afshari, A., Azarpeyvand, M., Dehghan, A. A., Szöke, M., and Maryami, R. "Trailing-Edge Flow Manipulation Using Streamwise Finlets." *Journal of Fluid Mechanics*, Vol. 870, No. June 2016, 2019, pp. 617–650. doi:10.1017/jfm.2019.249.

[30] Howe, M. S. "Aerodynamic Noise of a Serrated Trailing Edge." *Journal of Fluids and Structures*, Vol. 5, No. 1, 1991, pp. 33–45. doi:10.1016/0889-9746(91)80010-B.

[31] Lyu, B., Azarpeyvand, M., and Sinayoko, S. "Prediction of Noise from Serrated Trailing Edges." *Journal of Fluid Mechanics*, Vol. 793, 2016, pp. 556–588. doi:10.1017/jfm.2016.132.

[32] Howe, M. S. "Noise Produced by a Sawtooth Trailing Edge." *Journal of the Acoustical Society of America*, Vol. 90, No. 1, 1991, pp. 482–487. doi:10.1121/1.401273.

[33] Gruber, M., Joseph, P. F., and Chong, T. P. "On the Mechanisms of Serrated Airfoil Trailing Edge Noise Reduction." *17th AIAA/CEAS Aeroacoustics Conference 2011 (32nd AIAA Aeroacoustics Conference)*, No. June, 2011, pp. 5–8. doi:10.2514/6.2011-2781.

[34] Gruber, M. *Airfoil Noise Reduction by Edge Treatments*. University of Southampton, 2012.

[35] Moreau, D. J., and Doolan, C. J. "Noise-Reduction Mechanism of a Flat-Plate Serrated Trailing Edge." *AIAA Journal*, Vol. 51, No. 10, 2013, pp. 2513–2522. doi:10.2514/1.J052436.

[36] Chong, T. P., Joseph, P., and Gruber, M. “An Experimental Study of Airfoil Instability Noise with Trailing Edge Serrations.” *16th AIAA/CEAS Aeroacoustics Conference (31st AIAA Aeroacoustics Conference)*, 2010. doi:10.2514/6.2010-3723.

[37] Kleinfelter, A., Repasky, R., Hari, N., Letica, S., Vishwanathan, V., Organski, L., Schwaner, J., Alexander, W. N., and Devenport, W. “Development and Calibration of a New Anechoic Wall Jet Wind Tunnel.” *AIAA Scitech 2019 Forum*, 2019. doi:10.2514/6.2019-1936.

[38] Alexander, W. N. *Sound from Rough Wall Boundary Layers*. Virginia Polytechnic Institute and State University, 2011.

[39] Morel, T. “Design of Two-Dimensional Wind Tunnel Contractions.” *Journal of Fluids Engineering, Transactions of the ASME*, Vol. 99, No. 2, 1977, pp. 371–377. doi:10.1115/1.3448764.

[40] Fang, F. M., Chen, J. C., and Hong, Y. T. “Experimental and Analytical Evaluation of Flow in a Square-to-Square Wind Tunnel Contraction.” *Journal of Wind Engineering and Industrial Aerodynamics*, Vol. 89, No. 3–4, 2001, pp. 247–262. doi:10.1016/S0167-6105(00)00080-5.

[41] Grissom, D. L. *A Study of Sound Generated by a Turbulent Wall Jet Flow Over Rough Surfaces*. Virginia Tech, 2007.

[42] Yegna Narayan, K., and Narasimha, R. “Parametric Analysis of Turbulent Wall Jets.” *Aeronautical Quarterly*, Vol. 24, No. 3 (August, 1973), 1973, pp. 207–218. doi:10.1017/s0001925900006600.

[43] Wygnanski, I., Katz, Y., and Horev, E. “On the Applicability of Various Scaling Laws to the Turbulent Wall Jet.” *Journal of Fluid Mechanics*, Vol. 234, 1992, pp. 669–690. doi:10.1017/S002211209200096X.

[44] Knowles Electronics. FG-23329-P07 Datasheet.

[45] Bendat, J. S., and Piersol, A. G. *Random Data: Analysis and Measurement Procedures*. Wiley, Hoboken, NJ, 2010.

[46] Blake, W. K., and Chase, D. M. “Wavenumber-Frequency Spectra of Turbulent-Boundary-Layer Pressure Measured by Microphone Arrays.” *The Journal of the Acoustical Society of America*, Vol. 49, No. 3B, 1971, pp. 862–877. doi:10.1121/1.1912427.

[47] Farabee, T. M., and Geib, F. E. Measurements of Boundary Layer Pressure Fluctuations at Low Wavenumbers on Smooth and Rough Walls. No. 11, 1991, pp. 55–68.

[48] Devenport, W., Wahl, E. A., Glegg, S. A. L., Alexander, W. N., and Grissom, D. L. "Measuring Surface Pressure with Far Field Acoustics." *Journal of Sound and Vibration*, Vol. 329, No. 19, 2010, pp. 3958–3971. doi:10.1016/j.jsv.2010.03.012.

[49] Joseph, L. A. *Pressure Fluctuations in a High-Reynolds-Number Turbulent Boundary Layer over Rough Surfaces of Different Element Spacing*. Virginia Polytechnic Institute and State University, 2017.

[50] Millican, A. J. *Bio-Inspired Trailing Edge Noise Control: Acoustic and Flow Measurements*. Virginia Polytechnic Institute and State University, 2017.

[51] Millican, A. J., Clark, I., Devenport, W., and Alexander, W. N. "Owl-Inspired Trailing Edge Noise Treatments: Acoustic and Flow Measurements." *AIAA SciTech Forum - 55th AIAA Aerospace Sciences Meeting*, No. January, 2017, pp. 1–29. doi:10.2514/6.2017-1177.

[52] Schetz, J. A., and Bowersox, R. D. W. *Boundary Layer Analysis*. AIAA, 2011.

[53] Billingsley, J., and Kinns, R. "The Acoustic Telescope." *Journal of Sound and Vibration*, Vol. 48, No. 4, 1976, pp. 485–510. doi:10.1016/0022-460X(76)90552-6.

[54] Tester, B. J., and Glegg, S. A. L. "A Review of Engine Noise Source Diagnostic Methods for Static Engine Tests, with Phased Array and Polar Correlation Techniques." *14th AIAA/CEAS Aeroacoustics Conference (29th AIAA Aeroacoustics Conference)*, No. May, 2008, pp. 5–7. doi:10.2514/6.2008-2854.

[55] Corcos, G. M. "Resolution of Pressure in Turbulence." *The Journal of the Acoustical Society of America*, Vol. 35, No. 2, 1963, pp. 192–199. doi:10.1121/1.1918431.

[56] Maidanik, G., and Jorgensen, D. W. "Boundary Wave-Vector Filters for the Study of the Pressure Field in a Turbulent Boundary Layer." *The Journal of the Acoustical Society of America*, Vol. 42, No. 2, 1967, pp. 494–501. doi:10.1121/1.1910606.

[57] Arguillat, B., Ricot, D., Bailly, C., and Robert, G. "Measured Wavenumber: Frequency Spectrum Associated with Acoustic and Aerodynamic Wall Pressure Fluctuations." *The Journal of the Acoustical Society of America*, Vol. 128, No. 4, 2010, pp. 1647–1655. doi:10.1121/1.3478780.

[58] Ehrenfried, K., and Koop, L. "Experimental Study of Pressure Fluctuations beneath a Compressible Turbulent Boundary Layer." *14th AIAA/CEAS Aeroacoustics Conference*, 2008. doi:10.2514/6.2008-2800.

[59] Leclercq, D. J. J., and Bohineust, X. "Investigation and Modelling of the Wall Pressure Field Beneath a Turbulent Boundary Layer at Low and Medium Frequencies." *Journal of Sound and Vibration*, Vol. 257, No. 3, 2002, pp. 477–501.

[60] Palumbo, D. “Determining Correlation and Coherence Lengths in Turbulent Boundary Layer Flight Data.” *Journal of Sound and Vibration*, Vol. 331, No. 16, 2012, pp. 3721–3737. doi:10.1016/j.jsv.2012.03.015.

[61] Raichel, D. R., and Hansen, U. J. *The Science and Applications of Acoustics*. Springer, 2006.

[62] Ragni, D., Avallone, F., van der Velden, W. C. P., and Casalino, D. “Measurements of Near-Wall Pressure Fluctuations for Trailing-Edge Serrations and Slits.” *Experiments in Fluids*, Vol. 60, No. 1, 2019, pp. 1–22. doi:10.1007/s00348-018-2654-5.

[63] Chong, T. P., and Vathylakis, A. “On the Aeroacoustic and Flow Structures Developed on a Flat Plate with a Serrated Sawtooth Trailing Edge.” *Journal of Sound and Vibration*, Vol. 354, 2015, pp. 65–90. doi:10.1016/j.jsv.2015.05.019.

[64] Avallone, F., Van Der Velden, W. C. P., Ragni, D., and Casalino, D. “Noise Reduction Mechanisms of Sawtooth and Combed-Sawtooth Trailing-Edge Serrations.” *Journal of Fluid Mechanics*, Vol. 848, 2018, pp. 560–591. doi:10.1017/jfm.2018.377.